Antti Näsilä

Validation of Aalto-1 Spectral Imager Technology to Space Environment

School of Electrical Engineering

Thesis submitted for examination for the degree of Master of Science in Technology.

Espoo 1.5.2013

Thesis supervisor:

Prof. Martti Hallikainen

Thesis advisor:

M.Sc. (Tech.) Kai Viherkanto

Aalto University
School of Electrical
Engineering

AALTO-YLIOPISTO
SÄHKOTEKNIIKAN KORKEAKOULU

DIPLOMITYÖN
TIIVISTELMÄ

Tekijä: Antti Näsilä

Työn nimi: Aalto-1 -satelliitin spektrikamerateknologian validointi avaruusympäristöön

Päivämäärä: 1.5.2013 Kieli: Englanti Sivumäärä:10+79

Radiotieteen ja -tekniikan laitos

Professuuri: Avaruustekniikka Koodi: S-92

Valvoja: Prof. Martti Hallikainen

Ohjaaja: DI Kai Viherkanto

Tässä työssä suoritettiin Aalto-1 -nanosatelliitin spektrikameran pietso-aktuoidun Fabry–Perot Interferometrin avaruuskvalifiointi. Spektrikamera tulee olemaan Aalto-1 -satelliitin päähyötykuorma. Avaruuskvalifiointia varten suunniteltiin ja toteutettiin avaruustestikampanja, joka sisälsi lämpösyklauksen lämpökaapissa, tärinä- ja shokkitestit, taajuus- ja askelvasteiden mittaukset tyhjiössä. Lopuksi suoritettiin myös sarja testejä termovakuumikammiossa. Fabry–Perot Interferometrin suorituskyvylle asetettiin seuraavat spesifikaatiot: läpäisy 0.1–0.3, spektraalinen resoluutio 10–30 nm, spektrinen vakaus 0.2 nm/°C sekä säätönopeus $<$ 30 ms. Tämän lisäksi vaaditiin myös selviytymistä lämpötila- (-45–65°C) ja laukaisuympäristöistä. Muutamien korjausten jälkeen Fabry–Perot -moduuli läpäisi kaikki kvalifikaatiotestit ja spesifikaatiot täytettiin, joten moduuli on kvalifioitu avaruusolosuhteisiin onnistuneesti.

Avainsanat: Fabry–Perot Interferometri, Aalto-1, Avaruus, Testaus

AALTO UNIVERSITY
SCHOOL OF ELECTRICAL ENGINEERING

ABSTRACT OF THE
MASTER'S THESIS

Author: Antti Näsilä

Title: Validation of Aalto-1 Spectral Imager Technology to Space Environment

Date: 1.5.2013 Language: English Number of pages:10+79

Department of Radio Science and Technology

Professorship: Space Technology Code: S-92

Supervisor: Prof. Martti Hallikainen

Advisor: M.Sc. (Tech.) Kai Viherkanto

The goal of this work was the successful space qualification of the piezo-actuated Fabry–Perot Interferometer module for the Aalto-1 Spectral Imager, which is designed to be the main payload of the Aalto-1 nanosatellite. To accomplish this goal, series of tests were designed and implemented. The tests included thermal cycling in temperature chamber, vibration and shock tests, frequency and step response tests in low vacuum and finally a series of hard vacuum tests in thermal vacuum chamber. The design specifications related to performance of the Fabry–Perot module were set for transmission (0.1–0.3), spectral resolution (10–30 nm), spectral stability (0.2 nm/°C) and tuning speed (<30 ms). In addition to this, there were also specifications for the temperature (-45–65°C) and launch vehicle environment. After some re-designs, The Fabry–Perot module passed all the qualification tests, and the design specifications were met, thus the module can be qualified for space environment.

Keywords: Fabry-Perot Interferometer, Aalto-1, Space, Qualification

Preface

The work done in this thesis was conducted in the Photonic Sensors team of VTT Technical Research Centre of Finland during 2012 and 2013 as a part of the ESA activity "MEMS Fabry–Perot Interferometer Technology for Miniaturized Hyperspectral Imagers and Microspectrometers".

I would like to thank the project manager Kai Viherkanto for the opportunity to do my thesis as a part of such an interesting activity and for acting as the instructor for my thesis. I am also grateful to my supervisor Prof. Martti Hallikainen for accepting to supervise this thesis.

I would also like to thank my co-workers Christer Holmlund, Heikki Saari, Jarkko Antila, Jussi Mäkynen, Rami Mannila, Tapani Antila and Uula Kantojärvi and the rest of the team for their advice and guidance. I'd still be in the lab without your help.

Special thanks also go to my family and friends and, most of all, to my girlfriend Varpu, who was kind enough to correct most of my spelling mistakes.

Otaniemi, 1.5.2013

Antti Näsilä

Table of contents

Symbols and Abbreviations

Symbols

α	Absorptivity
α_λ	Absorption
γ	Heat capacity ratio
ϵ	Emissivity
ϵ_λ	Phase change per reflection
ϵ_0	Vacuum permittivity, 8.854×10^{-12} F m^{-1}
θ	Angle of incidence
λ	Wavelength
σ	Stefan–Boltzmann constant, 5.670×10^{-8} W m^{-2} K^4
τ_λ	Relative intensity transmission
Φ_n	Spectral photon flux
φ	Net phase difference
φ_0	Phase shift of the wave
Ω	Solid angle
ω	Angular frequency

$A(\varphi, R)$	Airy function
A	Surface area
A_α	Absorbing surface area
A_ϵ	Emitting surface area
$A_{electrode}$	Electrode surface area
A_0	Amplitude of an electromagnetic plane wave
ΔC	Capacitance change
C_{fb}	Feedback capacitance
C_{gap}	Capacitance of the FPI electrodes
C_m	FPI electrode capacitance
C_ref	Reference capacitance
Δd	Electrode displacement
d	Air gap length
d_{sp}	Air gap at given set point
d_0	Initial air gap length
$\vec{E}$ / E / E_0	Electromagnetic plane wave
E_T	Total transmitted amplitude
F'	Coefficient of Finesse
f	Frequency
g	Standard gravity, 9.81 m s^{-2}
i	Imaginary unit
I	Intensity

J	Energy radiated by a black body
$J_{incident}$	Incident heat flux
$\vec{k}$	Wave vector
k	Wave number
m	Order of interference
m_{eff}	Effective order of interference
m_s	Mirror mass
n	Index of refraction
$N_{D,i}$	Defective Finesse caused by surface irregularities of the mirror
$N_{D,s}$	Defective Finesse caused by mirror deformation
$N_{D,w}$	Defective Finesse caused by mirror wedging
N_A	Aperture Finesse
N_D	Defective Finesse
N_{eff}	Effective Finesse
N_r	Reflective Finesse
P	Ambient pressure
$\vec{r}$	Position vector
r	Amplitude reflection coefficient
R_λ	Intensity reflection coefficient
R_{fb}	Feedback resistance
$S_{B1,2,3}$	Spectral response of a blue pixel
S_{Bm}	Signal measured by blue pixels
$S_{G1,2,3}$	Spectral response of a green pixel
S_{Gm}	Signal measured by green pixels
$S_{R1,2,3}$	Spectral response of a red pixel
S_{Rm}	Signal measured by red pixels
T	Temperature
t	Amplitude transmission coefficient
T_λ	Intensity transmission coefficient
t_0	Moment in time
U_{out}	Output voltage
V_{bias}	Bias voltage
V_e	Error signal voltage
V_{ref}	Reference voltage
V_{sp}	Set point voltage

Terms and Abbreviations

Aalto-1	The first Finnish nanosatellite mission
AaSI	Aalto-1 Spectral Imager
Air gap	The distance between the FPI mirrors
ASD	Acceleration Spectral Density
CMOS	Complementary Metal Oxide Semiconductor
CMOSIS	Image sensor manufacturer called CMOSIS
COMSOL™	A commercial finite element analysis and simulation software
COTS	Commercial-Off-The-Shelf
CubeSat	A popular nanosatellite standard
CVCM	Collected Volatile Condensable Material
CWL	Center Wavelength
DAQ	Data Acquisition
DN	Digital Number
ECSS	European Cooperation for Space Standardization
EPS	Electrical Power System
FEM	Finite Element Method
FPGA	Field-Programmable Gate Array
FPI	Fabry–Perot Interferometer
FSR	Free Spectral Range
FWHM	Full-Width at Half-Maximum
HeNe	Helium-Neon
HR4000	Spectrometer by Ocean Optics Inc.
I/F	Interface
INTA	Instituto Nacional De Tecnica Aeroespacial
JWST	James Webb Space Telescope
LASCO	Large Angle and Spectrometric Coronagraph Experiment
LED	Light Emitting Diode
LEO	Low Earth Orbit
LVDS	Low-Voltage Differential Signaling
MEMS	Micro-Electro-Mechanical System
MFPI	MEMS Fabry–Perot Interferometer
MOSFET	Metal Oxide Semiconductor Field Effect Transistor
MPM2000	Fiber-optic multiplexer by Ocean Optics Inc.
OBC	On-Board Computer
OPD	Optical Path Difference
P-V	Peak-to-Valley
PCB	Printed Circuit Board
PFPI	Piezo-actuated Fabry–Perot Interferometer
PPM	Parts-Per-Million
RGB	Red-Green-Blue
RML	Recovered Mass Loss

RMS	Root-Mean-Square
SD	Standard Deviation
SDRAM	Synchronous Dynamic Random Access Memory
SEL	Single Event Latch-up
Set point	Piezo-actuator control voltage, determines the air gap at each actuator
SEU	Single Event Upset
SiO_2	Silicon dioxide
SP1	Set point of actuator 1
SP2	Set point of actuator 2
SP3	Set point of actuator 3
SPI	Serial Peripheral Interface
SRS	Shock Response Spectrum
TBC	To Be Confirmed
TML	Total Mass Loss
UV	Ultraviolet
VIS	Visible light camera of AaSI
VTT	VTT Technical Research Centre of Finland

1 Introduction

Spectroscopy is a field which studies the interaction of electromagnetic radiation with matter. Spectrometers are used to detect, measure and analyze the spectral content of electromagnetic radiation. The spectral information can be used, for example, for identifying chemical composition of a given target, like atmosphere or forest. More accurate instruments allow us to detect smaller and smaller differences in spectral signatures.

Earth observation satellites have been in the sky since the 1960's, and the first satellite capable of spectral imaging, LandSat-1, was launched in 1972 [1]. Traditional satellites have been very bulky and robust, but the miniaturization of electronics has enabled the emergence of micro, nano and picosatellites [2, 3, 4]. The most common type of nanosatellite is the CubeSat, a concept developed by CalPoly in 1999 [5]. The CubeSat Standard [6] defines the dimensions of the satellite very clearly, thus all satellites following the specification are automatically compatible with the launch vehicle interface developed for CubeSats. This enables easier and cheaper launch opportunities for nanosatellite missions. The popularity of the cubesat concept has led to good availability of many commercial-off-the-shelf (COTS) subsystems designed for nanosatellites.

Aalto University has initiated the first Finnish nanosatellite mission, Aalto-1, in early 2010 [7]. Aalto-1 will be a three-unit cubesat, which means that the size of the satellite will be 34 x 10 x 10 mm^3, as specified by the CubeSat Design Specification. The main payload of Aalto-1 will be a miniaturized imaging spectrometer, called Aalto-1 Spectral Imager (AaSI). AaSI is also made compatible with the CubeSat Standard, in order to reduce development cost and to make the instrument compatible with other CubeSats as well.

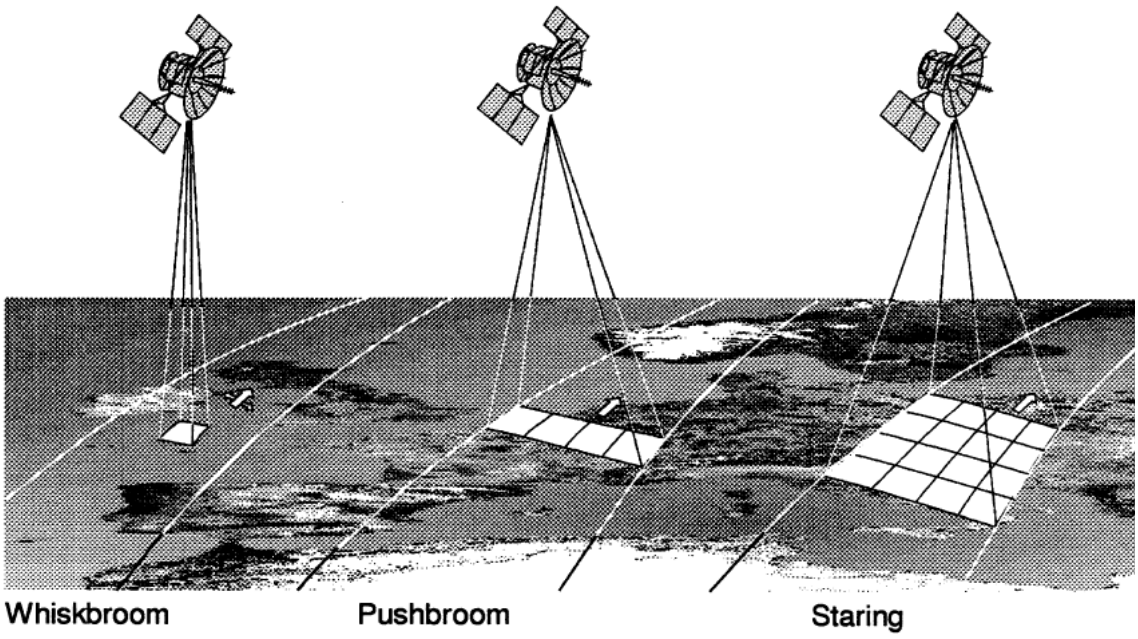

Figure 1: Different imaging concepts [1]. AaSI will be a staring imager.

Most spaceborne spectrometers work in either whiskbroom or pushbroom configurations (Figure 1). In whiskbroom imagers the image is formed by sweeping the telescope from one edge of the swath to the other. In pushbroom imagers the whole swath is imaged at once. For both of these types the image formed is one dimensional (a point or a line), as the other dimension of the sensor is reserved for the spectral information. In these imagers movement of the satellite will provide the other spatial dimension. Third option is to use a staring imager, which produces a two dimensional image with a single exposure. In this case the spectral sorting has to be performed differently, as the image sensor uses both dimensions for spatial information. In staring imagers the target is imaged several times at different wavelengths and the spectral sorting is usually done with tunable or changeable filters.

The Aalto-1 Spectral Imager (AaSI) will be a staring instrument, and the spectral selection is done with a tunable Fabry–Perot Interferometer (FPI). The Fabry–Perot Interferometer is introduced in more detail in Chapter 2 and the design and the operational principle of AaSI will be explained in Chapter 4. Tunable Fabry–Perot Interferometers have been used in space applications before [8, 9], and VTT has developed a novel miniaturized FPI [10], which enables imaging devices for nanosatellites or unmanned aerial platforms. This method is also suitable for missions with limited downlink capacity, as the amount of data can be controlled by selecting only relevant spectral channels and discarding the rest.

However, due to the novelty of the technology used in AaSI, a complete characterization of the FPI is required before it can be used in spaceborne instruments. This thesis mainly focuses on the characterization and space qualification of the FPI module that will be used in AaSI. The module will have to survive the launch environment and the space environment, which will be explained in more detail in Chapter 3. The FPI module will be put through tests which simulate this environment, and these tests are described in Chapters 5, 6, 7 and 8. The tests include detailed temperature characterization, vibration and shock tests, vacuum characterization and finally thermal vacuum cycling.

2 The Fabry–Perot Interferometer

The idea behind the Fabry–Perot Interferometer (FPI) was introduced in the end of the 19th century by Charles Fabry and Albert Perot [11]. The Fabry–Perot Interferometer is a critical part of AaSI, as it is used for spectral selection, so the basic principles of the interferometer are introduced in this chapter. VTT has developed two different kinds of tunable FPI's: Micro-electro-mechanical (MEMS) and Piezo-actuated Fabry–Perot Interferometers [12]. The Piezo-actuated FPI's (PFPI) are larger (aperture sizes up to 20 mm), so they are more suitable for low lighting conditions and imaging applications. The MEMS FPI's (MFPI) are much smaller, but their light gathering apertures are rather limited (ca. 2 mm) at the current time. This work mainly focuses on the piezo-actuated version, as a 15.5 mm aperture PFPI will be used in AaSI.

2.1 Theoretical background

A Fabry–Perot Interferometer consists of two parallel reflective surfaces, which causes the beams of light to reflect back and forth between the mirrors (Figure 2). A constructive interference within the interferometer allows certain wavelengths to be transmitted while others are reflected.

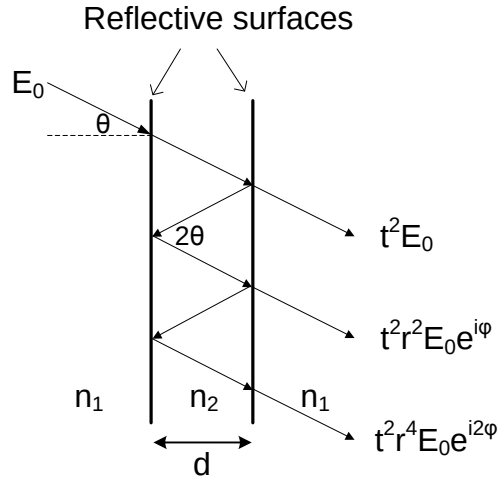

Figure 2: Light reflecting within the FPI. E_0 is the beam of light entering the FPI and the beams on the right are beams exiting the FPI after 0, 2 and 4 reflections. n_1 and n_2 are the indices of refraction and d is the separation distance of the mirrors (usually referred as the air gap or FPI cavity).

As light is electromagnetic radiation, a beam of light can be considered as an electromagnetic plane wave, described by [13]

$$\vec{E}(\vec{r},t) = A_0 e^{i(\vec{k}\cdot\vec{r}-\omega t+\varphi)} = A_0 e^{i(\vec{k}\cdot\vec{r}-\omega t_0)} e^{i\varphi_0} \tag{1}$$

where A_0 is the amplitude, $\vec{k}$ is the wavevector, $\vec{r}$ is the position vector, ω is the angular frequency, φ is the phase shift of the wave and t_0 is a given moment in time. This equation can be still simplified to

$$E = E_0 e^{i\varphi}, \tag{2}$$

where $E_0 = A_0 e^{i(kr-\omega t_0)}$, so $E = E_0$ when phase shift is zero.

For simplicity, it can be assumed that both mirrors are identical, so the reflection and transmission coefficient are also identical, thus $r = r_1 = r_2$ and $t = t_1 = t_2$. It is also assumed that the reflectivity is independent of wavelength. In this case the refractive index n can be assumed to be the same inside and outside the FPI cavity ($n_2 = n_1 = 1$ when the medfium is air). The optical path difference (OPD) between adjacent rays is given by [14]

$$OPD = 2nd\cos\theta, \tag{3}$$

which can also be seen from Figure 2. By using this path difference it is possible to find the phase difference between any pair of rays. The net phase difference (φ) is the combination of the OPD and the wavelength-dependent phase change per reflection (ϵ_λ) [13]:

$$\varphi = \left(\frac{2\pi}{\lambda}\right) 2nd\cos\theta - 2\epsilon_\lambda \tag{4}$$

Constructive interference occurs when the net phase difference equals $2\pi m$, where m (order of interference) is an integer number. Thus the center wavelength (CWL) of the constructive interferences (Figure 3) can be expressed by

$$\left(m + \frac{\epsilon_\lambda}{\pi}\right)\lambda = m_{\text{eff}}\lambda = 2nd\cos\theta. \tag{5}$$

Now, when a beam of light with an amplitude E_0 arrives to the first mirror of the FPI, only a part of it, tE_0, enters the optical cavity. When the same beam of light arrives to the second mirror, only a part of it, t^2E_0, exits the FPI while a part, trE_0, is reflected back. When the reflected beam arrives to the second mirror again, a part of it exits ($t^2r^2E_0$)the FPI while a part is reflected (tr^2E_0) again, so at each passage the amplitude of the transmitted light reduces by a factor of r^2. In addition to this, at each passage through the cavity a phase shift occurs (given by Equation 4). The total amplitude of the light exiting the FPI is a geometric series [14], thus

$$E_T = t^2E_0 + t^2r^2E_0e^{i\varphi} + t^2r^4E_0e^{i2\varphi} + ... = \frac{E_0t^2}{1 - r^2e^{i\varphi}}. \tag{6}$$

The intensity of an electromagnetic field is directly related to the amplitude [15], $I = |E|^2$, so the transmitted intensity can be written as

$$\begin{aligned} |E_T|^2 &= \frac{|E_0t^2|^2}{|1 - r^2e^{i\varphi}|^2} = \frac{|E_0|^2T^2}{|1 - Re^{i\varphi}|^2} \\ |E_T|^2 &= \frac{|E_0|^2T_\lambda^2}{(1 - R_\lambda e^{i\varphi})(1 - R_\lambda e^{-i\varphi})}, \end{aligned} \tag{7}$$

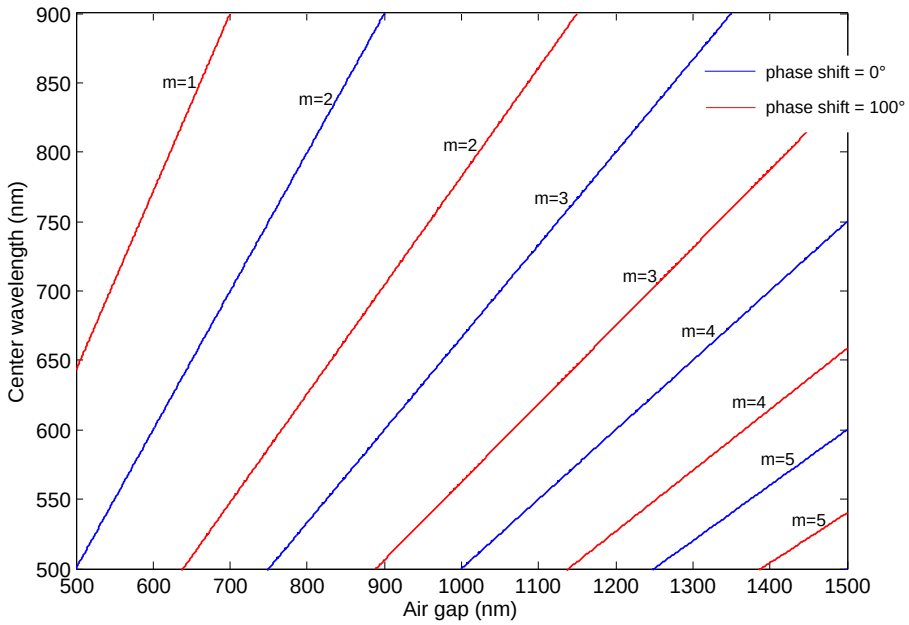

Figure 3: The relationship between air gap and the center wavelength for different orders of interference as given by Equation 5. Note how the phase shift affects the position of the curves. $n = 1$, $\theta = 0$, $\epsilon_\lambda = 0°/100°$.

where $T_\lambda = |t|^2$ and $R_\lambda = |r|^2$. These are sometimes called the intensity transmission and reflection coefficients. After expanding the term $(1-R_\lambda e^{i\varphi})(1-R_\lambda e^{-i\varphi})$, it takes the following form [16]

$$1 - 2R_\lambda \cos\varphi + R_\lambda^2 = (1 - R_\lambda)^2 \left[1 + \frac{4R_\lambda}{(1 - R_\lambda)^2} \sin^2 \frac{\varphi}{2}\right]. \tag{8}$$

By denoting

$$\tau_\lambda = \frac{|E_T|^2}{|E_0|^2}, \tag{9}$$

and substituting (8) into (7) the relative intensity transmission becomes

$$\tau_\lambda = \frac{T_\lambda^2}{(1 - R_\lambda)^2} \left[1 + \frac{4R_\lambda}{(1 - R_\lambda)^2} \sin^2 \frac{\varphi}{2}\right]^{-1}. \tag{10}$$

The latter part of Equation 10 is called the Airy function [13, 14]:

$$A(\varphi, R_\lambda) = \left[1 + \frac{4R_\lambda}{(1 - R_\lambda)^2} \sin^2 \frac{\varphi}{2}\right]^{-1}, \tag{11}$$

which, in a loss-less case, is the transmission of the FPI (see Figure 4).

In the most simple ideal case, $T_\lambda + R_\lambda = 1$, the angle of incidence is zero and no phase shift is caused by reflections. In this case, the Airy function is often expressed as [15]

$$\tau_\lambda = \frac{1}{1 + F' \sin^2 kd}, \tag{12}$$

where $k = 2\pi/\lambda$ and $F' = 4r^2/(1-r^2)^2$. F' is also known as the Coefficient of Finesse, which can be used to define the quality of FPI mirrors.

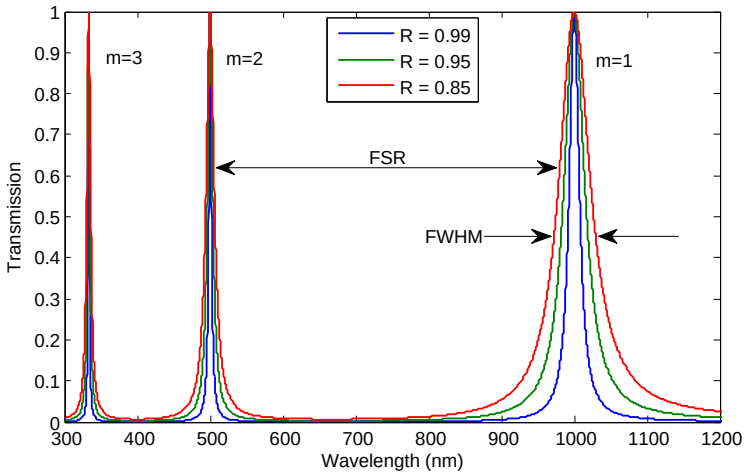

Figure 4: The Airy function, showing orders 1, 2 and 3 for air gap of 500 nm. Note how the reflectivity R affects the FWHM. The distance between two peaks is called the Free Spectral Range (FSR). Phase shift and angle of incident are both zero in this case.

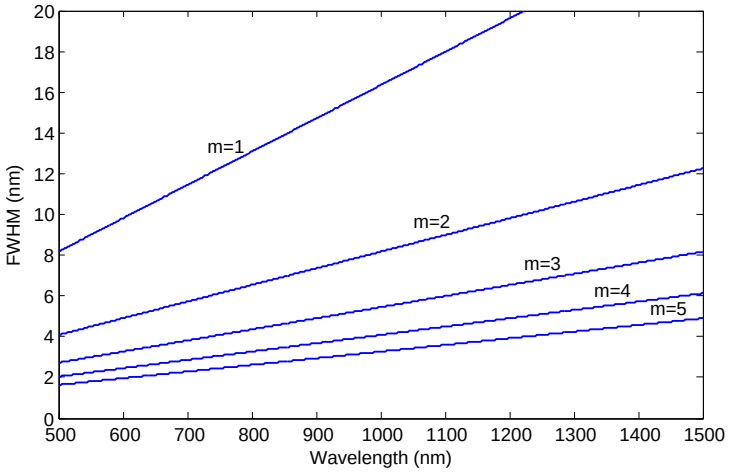

Figure 5: The theoretical FWHM for different orders as a function of wavelength, $R_\lambda = 0.95$.

The Airy function shows that the transmission of the Fabry–Perot Interferometer has narrow passbands at different orders of interference, i.e. at different wavelengths. The width and position of the passbands depend on the reflectivity of the mirrors and the distance between the mirrors. The order of interference also affects the peak width, as at higher orders the peaks are narrower. The distance between transmission bands is called the Free Spectral Range (FSR, Equation 13) and peak width is usually measured at the 50% of the maximum value. The full-width at half-maximum (FWHM, Equation 14) is often used as a measure of spectral resolution, which is illustrated in Figures 4 and 5. Another figure of merit for the FPI is the reflective finesse (N_r, Equation 15), which describes the sharpness of the peaks. It is defined to be the ratio of distance between successive transmission peaks, $N_r = \frac{FSR}{FWHM}$. [16, 17]

$$FSR = \frac{\lambda_{m+1}}{m} \tag{13}$$

$$FWHM = \frac{\lambda}{m\pi}\frac{(1-R)}{\sqrt{R}} \tag{14}$$

$$N_r = \frac{\pi\sqrt{R}}{(1-R)} \tag{15}$$

The reflective finesse N_r can be used to rewrite the Airy function:

$$A(\varphi, R) = \left[1 + \left(\frac{2N_r}{\pi}\right)^2 \sin^2\frac{\varphi}{2}\right]^{-1}, \tag{16}$$

However, the equations shown above apply only to the ideal Fabry–Perot Interferometer. In real devices there are several aspects which differ from the ideal case, as many of the parameters assumed constant are wavelength-dependent in reality [16, 17]:

1. The reflection and transmission coefficients are wavelength dependent, thus a wavelength dependence must be added to the equations shown above.

2. There is a wavelength-dependent phase shift upon reflection at the mirrors. Equation 4 takes this into account.

3. Some absorption occurs in the mirrors and coatings. This absorption is also wavelength-dependent. The absorption can be described by $\alpha_\lambda = 1 - T_\lambda - R_\lambda$.

4. The mirrors are not completely flat nor are they completely parallel. Often the difference of the largest and smallest air gap within an FPI aperture is named peak-to-valley (P-V), which is a very common measure for flatness. Characterization and measurement of these defects is explained in Chapter 6.

It is possible to take these defects into account [17]. For accounting for defects, a concept of effective finesse can be used. The effective finesse takes into account all possible sources of peak broadening:

$$\frac{1}{N_{\text{eff}}^2} = \frac{1}{N_r^2} + \sum \frac{1}{N_i^2}, \tag{17}$$

where N_i denotes the different defect finesses (N_D).

Several aspects contribute to N_i. Three major aspects are the deformation of the mirrors, wedging of mirrors and surface irregularities of the mirrors. All these effects should be small compared to the air gap. Mirror deformation, which has the maximum amplitude δd_s, produces a defect dinesse $N_{D,s} = \lambda/(2\delta d_s)$ and a wedge, which has the maximum amplitude of δd_w, produces a defect finesse $N_{D,w} = \lambda/(\sqrt{3}\delta d_w)$. If the surface irregularities follow a normal distribution with a standard deviation of δd_i, then the associated defect finesse $N_{D,i}$ is $\lambda/(4.7\delta d_i)$ [17]. Thus the net defect finesse is

$$\frac{1}{N_D^2} = \frac{1}{N_{D,s}^2} + \frac{1}{N_{D,w}^2} + \frac{1}{N_{D,i}^2}. \tag{18}$$

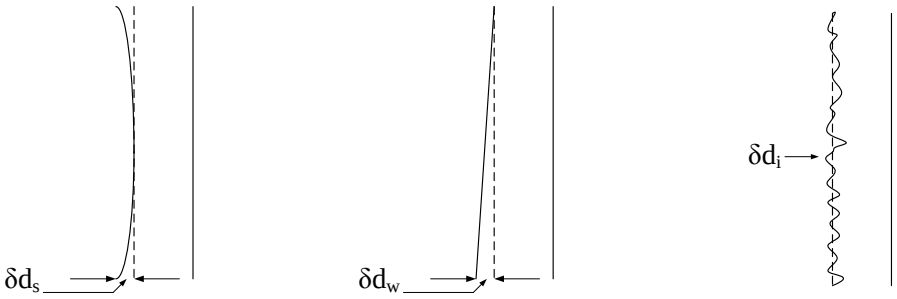

(a) Mirror deformation (b) Mirror wedging (c) Surface irregularities

Figure 6: The causes for defect finesse. [17]

In addition to this, there is deviation in the ray angles of a beam of light entering the FPI. This causes the peak to broaden, as can be seen from Equation 5: beams coming in different angles constructively interfere at slightly different wavelengths. This can be taken into account by defining aperture finesse [17]:

$$N_A = \frac{2\pi}{m\Omega}, \tag{19}$$

where m is the order of interference and Ω is the solid angle of the incoming beam. This leads to the general effective finesse

$$\frac{1}{N_{\text{eff}}^2} = \frac{1}{N_r^2} + \frac{1}{N_D^2} + \frac{1}{N_A^2}, \tag{20}$$

which can be used to correct the Airy function. Also by including the absorption, $\alpha_\lambda = 1 - T_\lambda - R_\lambda$, the transmission function of an FPI becomes

$$\tau_\lambda = \left(\frac{T_\lambda}{\alpha_\lambda + T_\lambda}\right)^2 \left[1 + \left(\frac{2N_{\text{eff},\lambda}}{\pi}\right)^2 \sin^2\frac{\varphi}{2}\right]^{-1}. \tag{21}$$

Equation 21 can be used to estimate the behaviour of real FPI's, if the non-idealities are known. The effect of these non-idealities is demonstrated in Figure 7.

From the equations given in this chapter, it can be seen that a tunable Fabry–Perot filter can be achieved in three different ways: by tuning the air gap, by tilting the FPI mirrors or by changing the index of refraction inside the FPI cavity. In AaSI, the tunability is achieved by moving the mirrors by piezo-electric actuators, as precise piezo-electric actuators are easily available commercially.

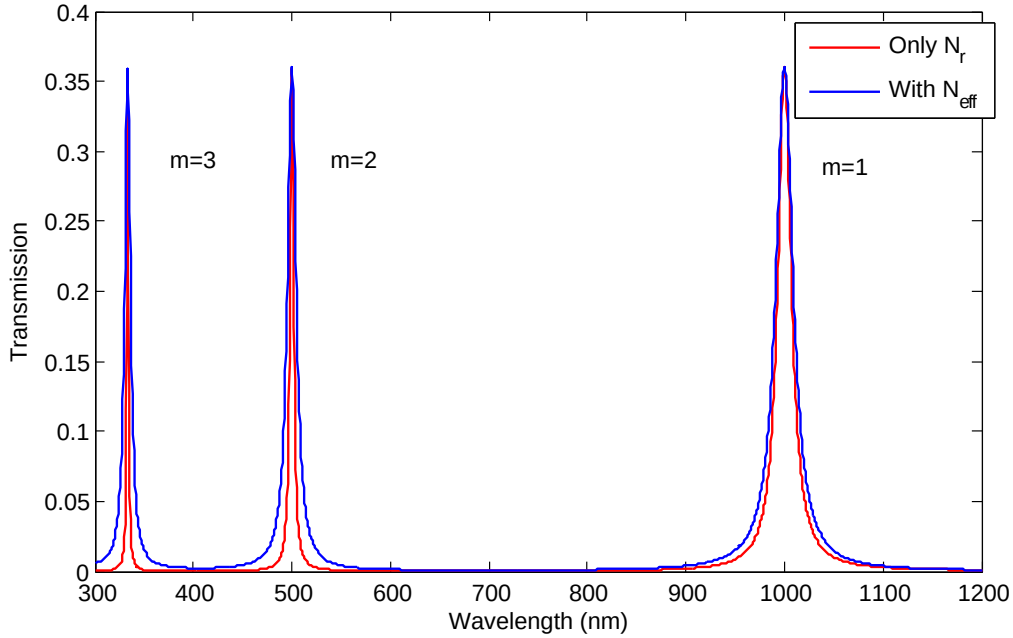

Figure 7: The effect of defective finesse. Higher order peaks are slightly broadened compared to the ideal case. In reality the broadening also decreases the peak height, which is not taken in to account here. $\delta d_\mathrm{s} = 10$ nm, $\delta d_\mathrm{w} = 0$ nm and $\delta d_\mathrm{i} = 4.34$ nm. Incoming beam angle difference was estimated as 0.2°. Defects were estimated from previous experience and manufacturer data [18]. d=500 nm, $\alpha = 0.02$, $\epsilon = 0$, $R = 0.95$.

2.2 Applications

The main advantage of the FPI is its high throughput compared to prism or grating spectrometers [19]. It has been applied to various spectroscopic applications over a wide wavelength range from ultraviolet (UV) to thermal infrared. This allows the construction of compact and efficient filters or monochromators [17]. Traditionally Fabry–Perot Interferometers have been used at very high orders (e.g. $m = 300$–1000), where high spectral resolving power can be achieved. This method has been used to study the fine structure of spectral lines [13], but it is limited by small FSR, as shown by Equation 13. The Large Angle and Spectrometric Coronagraph Experiment (LASCO) on board the SOHO spacecraft is one example of where this kind of high resolving power FPI's have been used [8]. However, it is difficult to produce high quality FPI's with very large mirrors [19, 20], so high-luminosity applications still often use large gratings or prisms for spectral sorting.

More recently spectral imagers operating on lower orders of interference have appeared. A hyperspectral imager based on piezo-actuated FPI's for unmanned aerial vehicles has been developed by VTT Technical Research Centre of Finland [10, 21]. A tunable filter imager based on a FPI was also planned for the James Webb Space Telescope (JWST), but the concept was abandoned in 2011 [20] due to issues with cryogenic performance.

FPI's are also used extensively in telecommunications and laser technology [22, 23], but these applications are not related to this thesis, so they are not covered here.

3 Spacecraft Environment

Spacecraft operations are characterized by their remoteness and harsh environment, as they have left the protection of Earth's atmosphere, and in some cases, also Earth's magnetosphere. The missing protection from the atmosphere can expose the spacecraft to hazards that are not seen on ground.

3.1 Effects during the launch campaign

As launching a satellite is a very complex procedure, it may take months or even years after integration of the satellite before it reaches its final destination. This means that the satellite systems must be unaffected by long periods of storage, if possible. During launch, the satellite is exposed to severe acoustic and mechanical vibrations caused by the launcher itself. The vibration magnitude is often given as the acceleration spectral density (ASD), g^2 Hz^{-1}, i.e. the power spectral density of the vibrational acceleration. As an example, the random vibration spectrum of Ariane 4 launch vehicle is shown in Figure 8. The figure shows that the random vibration induced root-mean-square (RMS) acceleration directed to the payload will be 7.3g's. Also as all current rockets are multi-stage rockets, severe shocks can be present at stage separation phases. For example, during an Ariane 4 launch, momentarily accelerations can reach 2000g's [24], which may cause shock-sensitive structures to fracture or break. The launch vehicle environment will define the characteristics for vibration and shock testing, which are explained in Chapter 5.

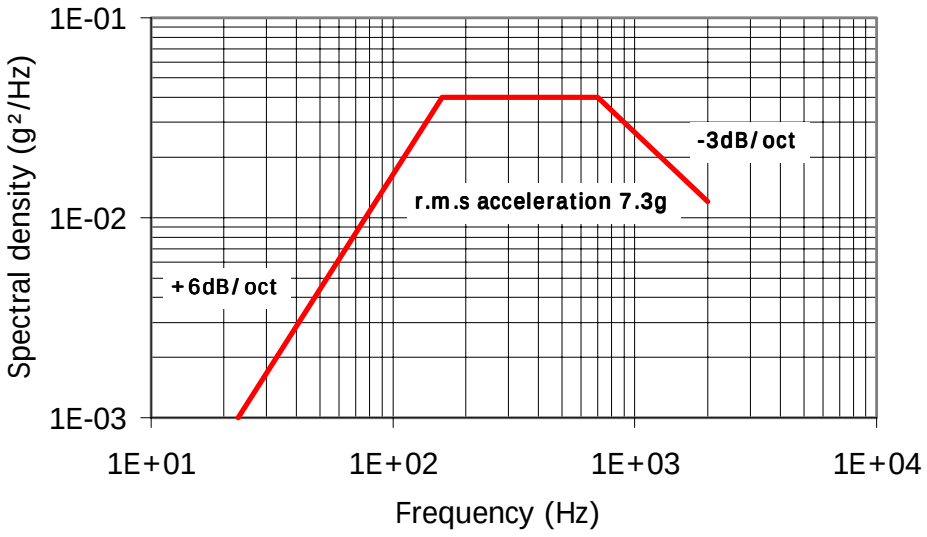

Figure 8: Ariane 4 vibration spectrum. [24]

3.2 Thermal environment

As there is an almost perfect vacuum even on the low Earth orbit (LEO), most of the thermal energy is transferred by radiation. Dark space is also very cold, with the cosmic background radiation being only 2.7 Kelvins. On the low Earth orbit, the most significant heat flux (ca. 1370 W/m^2) comes directly from the Sun and this will cause sun-facing surfaces to heat considerably. On LEO there is also reflected radiation (albedo) and the thermal radiation of the Earth, called the earthshine. The magnitude of the earthshine is ca. 200 W/m^2, which is not very much, but it has to be taken into account during the thermal design of a spacecraft. [2]

For ideal black bodies radiative heat exchange is simple: an object absorbs all radiation, which causes the object to aquire a certain temperature, which causes the object to radiate an equal amount of energy in order to remain at thermal equilibrium. The energy radiated by a black body at temperature T is given by the Stefan-Boltzmann law

$$J = \sigma T^4, \tag{22}$$

where σ is the Stefan-Boltzmann constant[1]. However, satellites are not black bodies, as they absorb only a fraction of the incident radiation and emit only a fraction of the the black body radiation. Thus, for the equilibrium temperature the following equation can be written:

$$A_\alpha \alpha J_{incident} = A_\epsilon \epsilon \sigma T^4, \tag{23}$$

where A_α and A_ϵ are the areas absoring and emitting radiation and α and ϵ are constants, which define the fractions of absorption and emittance. These coefficients are called the absorptivity and emissivity. From this the equilibrium temperature for any object can be written as

$$T = \sqrt[4]{\frac{A_\alpha}{A_\epsilon} \frac{J_{incident}}{\sigma} \left(\frac{\alpha}{\epsilon}\right)}. \tag{24}$$

Equation 24 shows that the equilibrium temperature can be adjusted by tuning the value of α/ϵ. However, according to the laws of thermodynamics, α and ϵ must be equal to each other at the same wavelength. This does not hinder the thermal design of a spacecraft, because most of the absorbed radiation is at visible wavelenghts, and all of the emitted radiation is at infrared wavelengths, so the absorptivity is actually 'solar absorptivity' and the emissivity is actually 'infrared emissivity'. In principle, all thermal effects in a spacecraft follow this equilibrium. [2] Accurate modeling of the thermal environment is difficult, so it is critical to also verify the calculations with testing. Details of the thermal tests for AaSI are described in Chapters 6 and 8.

[1] $\sigma = 5.670 \times 10^{-8}$ W m^{-2} K^4

3.3 Radiation environment

The radiation environment on low Earth orbit is rather harsh compared to ground level. The biggest threat to satellites is the ionizing radiation, which is mainly caused by the trapped charged particles in the Van Allen belts. The environment can be roughly divided in two regions: region below 800 km is dominated by protons and the region above is dominated by electrons. There may also be trapped ions of Helium, Nitrogen and Oxygen in addition to protons and electrons. The accumulating total dose will degrade all semiconductor materials, such as processors and memory chips. Another problem are the single event effects. These are normally caused by high energy particles, which are absorbed by the semiconductor materials. The most common effect is the single-event upset (SEU), in which the particle gets absorbed and its charge is deposited to the semiconductor. This will cause a bit-flip in a memory bank, but its effect is reversible. More serious effect is the single-event latch-up (SEL), in which a single charged particle hits a complementary metal oxide (CMOS) material, causing a latched low impedance state in the device. In the worst case, this latched state can result in a burn out. This is even more serious in metal oxide semiconductor field effect transistors (MOSFET), as a conducting path may be formed by the impact. If this state continues the device may be completely destroyed. [2, 25]

It is possible to shield against radiation effects, wrapping the sensitive systems in aluminum shells for example. This will reduce the total dose effects, thus increasing the lifetime of the system. Shielding against single-event effects is more problematic, as the particles are so energetic that thin metal shields do not work. In these cases the system can be made redundant in both software and hardware e.g. by applying error correcting coding or duplicating critical systems. [2, 25] However, as the FPI for AaSI is an optical component made mostly of glass, it is not very radiation sensitive. Thus it is not necessary to specially shield the FPI component against radiation. Also for this reason the FPI module will not radiation tested separatedly.

3.4 Vacuum effects

One of the most critical issues with vacuum environment is the outgassing of materials. This refers to the vaporization of surface atoms of a material when it is subjected to a pressure that is comparable with its own vapour pressure. Such pressures occur already at low earth orbit and the process is accelerated as the temperature rises [2]. If the outgassing material gets deposited on optical systems (mirrors, lenses, detectors), it may affect the performance of the system. The effects can be mitigated by shielding the sensitive components and putting them to thermal vacuum bakeout, since forcing the excess material to outgas before orbit will reduce the amount of outgassing once in space. The only way to completely negate this effect is to avoid materials that have high outgassing. Material outgassing is measured by three parameters, Total Mass Loss (TML), Recovered Mass Loss (RML) and Collected Volatile Condensable Material (CVCM), and general ECSS requirements for material outgassing are RML $< 1\%$ and CVCM $< 0.1\%$ [26]. Outgassing tests

require special facilities, so they are not included in this work. However, an outgassing report from Instituto Nacional De Tecnica Aeroespacial (INTA) is included in Appendix 9.

For moving mechanical structures vacuum environment can also affect the moving parts, as air (or any medium) acts as a dampener. In vacuum this damping effect is removed, which may trigger unexpected behaviour. As the FPI used in AaSI will be a tunable filter, the vacuum tests performed in this thesis will be focused on the behaviour and endurance of the FPI module.

4 Aalto-1 Spectral Imager (AaSI)

4.1 Overview

The Aalto-1 Spectral Imager (AaSI) is a miniaturized spectral imager developed by VTT and it is capable of recording images at 20+ selectable wavelength bands between 500 and 900 nanometers. AaSI will be the main payload of the Finnish Student satellite Aalto-1 and the main operational parameters are shown in Table 1. AaSI is designed to be compatible with the CubeSat form factor [6] and it also incorporates the PC104-standard -based stack-through design, which is most common in CubeSat systems.

AaSI (Figure 9) consists of two camera modules, the main part of the instrument is the spectral camera, which includes a tunable Fabry–Perot Interferometer (FPI) and a CMOSIS CMV4000 CMOS color sensor. The second part is the visible light (VIS) camera, which is a normal red-green-blue (RGB) camera with wider field of view than the spectral camera. The VIS camera has the same CMOSIS sensor which is combined with commercial off-the-shelf optics. Both image sensors share the common control electronics in order to minimize the system complexity. [27]

Table 1: Main parameters of AaSI [27].

Wavelength range	500–900 nm
Spectral resolution	10–30 nm
Field of view	10°
Spectral image size	512 × 512 pixels
VIS image size	1910 × 1270 pixels
Number of spectral bands	> 20
Size	97 × 97 × 48 mm^3
Mass	600 g

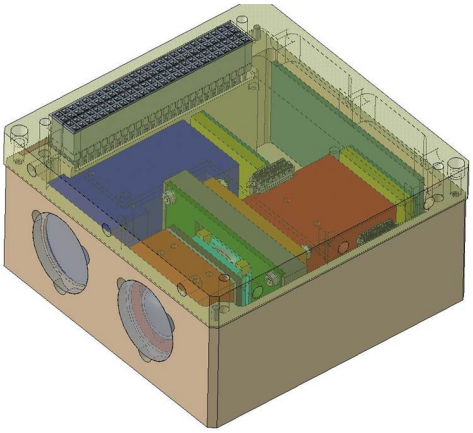

Figure 9: 3D-model of AaSI. [27]

4.2 The PFPI module design

The PFPI module is a key component in AaSI, thus it is necessary to perform a detailed characterization for the module. VTT has an internal serial number system for the PFPI's. The serial number is formed from the design type (003, 006 etc.) and the manufacturing order, e.g. PFPI-006-V035 would mean the 35th PFPI of 006-type manufactured.

The PFPI module is composed of the FPI itself and the surrounding support structure, which also houses the necessary electronics for the piezo-actuation. The FPI mirrors are made with silver coating (thickness 50 nm), on top of which a 50 nm layer of silicon dioxide (SiO_2) is deposited as a protective layer. A thin layer of titanium (4 nm) is used as an adhesive to fix all layers together [10]. These mirrors are then fixed (Figure 10) to the piezo actuators with UV-curable adhesive (Dymax OP-61). After the gluing process FPI module fixed to a fused silica support glass with another optical adhesive (Dymax OP-29), which is then fixed to the aluminum frame with 5 silicone pads (NuSil CV-1142P). The silicone pads are used to minimize thermal stresses to the FPI structure while providing sufficient mechanical support. The Dymax glues exceeds the outgassing limits (see Appendix 9) stated in the ECSS standard [26], so an alternative is being sought. However, it is assumed that the outgassing of the glue does not critically affect the performance of AaSI, as the mission goal is only to demonstrate the PFPI technology in space environment.

After the structure has been mechanically assembled, the electrical connections are made from the FPI to the printed circuit board (PCB) (Figure 11). Two types of connections are made: the wirings for capacitance measurement (Chapter 4.4) and wirings for the piezo-actuator control voltages.

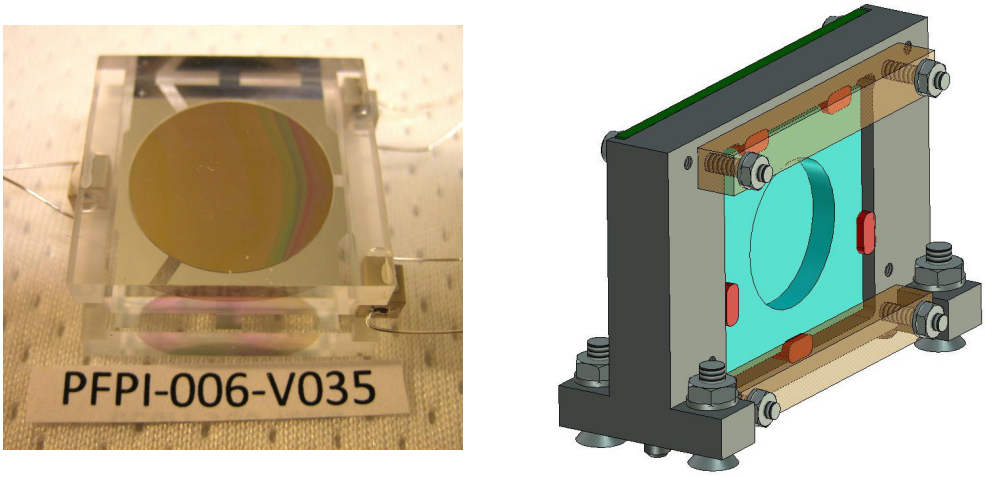

Figure 10: Left: The PFPI-006-V035 right after the piezo-actuators have been glued to the mirrors. Right: The FPI mounted to the support structure with five silicone pads (shown in red).

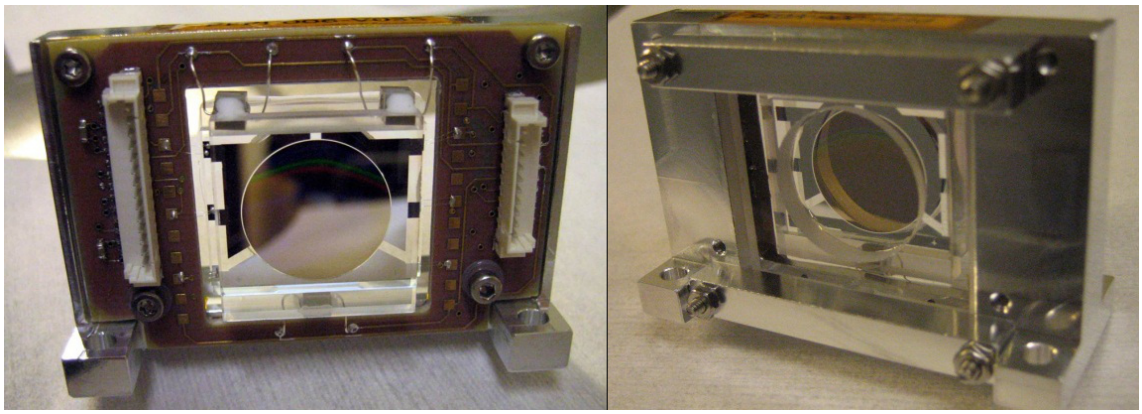

Figure 11: The PFPI module for qualification testing. The white connectors will be replaced by a flexible PCB extension in the final flight model design.

To fulfill the mission requirements [28], specifications for the FPI air gap, FWHM, transmission, CWL stability, gap change time and environment have been specified (Table 2). The air gap range, FWHM and transmission specifications define the radiometric performance of the instrument. The temperature environment is constantly changing, so the behavior of the PFPI module must be as independent of temperature as possible. However, the exact temperature range for AaSI is not yet known, so the actual range can only be estimated at this moment. In order to compensate for this, means of on-board spectral calibration are being developed [29], so the CWL stability can be improved during flight. The specifications set for the PFPI module are not extremely strict, as the nature of the mission is technology demonstration instead of hard science. For actual science mission with strict scientific requirements the PFPI specifications would be much stricter.

Table 2: Specifications for the PFPI-module. [30]

Air gap range	500–1500 nm
FWHM	10–30 nm
Transmission	0.1–0.3
Temperature compensated CWL stability for 2nd order transmission peak	0.2 nm/°C (Air gap stability 0.32 nm/°C)
Gap change time	<30 ms
Environment	Ground, launcher and LEO environment compatible.
Operating temperature range	15–45°C (TBC)
Survival temperature range	-45–65°C (TBC)
Lifetime	1 year

4.3 Spectral imaging principle

The principle of an FPI was already introduced earlier in Chapter 2.1. To use it for imaging purposes, the FPI must be combined with an image sensor (e.g. an RGB CMOS detector). If the air gap range is chosen right, there will be only one to three transmission peaks (Figure 12) at any time. Now when a transmission spectrum with one to three peaks is imaged with a normal RGB image sensor, the spectral information can be retrieved [10], as red, green and blue pixels have a different spectral response (also called the quantum efficiency) throughout the wavelength range (Figure 13). In Figure 14 the total spectral efficiency (quantum efficiency × transmission) of the detector and the FPI is shown for clarification.

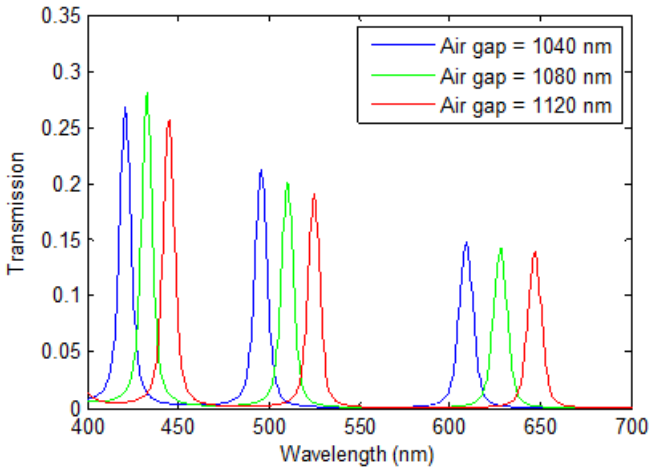

Figure 12: Simulated transmission of an FPI at three different air gaps.

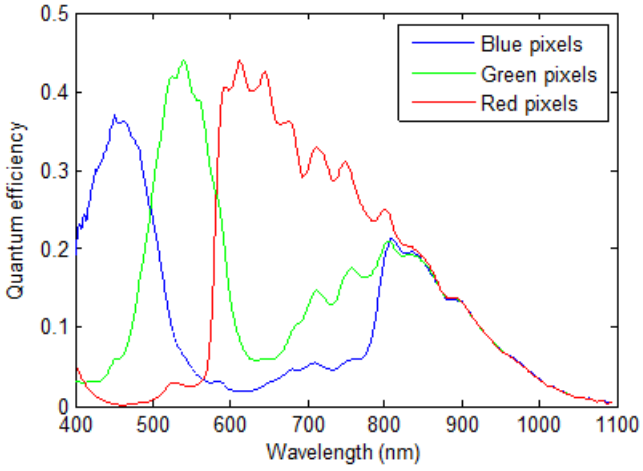

Figure 13: Measured quantum efficiency of the CMV4000 detector. (Measured by VTT)

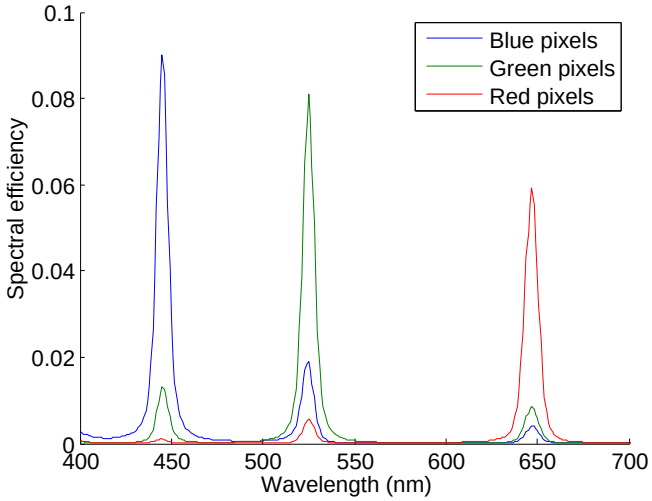

Figure 14: The total spectral efficiency of the FPI and the detector at an air gap of 1120 nm.

The different spectral responses can be measured during calibration, in which the spectral response of the image sensor (S_{Rn}, S_{Gn}, S_{Bn}) is measured as a function of the air gap and wavelength [10]. The signal measured by each pixel can be described as:

$$\begin{pmatrix} S_{Rm} \\ S_{Gm} \\ S_{Bm} \end{pmatrix} = \begin{pmatrix} S_{R3} & S_{R2} & S_{R1} \\ S_{G3} & S_{G2} & S_{G1} \\ S_{B3} & S_{B2} & S_{B1} \end{pmatrix} \cdot \begin{pmatrix} \Phi_3 \\ \Phi_2 \\ \Phi_1 \end{pmatrix}, \tag{25}$$

where S_{Rm}, S_{Gm} and S_{Bm} are the signals of the red, green and blue pixels, and Φ_1, Φ_2 and Φ_3 are the unknown spectral photon fluxes at different transmission bands. Now when the responses S_{Rn}, S_{Gn} and S_{Bn} are known from calibration, the spectral photon fluxes can be resolved by the following equation:

$$\begin{pmatrix} \Phi_3 \\ \Phi_2 \\ \Phi_1 \end{pmatrix} = \begin{pmatrix} S_{R3} & S_{R2} & S_{R1} \\ S_{G3} & S_{G2} & S_{G1} \\ S_{B3} & S_{B2} & S_{B1} \end{pmatrix}^{-1} \cdot \begin{pmatrix} S_{Rm} \\ S_{Gm} \\ S_{Bm} \end{pmatrix}. \tag{26}$$

This concept makes it possible to measure up to three spectral channels at once if necessary. In the AaSI mission the raw data (S_{Rm}, S_{Gm} and S_{Bm}) is downlinked to a ground station, where Equation 26 is used to convert the raw data to spectral data cubes, which contain both the spatial and spectral information of a target. In other words, a spectral datacube also holds the spectral information for every spatial pixel.

4.4 FPI control

The main functional blocks of AaSI are shown in Figure 15. There are three main parts: The FPI controller, the image sensor memory controller and the main microcontroller which acts as the main interface (I/F) between the on-board computer (OBC) and AaSI. AaSI is also directly connected to the Electrical Power System (EPS) of the satellite by two voltage lines +5 V and +12 V.

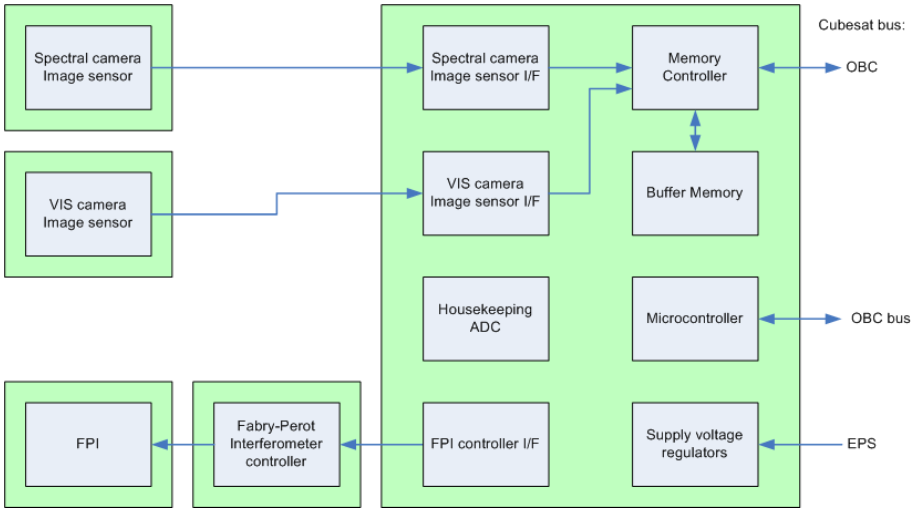

Figure 15: Block diagram of AaSI electronics.

Both image sensors have a global shutter function, so every pixel is exposed simultaneously. The image sensor data is transferred over four LVDS lines to the memory controller FPGA, which moves the data to the buffer memory. In AaSI a 32 MB SDRAM is used as the buffer memory, and it can hold the data of 16 megapixels. The same FPGA will also be used to send the image data to the OBC over and SPI-over-LVDS link. The main microcontroller manages all the communication with the OBC and the synchronization of FPI and image sensor functions. It will also manage the necessary housekeeping data. The controller is connected to the satellite-wide I^2C bus, which is used for command and telemetry transfer. The maximum power consumption is 3 W from the +5 V supply voltage line and 4 W from the +12 V line. The total power consumption depends on the operational mode of AaSI (Table 3). [27]

Table 3: Power consumption for different operational modes of AaSI. [27]

Mode	**Power consumption (5 V / 12 V)**
Off	0 W / 0 W
Idle	3 W / 0 W
Imaging	3 W / 4 W
Data transfer	3 W / 0 W

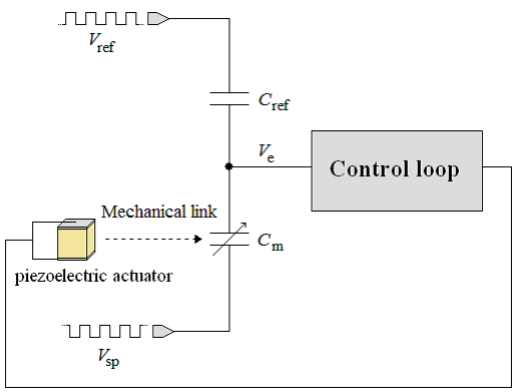

Figure 16: The controlling principle of the FPI. [21]

The FPI air gap is controlled by measuring the capacitance between the electrodes deposited on the mirror substrates and adjusting the gap by three piezoelectric actuators mounted between the mirrors. The interferometer control is based on a nulling capacitive half-bridge, shown in Figure 16. The operational principle of the bridge is straightforward: a reference signal, V_{ref} is applied to a reference capacitor (C_{ref}), while another signal (V_{sp}) is applied to the capacitor C_m, which is formed by the electrodes on the FPI mirrors. Now an error signal V_e is produced unless $V_{ref}C_{ref}$ equals $V_{sp}C_m$. When V_e is not zero, the control loop will adjust the air gap with piezo-electric actuators until V_e disappears. By adjusting V_{sp} the air gap can be set to the desired value, thus the name: set point voltage. All three actuators have their own closed control loops and voltages, so the set point voltages for the three actuators are called set points 1, 2 and 3 (SP1, SP2 and SP3). The set point values control the air gap at each actuator and thus all of them have to be calibrated together to get a parallel air gap. The air gap control principle is illustrated in Figure 17. The calibration procedure is explained in the next chapter. [21, 31]

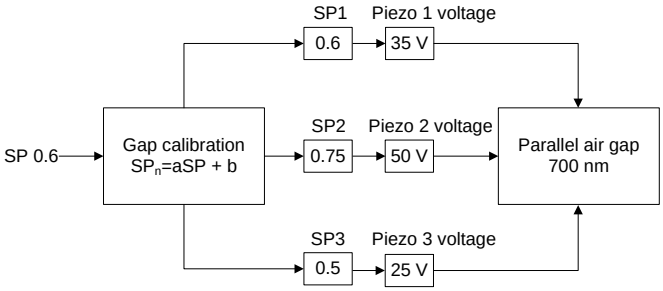

Figure 17: Air gap tuning principle with some values as an example. A single set point value is given to the FPI from which the other two set point values are calculated. Together these three set points define the voltages for each piezo actuator required for a parallel air gap.

4.5 FPI calibration

Before the PFPI can be used for measurements, a gap calibration has to be performed. The gap calibration ensures that the FPI mirrors are parallel throughout the operational gap range, e.g. from air gap values of 500 nm to 3000 nm. The gap calibration is performed by straightening the air gap at 10 to 20 different air gaps and set point values for each piezo actuator are recorded at each gap value, and the relationships between SP1, SP2 and SP3 are then calculated. As Figure 18 shows, the relationship is almost linear, which means that the calibration should be valid within the calibration range.

It is also necessary to confirm that the gap calibration is valid over the operational temperature range. This was done by performing gap calibration for PFPI-006-V035 at different temperatures, ranging from ca. 5°C to 55°C. Now when the calibration curves at the temperature extremes were compared, a small difference was found. However, the difference is so small that its effect is assumed negligible to the parallelism of the air gap. The average difference for both SP2 and SP3 is less than 1% (Figure 19).

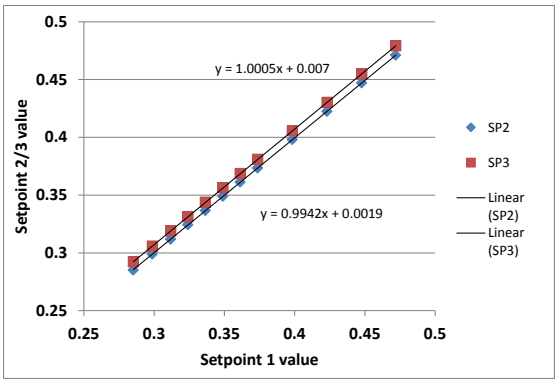

Figure 18: Gap calibration of PFPI-006-V035. Normalized with SP1.

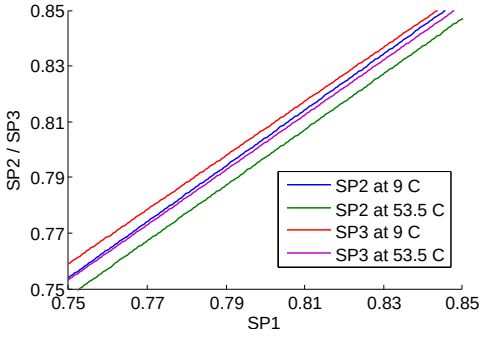

Figure 19: The set point calibration in two temperatures. A small difference is seen, but the average difference between set points at high and low temperatures is less than 1% when calculated over the whole calibration range.

4.6 Performance simulations

As was mentioned in Chapter 2, the mathematical model of the FPI does not exactly reflect reality. In real life the mirrors and coatings have non-zero thicknesss, which affects the reflections. The FPI transmission is also affected, as the silver used for mirror coatings has wavelength-dependent absorption [32]. To take these effects into account, a more realistic simulation with a numerical thin-film simulation software has to be used. These simulations have been performed at VTT in earlier projects, and they also apply to the FPI used in AaSI. CWL, FWHM and transmission simulations of the FPI used in AaSI are shown in Figures 20 and 21. These simulations have been made at VTT with Filmwizard^{TM}thin-film simulation software, and should reflect the actual FPI quite well. [27]

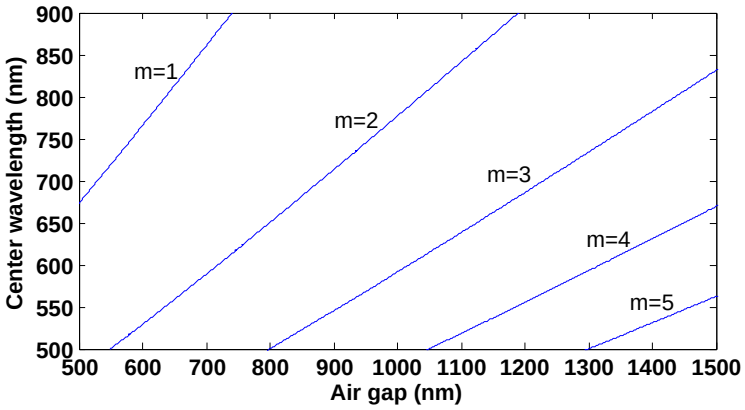

Figure 20: The simulated peak positions for different orders of interference. A small difference can be seen when compared to the theoretical curves with 100° phase shift in Figure 3. [27]

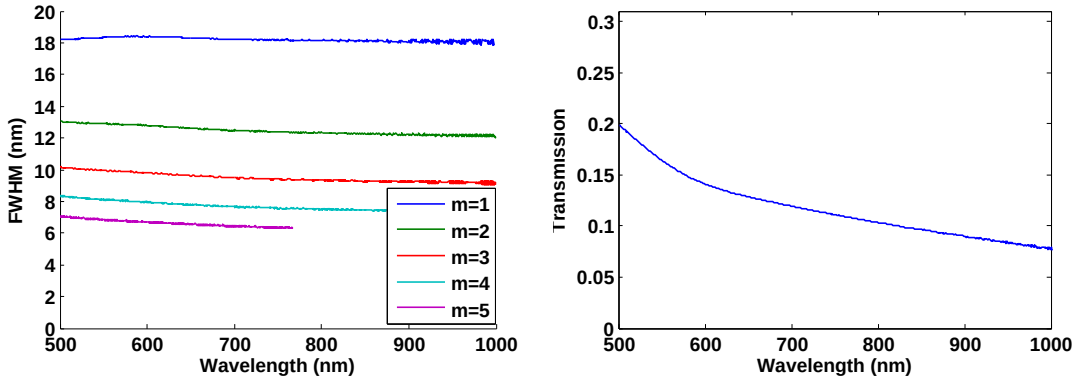

Figure 21: Simulated FWHM for different orders as a function of wavelength (left) and the simulated transmission of the PFPI as a function of wavelength. There is a significant difference to the theoretical FWHM values in Figure 5. This difference in FWHM curves is caused by the non-idealities of the mirrors. The drop in transmission is caused by wavelength-dependent absorption in the metallic mirrors.[27]

5 Vibration and Shock Testing

5.1 Testing procedures

The vibration tests were performed at VTT Expert Services with an LDS V875 Electrodynamic Shaker. Maximum force, acceleration and amplitude for the shaker were 40 kN, 1000 ms^{-2} and 50 mm. The shock test was performed by a free falling or impact hammer and the shock spectrum was measured with Dactron Laser USB-system. The vibration and shock tests are performed for all three coordinate axes (Figure 22) and the test levels (Table 4 and Figure 23) were derived from the General Environmental Verification Standard [33], as the launcher for Aalto-1 has not yet been confirmed. This standard defines that the Acceleration Spectral Density (ASD) must be 0.026 g^2 Hz^{-1} at 20 Hz and at 2000 Hz frequencies and 0.16 g^2 Hz^{-1} at 50–800 Hz. Between these limits the ASD is increased (decreased) by 6 dB/octave and the overall RMS acceleration is 14.1 g's.

During the vibration test, the test item is subjected to random vibration along each of the three mutually perpendicular axes for one minute each. During the shock test, the test item is subjected to 3 shocks from +X, -X, +Y and -Y directions and 6 shocks from +Z direction, 18 shocks in total. The geometry of the PFPI module prevents performing the shocks from -Z direction. The complete test procedure is explained in more detail in Appendix 9.

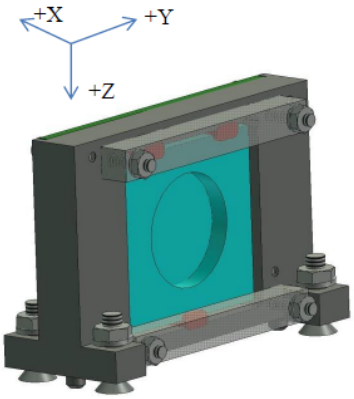

Figure 22: Coordinate axes of the PFPI modules for the vibration tests.

The functionality of the FPI will be confirmed after each vibration/shock direction. The functional test will involve measuring the air gap from a single point at 6 different set point values. In addition to this, the voltages generated by the piezo-electric actuators will be measured constantly during the tests, as there is concern that the voltage generated by the actuators will damage the control electronics. The measurement is performed by connecting the actuators to a Tektronix MSO2024 oscilloscope.

Table 4: Generalized Random Vibration Test Levels, duration one minute. [33]

Freq. (Hz)	**Qualification ASD** (g^2/Hz)
20	0.026
20–50	+6 dB/oct
50–800	0.16
800–2000	-6 dB/oct
2000	0.026
Overall	14.1 G_{rms}

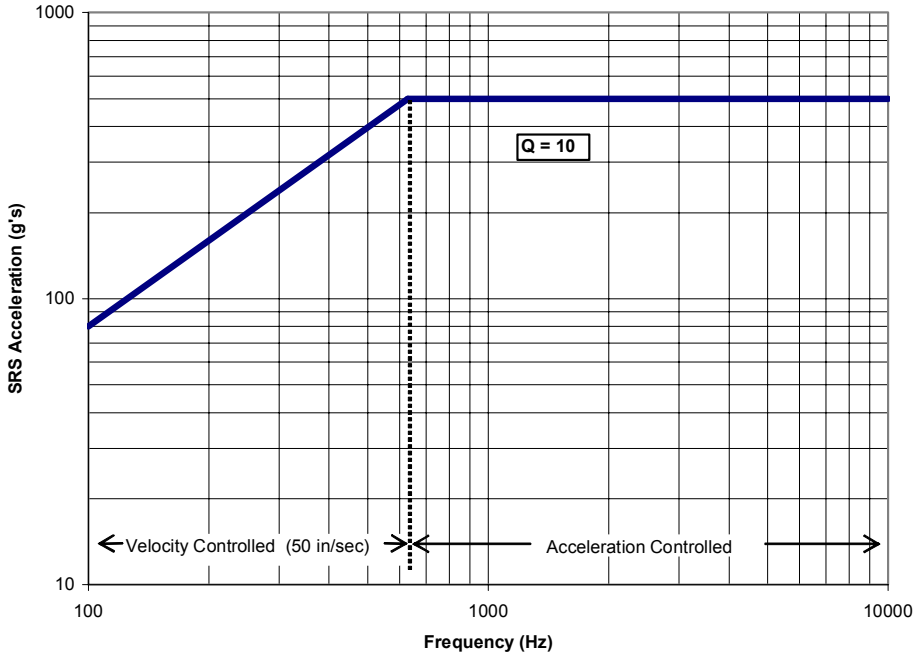

Figure 23: The shock response spectrum as given by the GSFC-STD-7000 standard. [33]

5.2 Results

5.2.1 Test 1: Random vibration (PFPI-006-V035)

The first test was performed on module PFPI-006-V035. Voltages generated by the piezo actuators were measured with an oscilloscope during the vibration tests. The results are shown in Figure 24, which shows that high voltages were not generated. The average voltage levels remained under 1 V.

A functional test was performed for the PFPI module after the X-axis vibration and no change in operation was observed. However, after the Y-axis vibration, the PFPI could not be controlled anymore. Closer inspection with a microscope revealed that the bonding wires for the capacitance measurement had been cut. The reason

for this was the fact that the mirror element had more room to move than the bonding wires were long, due to the flexibility of the silicone glue used to fix the mirror element to the aluminum frame. This resulted in snapping of the bonding wires (Figure 25) when there was no more slack left. After analysing the results, it was concluded that a re-design of the module was required.

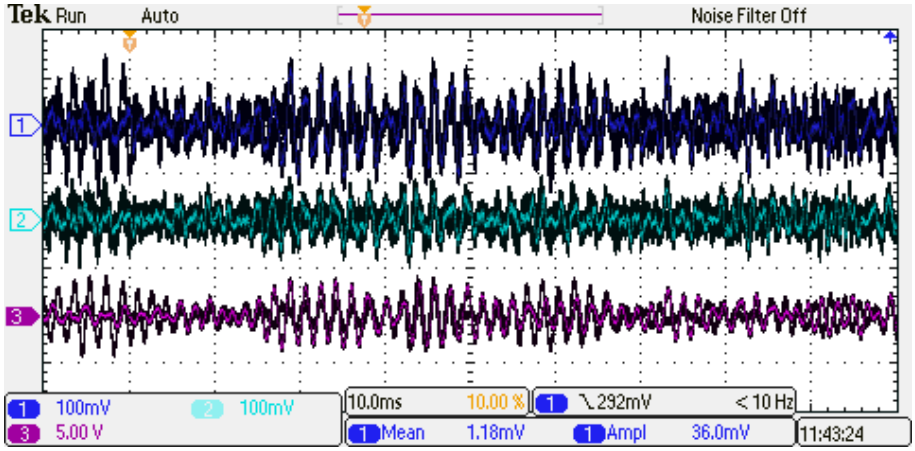

Figure 24: Voltages generated by the piezo actuators during random vibration test. 100 mV/div for channels 1 and 2, the 5 V shown in the image for channel 3 is actually 500 mV/div.

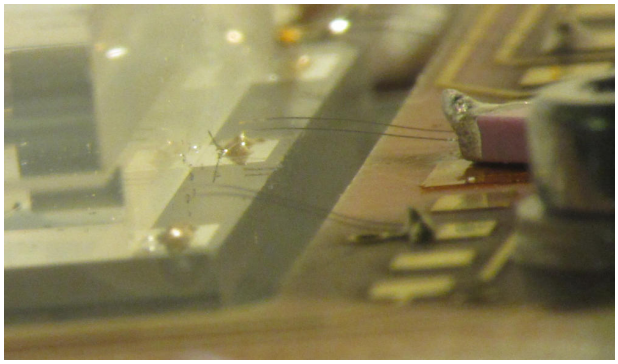

Figure 25: Broken bonding wires.

5.2.2 Test 2: Random vibration (PFPI-006-V033)

The design of the PFPI module was altered in order to correct the problem found in the first test. Instead of bonding the electrodes directly to the amplifier PCB, the electrodes were bonded to small PCBs on the same mirror element. From these PCBs the connection to the amplifier PCB was done by soldering thicker wires to both cards (Figure 26). The PFPI-006-V033 module was used for this test.

During the second test, the voltages generated by the piezo elements were measured also with a 30 to 50 V bias, but no large difference to earlier measurement was found (Figure 27). Functional tests were performed after each vibration direction

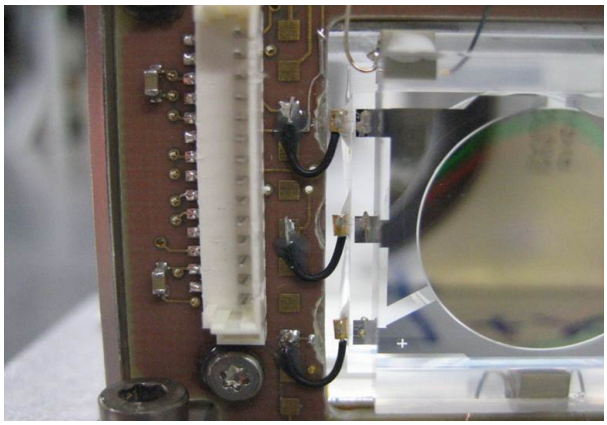

Figure 26: New design for bonding wires.

(Table 5), but no change in behavior could be observed. There were no anomalies in the FPI control and the gap calibration remained valid, as the same set points resulted in the same air gap. Some deviation in the air gap measurements can be seen, but it is most likely caused by the inaccurate gap measurement based on reflection spectrum instead of transmission. The initial gap measurement for set point 1.1 was incorrectly correlated, thus the air gap value in parentheses is incorrect in Table 5.

Table 5: PFPI functional test results during vibration test X, Y and Z columns denote the gap values in nanometers measured after each vibration direction. Also the average and the standard deviation are added for each set point. The first gap measurement for set point 1.1 was noticed to be erroneously measured and it is not included in the analysis, thus the parentheses.

Set point	Gap before test (nm)	X (nm)	Y (nm)	Z (nm)	Average (nm)	SD (nm)
0.6	694	694	693	690	692.8	1.9
0.7	1098	1098	1098	1097	1097.8	0.5
0.8	1505	1504	1504	1501	1503.5	1.7
0.9	1912.5	1909	1903	1901.5	1906.5	5.1
1.0	2323.5	2315	2314	2315	2316.9	4.4
1.1	(2356)	2730	2731	2733	2731.3	1.5

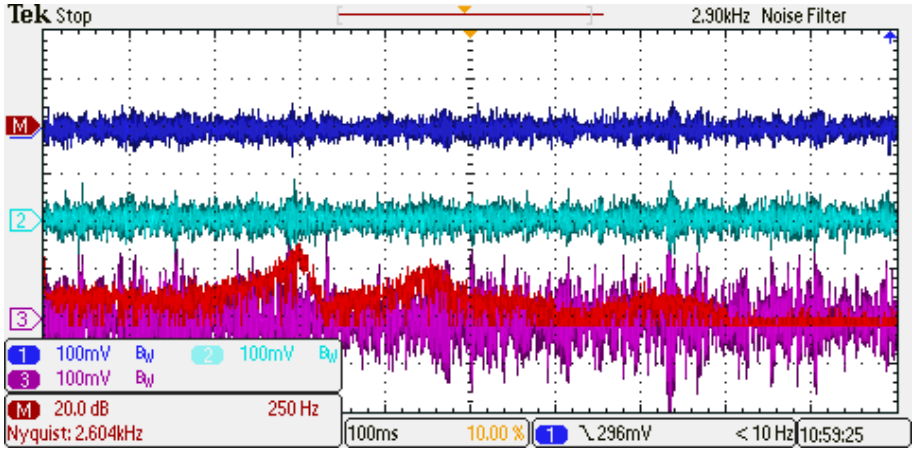

(a) No bias, 25% vibration levels

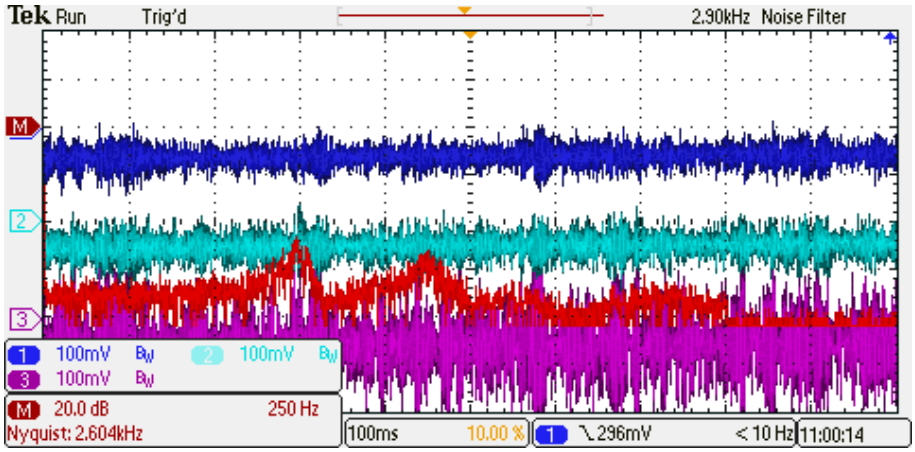

(b) 30 V bias, 25% vibration levels

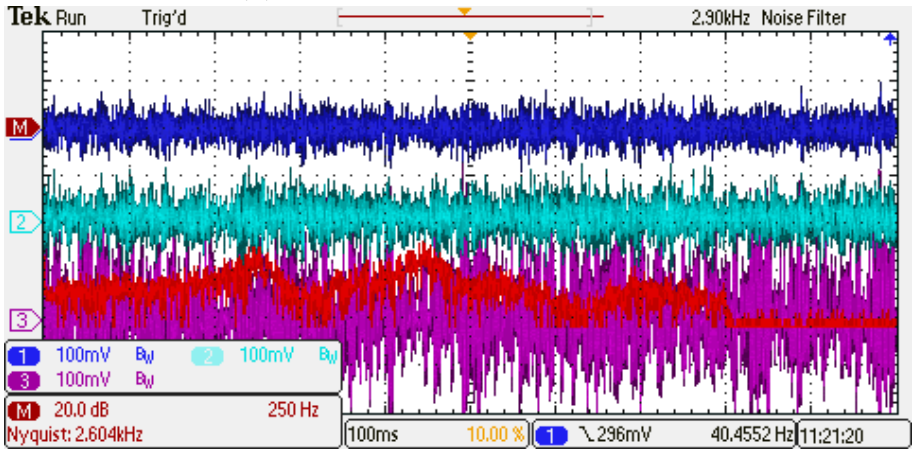

(c) No bias, 100% vibration levels

Figure 27: Voltages generated by the piezo actuators during random vibration test. 100 mV/div for channels 1, 2 and 3. Highest generated voltages were less than 300 mV with 100% levels. The red curve shows the frequency spectrum of the vibration.

5.2.3 Test 3: Shock (PFPI-006-V033)

During the shock test it was noticed that the achieved shock spectrum was different from the ideal one given by the standard (Figure 23). The actual shock spectrum had strong peaks around 1 and 2 kHz, which means that the actual shock (Figure 28) was stronger than required by the standard. Even so, no malfunctions were found during the test. An offset in the air gap can be seen for some set points between vibration and shock tests, but it is impossible to say if it is caused by measurement error or the shock test itself. The magnitude of this offset varies from 5 to 8 nm, for set points 0.6, 0.7, 0.8 and 1.1, but it is not present for set points 0.9 and 1.0. Generally no anomalies were found in the FPI operation, and the deviation seen in the air gap is most likely caused by the inaccurate gap measurement.

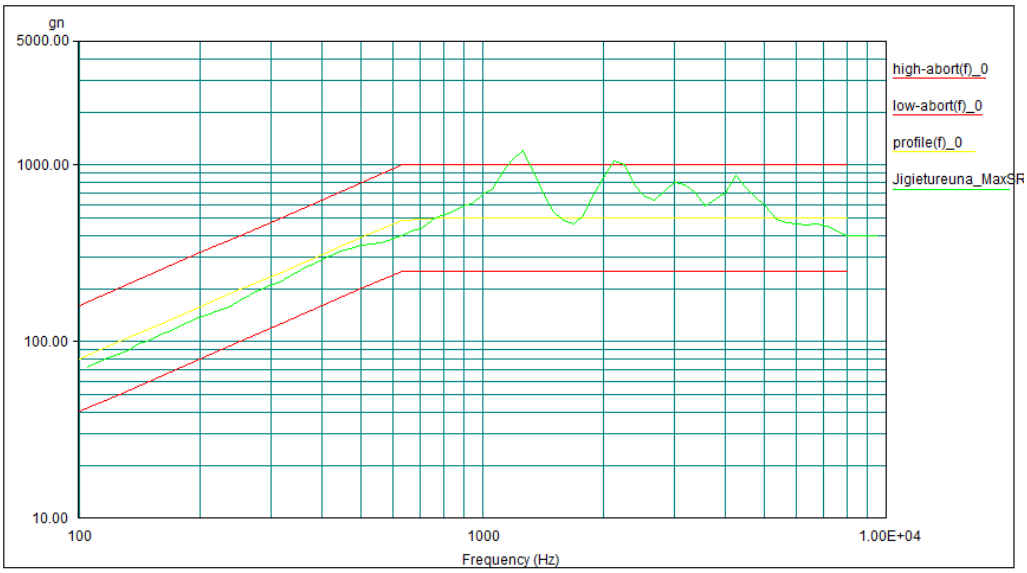

Figure 28: Measured shock spectrum for X- and Y-axis shocks. Courtesy of VTT Expert Services.

Table 6: PFPI functional test results during shock test. X, Y and Z columns denote the gap values in nanometers measured after each direction. Also the average and the standard deviation is added for each set point.

Set point	X (nm)	Y (nm)	Z (nm)	Average (nm)	SD (nm)
0.6	686	685	685	685.3	0.6
0.7	1091	1092	1091	1091.3	0.6
0.8	1496	1499	1498	1497.7	1.5
0.9	1906	1908	1907.5	1907.2	1.0
1.0	2317	2319	2318	2318.0	1.0
1.1	2715	2731	2730	2725.3	9.0

5.3 Sources of error in the vibration and shock tests

As the air gap measurements have been usually very stable, there is a small concern about the measurement accuracy during the vibration and shock testing. One clear explanation for the decreased accuracy is the different measurement method, as the reflection spectrum was correlated against the simulation data in order to find the correct air gap. The simulation for reflection spectrum is not as accurate as for transmission spectrum, and there are more stray reflections included in the measurement as well. Another issue is that the measurement fiber was held by hand, instead of using a fixed mount, as had been used earlier. This definitely adds an uncertainty to the position of the measurement point, and as the air gap is not perfectly parallel, the physical air gap may be different in different measurement points. All in all, generally the deviation in measurements was small.

The main question concerning the measured data is the large offset between vibration and shock testing. The air gap was not measured at the shock testing site before the first shocks were given, as it was assumed that the environment (and thus the air gap) had not changed. In hindsight this was a very false assumption, as the temperature, humidity and lighting conditions were different, so the initial air gap should have been measured. Now it is impossible to say whether or not the offset in air gap was caused by the first X-direction shock. However, this test will be repeated for complete AaSI, so the effect of the first shock can still be measured.

6 Thermal Characterization

6.1 Simulated thermal effects on the Fabry–Perot structure

The FPI electrodes for the capacitive measurement are placed just outside the FPI optical aperture. These electrodes go around the mirror substrate, thus enclosing the mirror inside an aluminum ring (Figure 29). This affects the thermal behaviour of the mirrors. The electrodes are made by depositing a 300 nm layer of aluminum on the 4.5 mm fused silica (SiO_2) glass substrate. Aluminum and fused silica have very different thermal expansion coefficients (23.1×10^{-6} K^{-1} and 0.55×10^{-6} K^{-1} respectively [34]), which means that tension will form as the temperature changes.

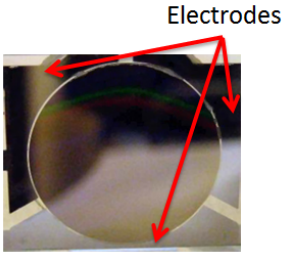

Figure 29: FPI mirror and electrodes.

A FEM simulation in COMSOL™ was made in order to gain better understanding of the effect. In the simulation a fused silica glass substrate (thickness 4.5 mm) was coated with an aluminum layer (thickness 500 nm) and a 15.5 mm hole was made in the aluminum coating. The temperature shift in the simulation was 50 °C. The simulation shows that the glass substrate displacement caused by the thermal expansion of the electrodes should be around 5 nm per 50 °C (see Figure 30). The displacement should be 5 nm because the difference between mirror center and the electrode center is ca. 5 nm, i.e. if both temperatures have the same air gap at the electrodes, the hot case should have 5 nm larger air gap at the center.This is a small effect, but as the simulation was very much simplified, the real PFPI module may also have other sources of thermal distortion.

6.2 Thermal cycling test

The thermal cycling test is used to examine the behaviour of the instrument at the thermal environment expected for AaSI. As the temperature environment on board the Aalto-1 spacecraft is constantly changing, it is necessary to understand how the changing temperatures affect the FPI behaviour.

In the first test a single PFPI-module was placed in the temperature chamber (Figure 31) and the temperature was cycled from +5°C to +55°C with a 20 minute pause after every 10°C. The chamber was also flushed with nitrogen in order to minimize the effects caused by humidity changes. The temperature sensors (thermocouples) were placed on the FPI and the control electronics, and a humidity sensor

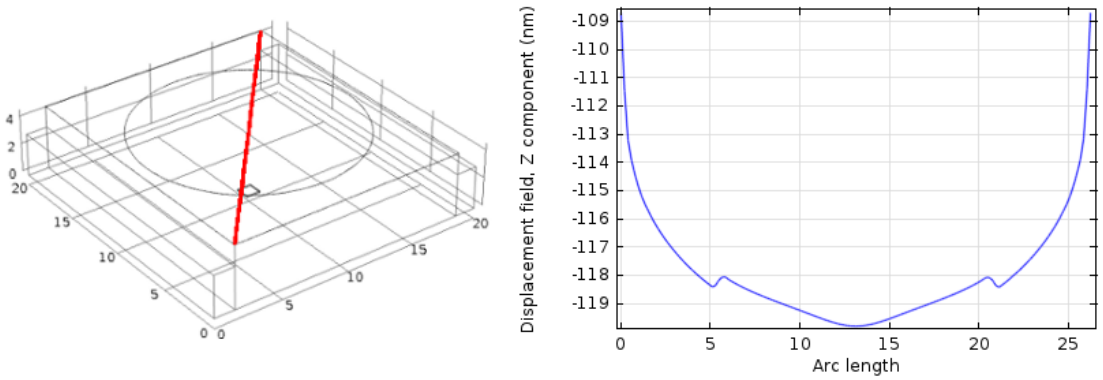

Figure 30: On the left the mirror structure is shown. On the right is the displacement of the mirror in nanometers along the red line. The arc lenght is given in millimeters. The actual mirror is located between 5 and 21 mm in this graph.

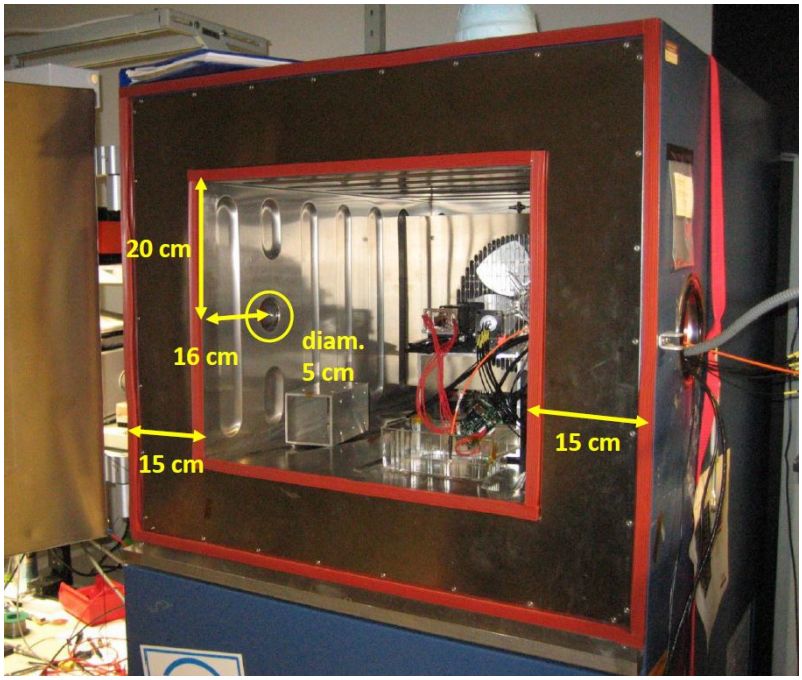

Figure 31: The WEISS 120/70 thermal chamber used for thermal characterizaton. The FPI module is placed in the middle and the measurement fibers (black and orange) and the illumination fiber (grey) can be seen on the right.

with a calibrated temperature sensor was placed in the bottom of the chamber. The temperatures, voltages and the humidity were logged every one minute.

The FPI deformation was monitored by measuring the air gap from seven different points: six measurement points were placed along perimeter with a 6 mm radius, and the seventh point was placed in the center (Figure 32). The diameter of the measurement fibers was 600 microns, and they were placed very close to the FPI mirror, thus the measurement area for each measurement point was equal to the fiber diameter. The measurement was performed by using a fiber-optic

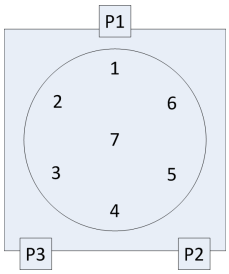

Figure 32: Gap measurement positions.

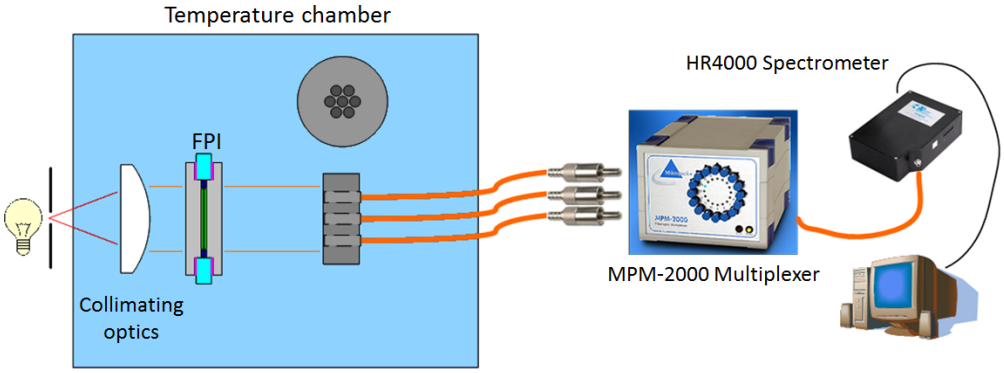

Figure 33: The temperature test setup.

multiplexer (Ocean Optics MPM2000) connected to a high resolution spectrometer (Ocean Optics HR4000). The measured spectra was then correlated against simulated transmission spectra of the FPI structure at each measurement point, so the air gap could be determined at the seven points. The measurement setup is shown in Figure 33.

6.3 FPI deformation measurement with a Helium-Neon laser

The second test was done using a Helium-Neon (HeNe) laser as a light source. The FPI was again placed in the temperature chamber and it was illuminated with a collimated beam from a HeNe laser (Figure 34). The whole FPI aperture was imaged with a self-built camera system. The set point was adjusted in small steps so that the transmission peak could be imaged. A temperature sensor placed on the FPI was used for temperature measurements during this test. Similar measurement setups have been used for FPI characterization before, but standardized tests for FPI's have not been developed [35, 36].

The set points were chosen in a way that the passband of FPI was scanned over the laser wavelength (632.8 nm, Figures 35 and 36). The FPI aperture was then imaged with a camera for every set point, and the light intensity at every point of the aperture (i.e. every pixel) was recorded. For each pixel the set point values with the strongest signal (i.e. transmission maximum) were then selected from the measurement data. The change in the set point value relates to a change in the physical air gap, so even if the actual gap value is not known, relative air gap values

across the aperture can be calculated. However, in this case the physical air gap was measured optically for different set point values before the test. The set point-to-gap relation of PFPI-006-V033 is shown in Figure 37. It also has to be taken into account that the gap shape from the direct set point values is actually the mirror image of the air gap, as the initially smaller gaps will be tuned to the laser wavelength at larger set points. The correct gap values can be calculated with the simple formula

$$d = d_0 + (d_0 - d_{sp}), \tag{27}$$

where d_0 is the gap value corresponding to the initial set point and d_{sp} is the gap value from the measurement.

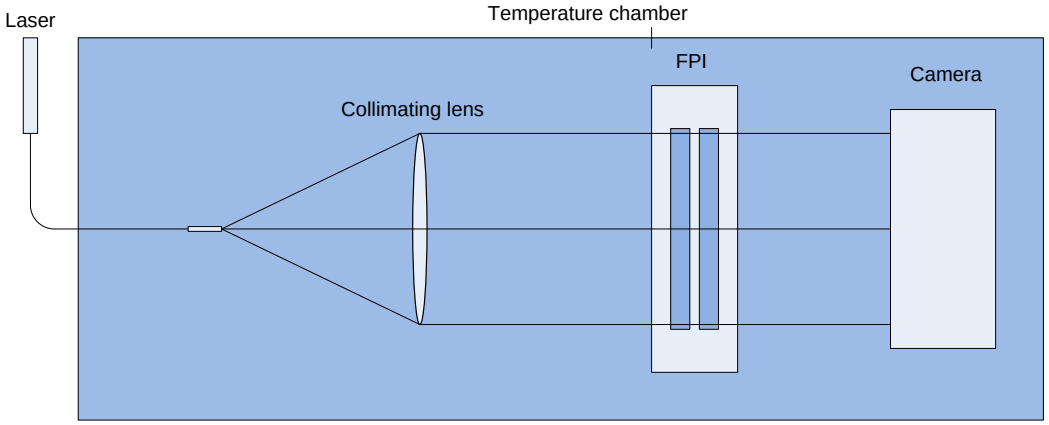

Figure 34: The measurement setup used for measuring the gap shape. The FPI module was illuminated with a HeNe laser (wavelength 632.8 nm) and the FPI aperture was imaged with a camera while the air gap was scanned over the laser wavelength.

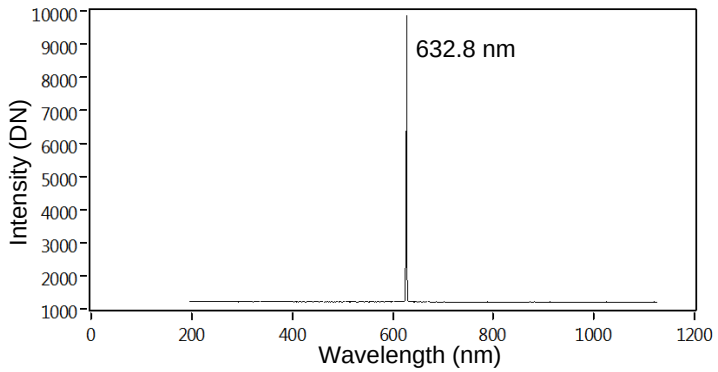

Figure 35: Laser spectrum measured with HR4000 spectrometer, showing a single narrow peak at around 633 nm.

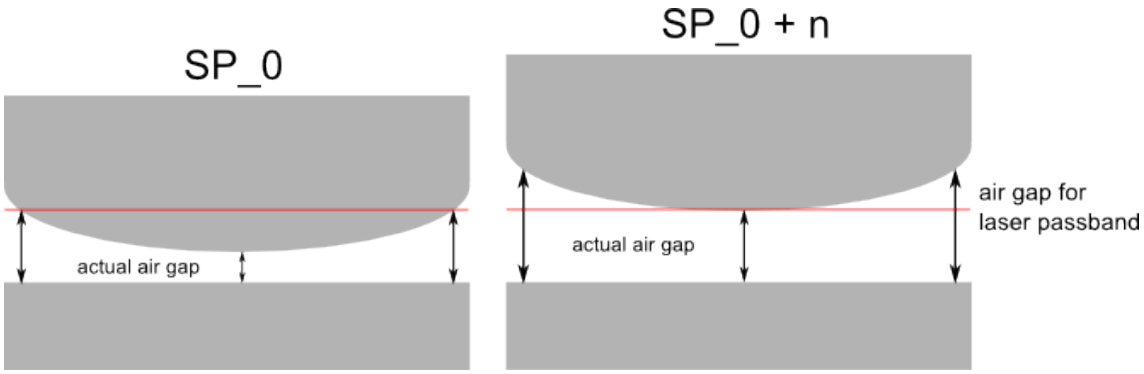

Figure 36: Set point adjustment over the laser wavelength passband.

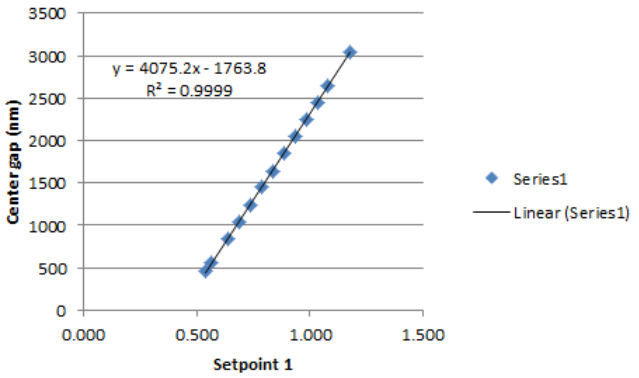

Figure 37: Set point to gap relationship for PFPI-006-V033.

6.4 Degradation of the spectral performance

Directly related to the FPI deformation is the degradation of the spectral performance. As the mirrors are not exactly parallel, different wavelengths pass the FPI at different points, which broadens the transmission peak. This effect was measured with the setup shown in Figure 38, which was placed in the same temperature chamber used earlier. The temperature was cycled between +5°C and +55°C during the test, with a 30 minute pause every 10 degrees. The temperature was measured from the temperature sensor placed on the FPI PCB.

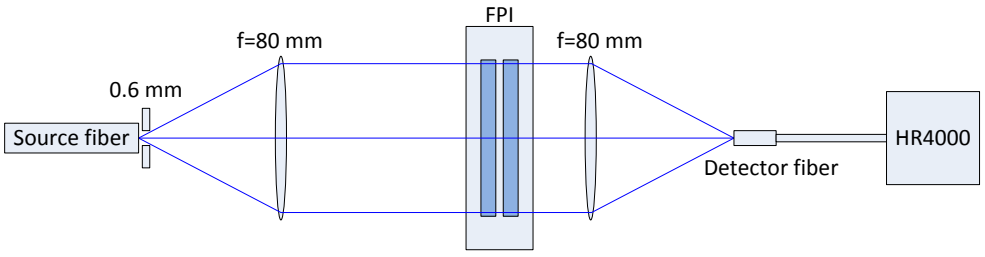

Figure 38: The setup used for measuring the spectral performance. The collimation accuracy was ca. 5°.

6.5 Results

6.5.1 Air gap drift

During the first thermal cycling test, a clear drift of the FPI air gap was detected (Figure 39). The air gap drift was measured to be ca. 1.5 nm/°C for the center gap. This is well outside the design specification of 0.316 nm/°C. The drift measured was not linear, the amount of drift was reduced above 25°C for all measurement points, and for the measurement point 4 the drift disappeared completely after 30°C.

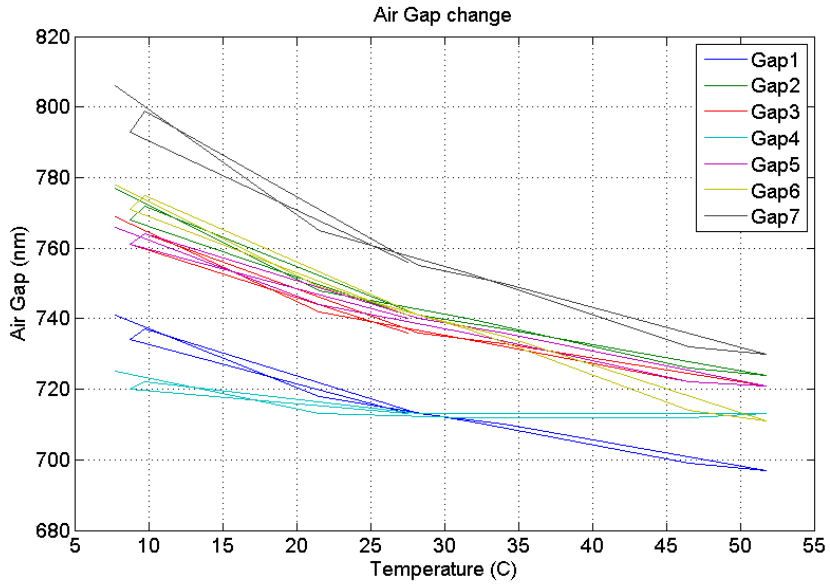

Figure 39: FPI air gap drift of PFPI-006-V035.

As the air gap drifts, the center wavelength of the passband(s) will also drift with the temperature, so the gap calibration performed in room temperature is no longer valid at higher or lower temperatures. In order to compensate this, a simple temperature calibration was added. The compensation was performed in a way that the air gap at the center was kept constant, and the set point values (SP1, SP2, and SP3) needed to achieve the best possible gap with this center gap were then recorded at different temperatures. The resulting curves are shown in Figure 40. It was assumed that the set point relationships from the initial gap calibration do not change with temperature, as was measured earlier (Chapter 4.5). Now the test was repeated with the temperature compensation enabled, and it can be seen that the center gap drift was reduced to ca. 0.1 nm/°C, but the mirror deformation is still present as the temperature cools down, resulting in the degradation of spectral resolution. This deformation was tracked to be the main cause of the temperature drift. Changing humidity was also suspected, but as the temperature chamber was flushed with nitrogen, the humidity remained constant during the test. The temperature drift of the electrical components was also investigated, but it was found out to be much smaller than the drift measured (see Appendix 9).

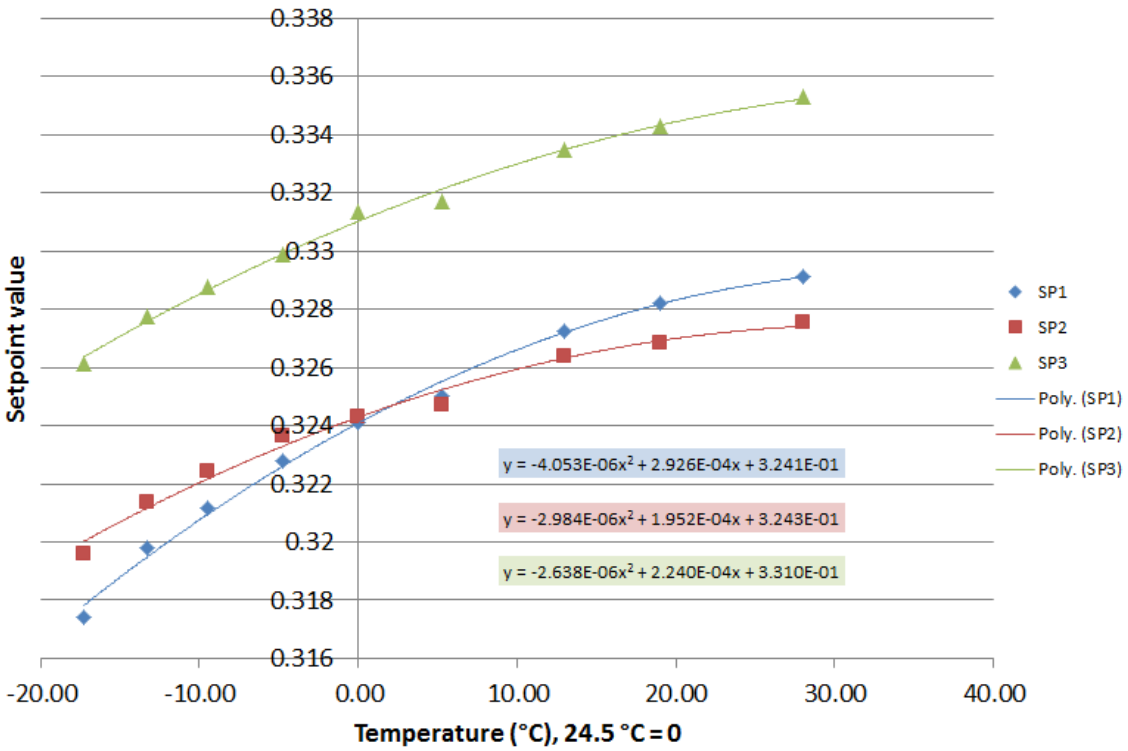

Figure 40: Temperature compensation for set points 1, 2 and 3 (PFPI-006-V035).

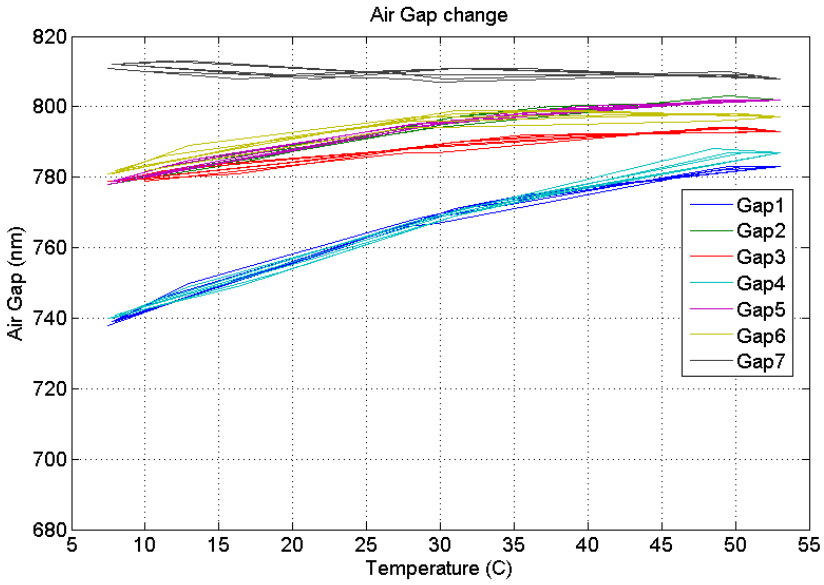

Figure 41: FPI air gap drift of PFPI-006-V035 with temperature compensation.

6.5.2 Mirror deformation

To study the deformation more closely, the gap shape of PFPI-006-V033 was measured more accurately with the laser setup. From this measurement the shape of the FPI air gap can be seen as a nearly symmetric bulge, where the gap is largest in the middle. In Figure 42 the effect of temperature is clear: in lower temperatures the FPI bulges more than in higher temperatures, the P-V ranging from ca. 100 nm (cold case) to ca. 50 nm (hot case).

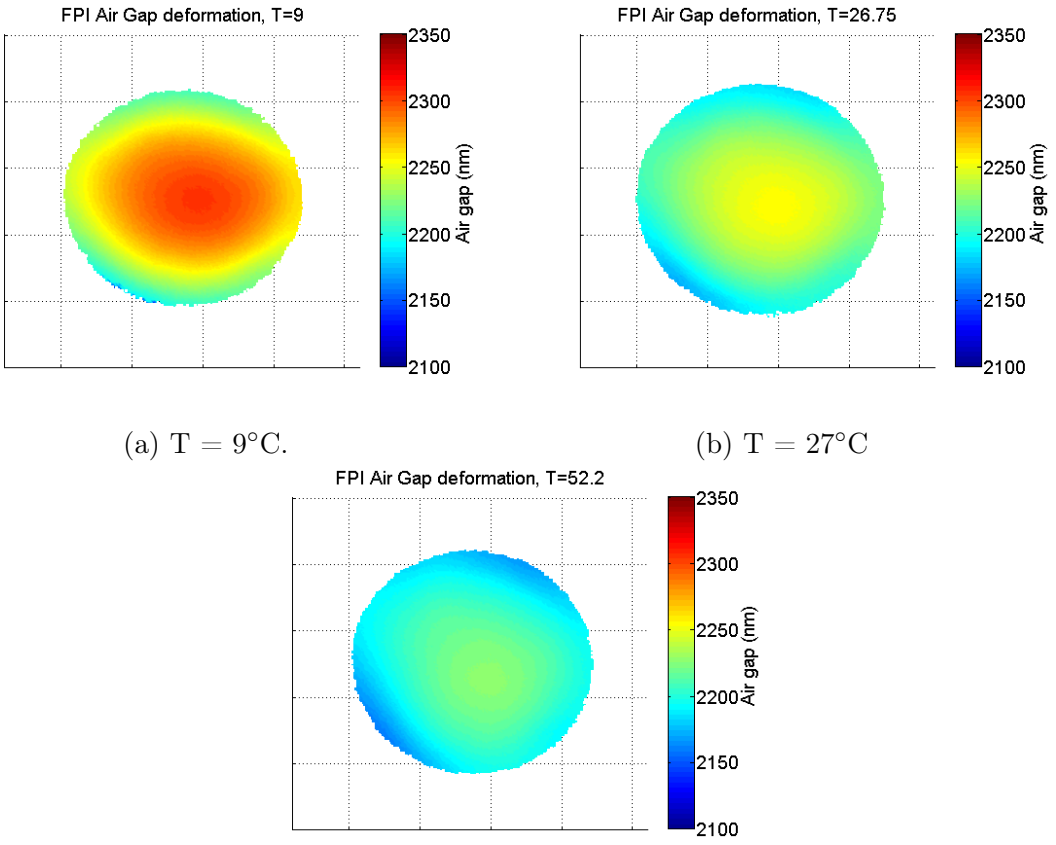

(a) T = 9°C.

(b) T = 27°C

(c) T = 52°C

Figure 42: PFPI-006-V033 deformation in different temperatures. A strong bulging effect can be seen at lower temperatures, i.e. the air gap is larger in the center than around the edges of the aperture. The colorbar to the right tells air gap value in nanometers (from 2100 to 2350 nm).

As the deformation is very evident, it is necessary to understand the underlying cause. In order to do this, a special PFPI module (PFPI-006-V036) was constructed (Figure 43). The mirrors of this module were made on different fused silica substrates (manufactured by LightMachinery Inc.), which explains the difference in the general shape, i.e. why PFPI-006-V033 has a parabolic shape and the PFPI-006-V036 has a saddle shape. The LightMachinery substrates were also of better quality [18], thus the air gap P-V is generally smaller.

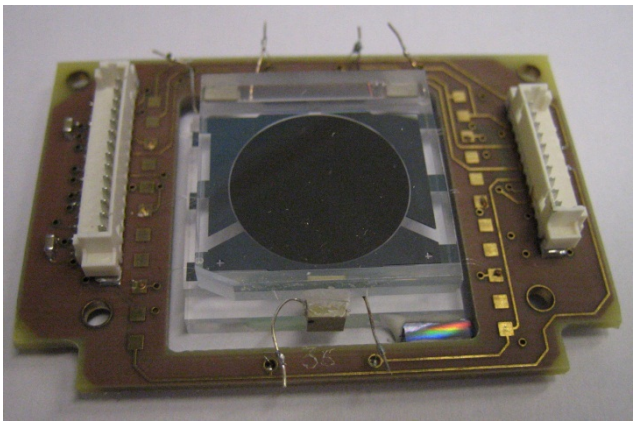

Figure 43: The special PFPI module (PFPI-006-V036) constructed for deformation study. The thick piezo wires have been connected to the PCB by very thin bonding wires and the FPI module has been attached from one corner only. This image has been taken after the excess glue was removed.

In this module the thick piezo wires were separated from the PCB in order to remove any possible stresses caused by the thick wires. The module was also attached only from one corner to the PCB, so any deformation of the PCB would not stress the FPI module. The main suspect for the deformation was the glue which is used to attach the piezo actuators to the mirrors, so after the initial measurements, the excess glue was removed with a knife (Figure 44).

(a) Before glue removal.

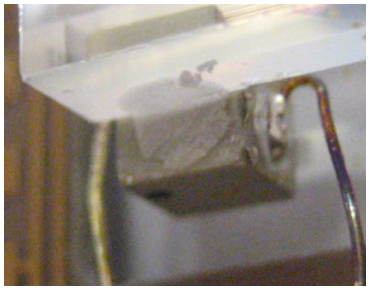

(b) After excess glue was removed.

Figure 44: Removal of excess glue from the piezo actuators.

The effect of glue removal was clear, as shown in Figure 45. In this figure the gap shape is shown from two different perspectives, first looking directly at the FPI aperture and then looking slightly from the side to illustrate the shape of the air gap. A saddle shape is easily distinguished, especially from Figure 45-c. Also a mirror defect is seen near the centre of the mirror, showing that a part of one of the mirrors is thicker than its surroundings resulting in a smaller air gap. This defect does not affect the shape measurement study. In room temperature the P-V of the air gap was reduced from ca. 27 nm to ca. 18 nm. This measurement was then repeated at ca. +10°C and ca. +55°C. In +10°C the effect of removing the glue was even clearer: the P-V of the air gap was reduced from ca. 49 nm to ca.

22 nm. However, at higher temperatures, the effect was not present, as shown in Figure 46. It may be too small to distinguish with this kind of a measurement setup, but it may also be that at higher temperatures most stresses causing the distortion have already disappeared. The shape of the air gap at ca. 55°C supports this assumption, as the air gap is already very flat (i.e. mirrors are parallel), although tilted. In order to better understand the effect, the measurement should be repeated at even higher temperatures, e.g. +75°C or +100°C. Unfortunately the setup used for the measurement is not suited for very high temperatures, so at this time the experiment cannot be performed. However, even from these measurements it is very clear that the piezo glue affects the amount of deformation caused by temperature changes.

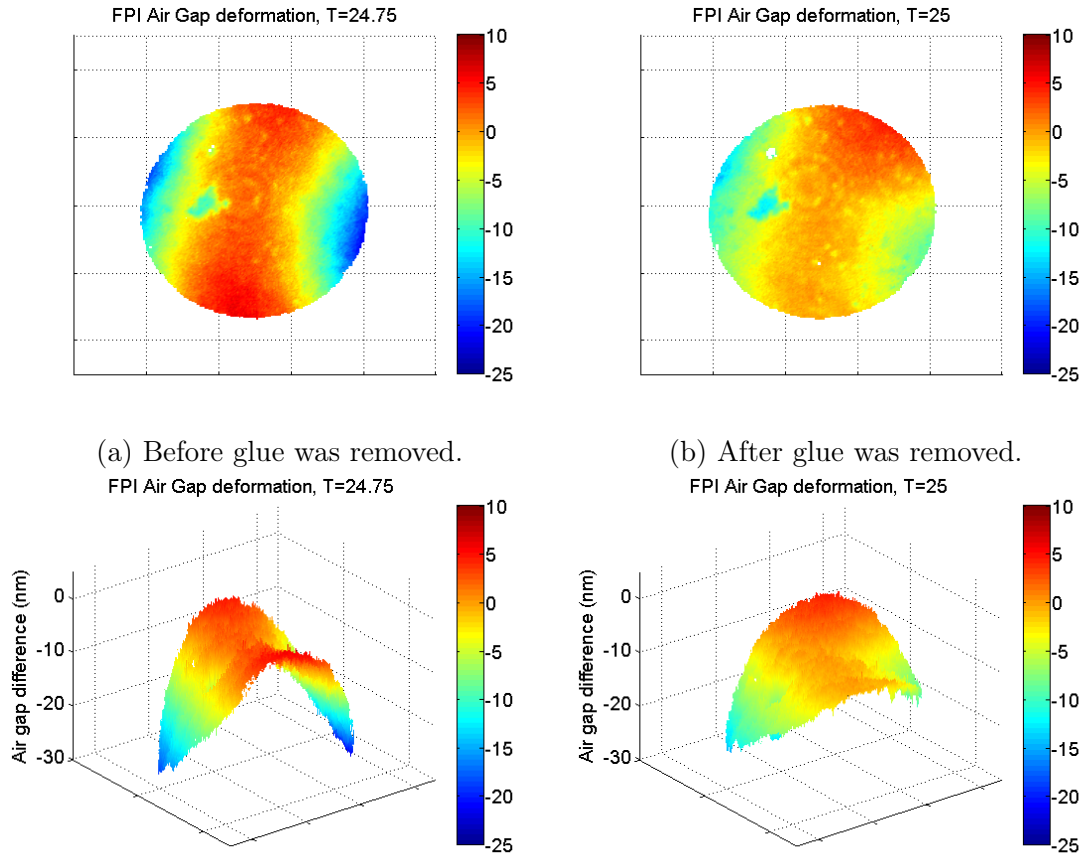

(a) Before glue was removed.

(b) After glue was removed.

(c) Before glue was removed.

(d) After glue was removed.

Figure 45: Effect of glue removal to the air gap shape over the FPI aperture shown from two different perspectives. Measurements performed at 24.75°C and 25.0°C.

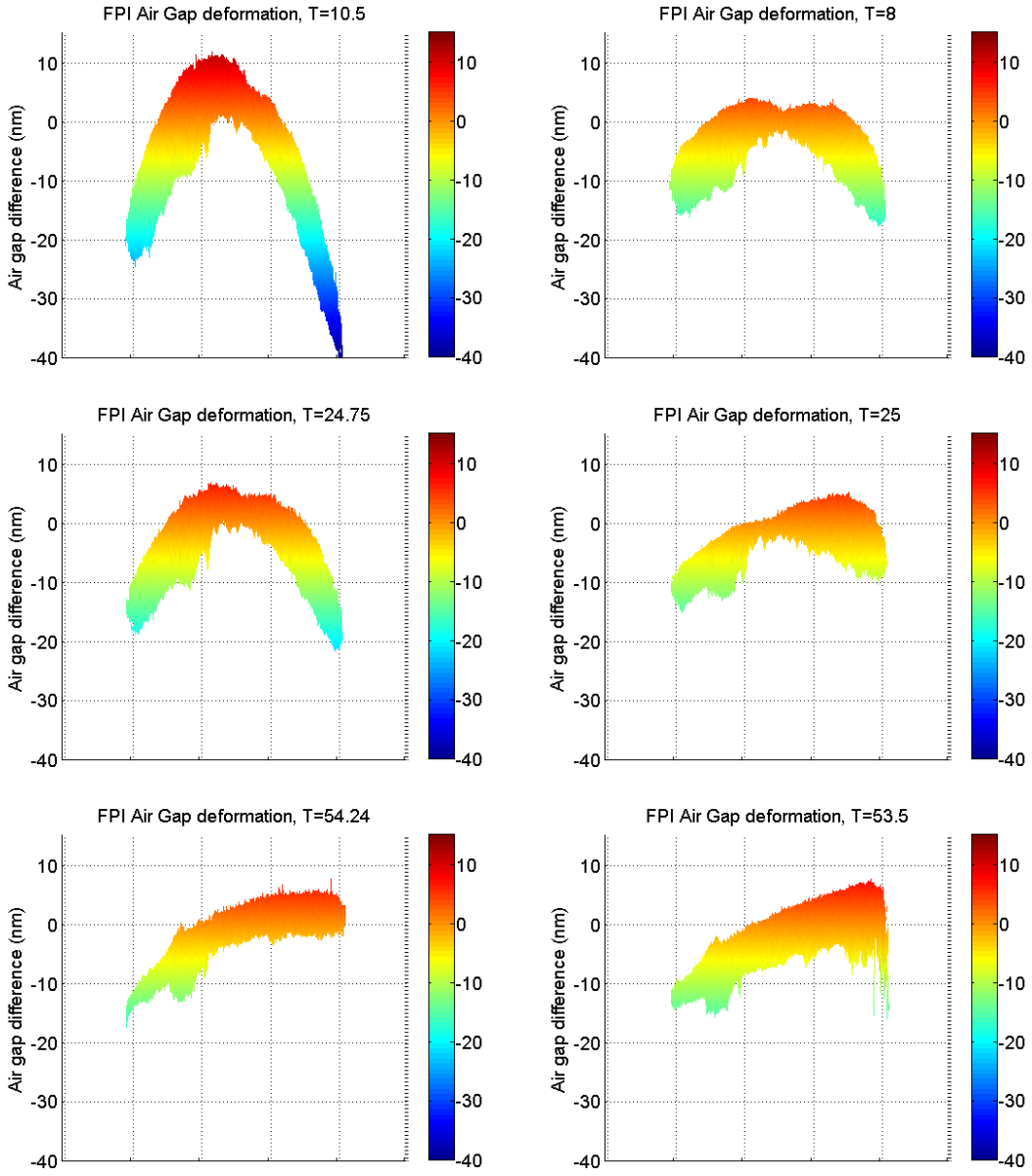

Figure 46: The air gap shape shown from the side. Left and right side figures show the cases before and after glue removal. Measurements performed at ca. 10°C, 25°C and 55°C. Clear change in curvature can be seen at lower temperatures. However, at ca. 55°C there is no clear difference.

6.5.3 Performance degradation

This measurement was performed on PFPI-006-V035, which has the same general shape as PFPI-006-V033. As Figure 42 shows, the FPI air gap of is distorted in low temperatures. This distortion also changes the shape of the transmission peak: in colder temperatures the peak broadens towards shorter wavelengths. This happens because the center of the air gap is bulging, so the physical gap at the edges of the aperture is smaller than in the center, thus shorter wavelengths can pass the FPI near the mirror edges (Figure 47a). This broadening naturally affects the FWHM as well: an increase of ca. 5 nm can be seen when moving from +55°C to +5°C (Figure 47b). However, the temperature effect to the FWHM is less than 6 nm over 50°C. It can also be seen that within the operational temperature of AaSI (15–45°C), the FWHM stays within the specifications (specification for the FWHM is 10–30 nm [30]). Closer inspection of the peak position reveals that the position is not very stable, even when compensated (Figure 48). There is a strong hysteresis-like effect, which causes the air gap to vary ca. 3 nm even at the same temperature. The cause for this variation is investigated in Chapter 8.2.2. For the operational temperature range (15–45°C), the CWL drift is small, only ca. 0.19 nm/°C for 2nd order transmission peak, which is within the specification (0.2 nm/°C).

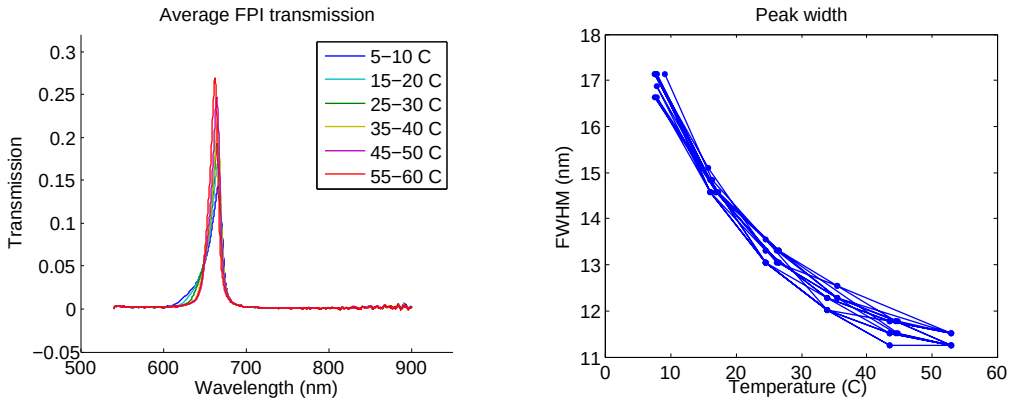

(a) Spectral transmission at different temperatures (2nd order peak).

(b) Peak width change as a function of temperature.

Figure 47: Temperature effects on the spectral transmission. Air gap = ca. 817 nm.

The test was afterwards repeated with three different set point values (0.2836, 0.3242 and 0.3724) to find out how the air gap size affects the temperature distortion. These three set point values correspond to air gaps of ca. 500, 800 and 1200 nm. At these air gaps, the transmission peaks within the operational wavelength range (500–900 nm) of AaSI are located between 600 and 700 nm. The corresponding orders for these peaks are 1, 2 and 3 respectively. The peak width changes are shown in Figure 49, which shows that the peak broadening is more prominent at low order and small air gap than at higher orders and larger air gap, but even with the air gap of 500 nm the FWHM stays within the specification at the operational temperature range. The measured peak widths also match the simulated peak widths well (Figure 21).

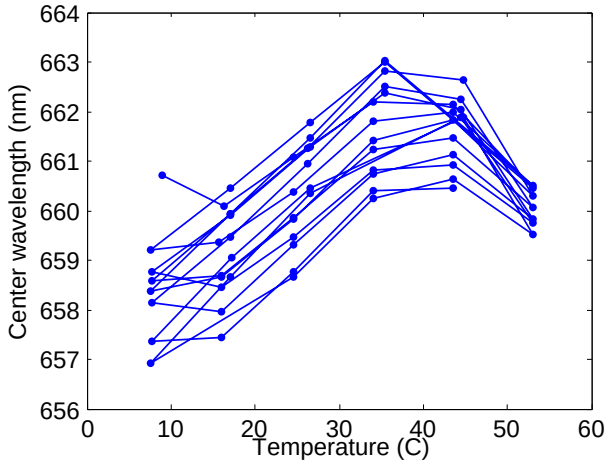

Figure 48: Center wavelength of the peak shown in Figure 47a as a function of temperature. The total drift is ca. 0.19 nm between 15 and 45°C. A clear hysteresis-like effect can be seen.

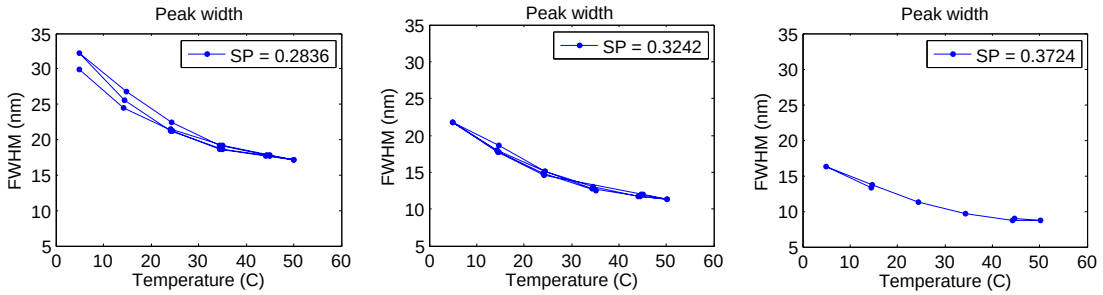

(a) 1st order peak. (b) 2nd order peak. (c) 3rd order peak.

Figure 49: Peak width change for three different air gaps as a function of temperature. Air gap values ca. 500 nm (a), ca. 800 nm (b) and ca. 1200 nm (c). At smaller air gaps the transmission peaks are wider than at larger air gaps. The peak broadening is also stronger at smaller air gaps, but the FWHM still stays within specifications.

7 Vacuum Testing

During the building of the vacuum setup it was found that the closed-loop control optimized for normal air pressure does not function in lower pressures. In order to characterize the behaviour of the FPI in lower pressures and vacuum, the frequency and step responses of the FPI were measured in different pressure environments. The results of these tests will be used to tune the control loop for vacuum operations. A simple vacuum chamber (Figure 50) was used for the tests. The pressure range for the chamber was from 10^{-3} to 10^{3} mbar. A PFPI module with no control loop (i.e. the piezo actuators were controlled directly) was used in the frequency response and open-loop step response measurements.

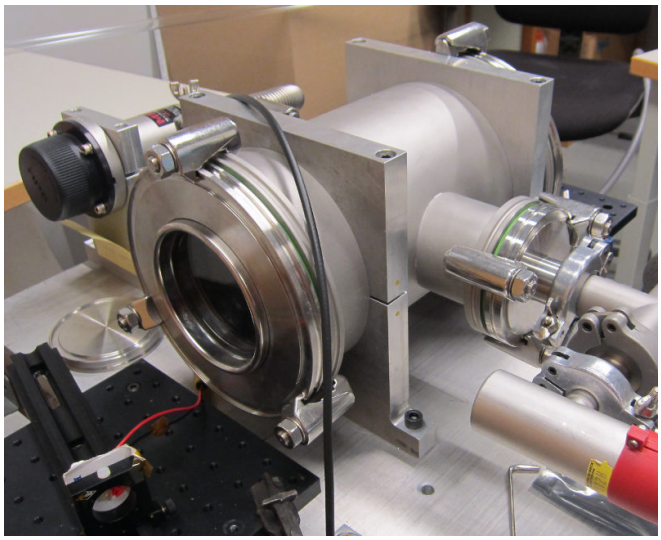

Figure 50: The vacuum chamber used for frequency and step response measurements.

7.1 Frequency response measurement

The FPI was first set to a fixed air gaps at 800 and 3000 nm, and the air gap value was confirmed with an optical measurement. The frequency response was measured by oscillating the FPI with a signal from Hewlett-Packard 3324A signal generator and measuring the resulting signal caused by capacitance change in the moving electrodes. The excitation signal frequency was scanned from 5 kHz to 39 kHz and the signal amplitude was kept constant if possible. In some cases the resonance amplitude was so large that the excitation amplitude had to be reduced. The amplifier output signal, the input voltage and the input current were measured with a National Instruments analog input DAQ. This measurement was then repeated at different pressure levels from 10^{-3} mbar to 10^{3} mbar with two different air gaps, ca. 800 and 3000 nm. The operation principle of the measurement circuit is explained below.

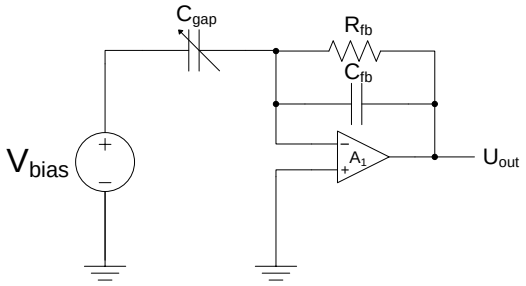

Figure 51: The circuit used for measuring the frequency response. V_{bias} = 50V, R_{fb} = 10 MΩ, C_{fb} = 10 pF.

In order to measure the change in electrode capacitance, a custom amplifier circuit had to be built for the measurement, which is shown in Figure 51. By definition the operational amplifier holds both terminals at the same potential, thus the voltage over C_{gap} is always equal to V_{bias}. The current through a capacitor is defined as $I(t) = \frac{d}{dt}CV$, thus

$$I_{C_{gap}}(t) = V_{bias}\frac{d}{dt}C(t). \tag{28}$$

The amplifier and the feedback resistor (R_{fb}) both have very large impedances compared to C_{fb} (when $f >> (2\pi R_{fb}C_{fb})^{-1}$), thus $I_{C_{gap}}$ always goes through C_{fb}, causing an opposite voltage change at the amplifier output, thus

$$\begin{aligned}
\Delta U_{out} &= -\frac{1}{C_{fb}}\int I_{C_{gap}}dt \\
\Delta U_{out} &= -\frac{V_{bias}}{C_{fb}}\int_{C_0}^{C_1} dC \\
\Delta U_{out} &= -\frac{V_{bias}}{C_{fb}}(\Delta C).
\end{aligned} \tag{29}$$

The capacitance of a plate capacitor is defined as $C = \epsilon_n A/d$, where ϵ_n is the permittivity of the dielectric medium separating the plates (in this case the medium is either air or vacuum, so ϵ_n equals vacuum permittivity[2] ϵ_0), A is the area of the plate and d is the separation distance so ΔC can be found by differentiating C with respect to d:

$$\begin{aligned}
\frac{dC}{dd} &= \frac{\epsilon_0 A}{d^2} \\
dC &= \frac{\epsilon_0 A}{d^2}dd \\
\Delta C &= \frac{\epsilon_0 A \Delta d}{d_0^2},
\end{aligned} \tag{30}$$

[2] $\epsilon_0 = 8.854 \times 10^{-12}$ F/m

where d_0 is the initial separation distance and Δd is the electrode displacement. Now by inserting (8) into (7), the electrode displacement as a function of U_{out} can be found:

$$\Delta d = \frac{|\Delta U_{out}| C_{fb} d_0^2}{V_{bias} \epsilon_0 A_{electrode}}. \tag{31}$$

7.2 Step response measurement

The step response was measured with a similar setup as the frequency response. The FPI air gap was fixed at around 1000 nm, and the piezo-actuators were excited with a signal generator (HP3324A). In this test the frequency used was 100 Hz with an amplitude of 4–20 V. The FPI was illuminated with a white LED and the LED current was pulsed with 5 μs long pulses. The LED signal was triggered by the signal generator used to move the FPI and it was possible to tune the triggering delay (Figure 52). 50 of these pulses were integrated with an Ocean Optics HR4000 spectrometer, thus a transmission spectrum exactly at the given delay was measured. The physical air gap was then calculated from the transmission spectrum, so the mirror movement during the transition could be recorded. By tuning the triggering delay from 0 to 5000 μs with 5 μs time step, the movement of the FPI mirror after a 4–20 V step could be measured at 1 nm accuracy with 5 μs time resolution. The step response directly from the electrodes was also measured during one measurement. This measurement was performed at two different pressures (ca. 10^{-2} and 10^3 mbar) in order to study the damping effects and potential air spring effects within the FPI structure.

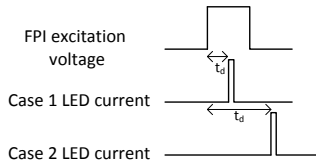

Figure 52: The exposure method used in the step response measurement. Led pulse length not to scale.

7.3 Results

7.3.1 Frequency response

Results of the frequency response test are shown in Figures 53 and 54. The figures show that the resonance frequency moves to the lower frequencies as the ambient pressure drops. The air gap length also influences the resonance frequency at higher ambient pressures, since the resonance frequency is around 22 kHz for an air gap of 800 nm but only ca. 18 kHz for an air gap of 3000 nm. However, at vacuum, the resonance frequency is ca. 14 kHz for both air gap lengths. Also a strong amplification of the resonance is also seen at lower pressures, this may be due to

an air spring effect (Figure 55) formed within the FPI air gap, but the exact cause for this is still unknown. The air spring effect may also cause the higher resonance frequency at smaller air gap lengths (Figure 56).

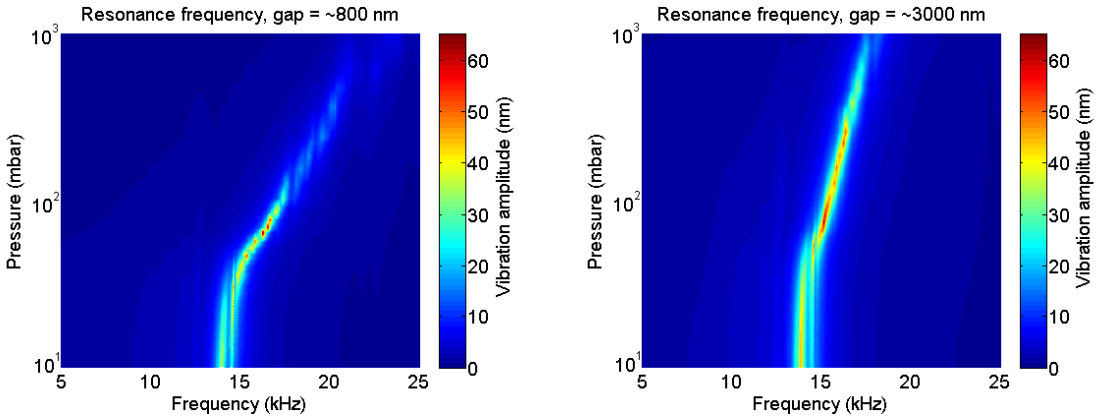

(a) Air gap = ca. 800 nm. (b) Air gap = ca. 3000 nm.

Figure 53: Frequency response, excitation amplitude normalized to 0.1 V. Colorbar to the right tells the vibration amplitude in nanometers.

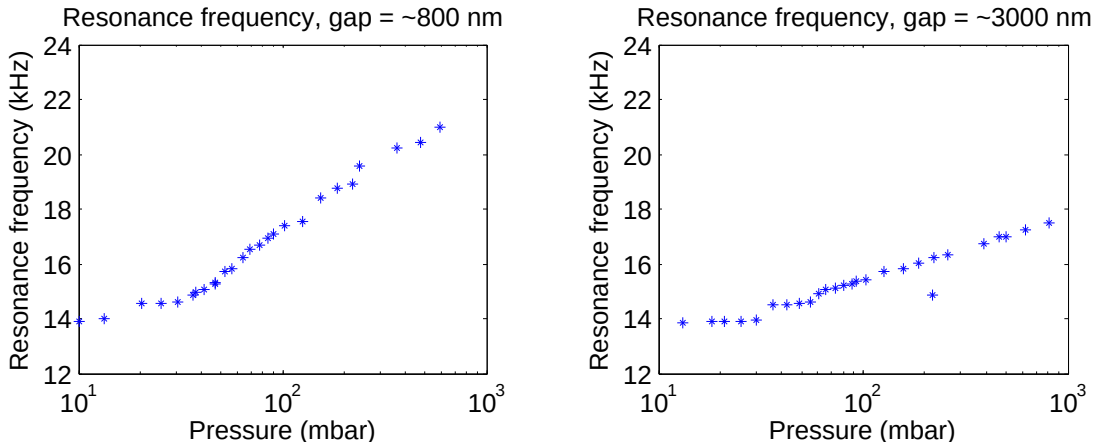

(a) Air gap = ca. 800 nm. (b) Air gap = ca. 3000 nm.

Figure 54: FPI resonance frequency.

The frequency of an air spring is defined as [37]

$$f = \frac{1}{2\pi}\sqrt{\frac{\gamma P A}{m_s d}}, \tag{32}$$

where m_s is the mass and A is the area of an object moving in a closed enclosure with a length d (Figure 55). P is the ambient pressure and γ is the heat capacity ratio of the surrounding medium (for air, $\gamma = 1.4$ [37]). The FPI is not really a closed enclosure, but as the air gap is very small, some effect may still be present.

The nominal frequency of a simple air spring formed by a two fused silica mirrors (dimensions 20 x 20 x 4.5 mm^3, Figure 55) was calculated for two different air gaps (800 and 3000 nm). The calculation shows that for simple air spring, the shift in resonance frequency is more prominent for smaller gap lengths (Figure 56).

The actual measurements (Figure 53) do not follow the calculated curves, but the resonance frequency is increasing when the pressure is increased, which is in line with the measurements. The frequency values itself do not match, but this may be due to the fact that the FPI is not a closed enclosure and it is a more complex structure than the simplified model used for the calculation. Other effects affecting the resonance frequency may also be present. The resonance frequency of the FPI sets the upper limit to the control speed, as the mirrors will start to oscillate if the air gap is tuned at the same frequency.

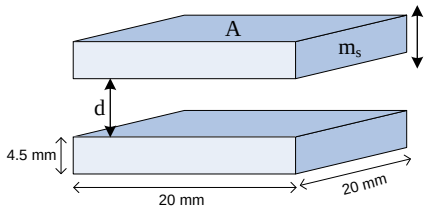

Figure 55: Vibrating mirror structure.

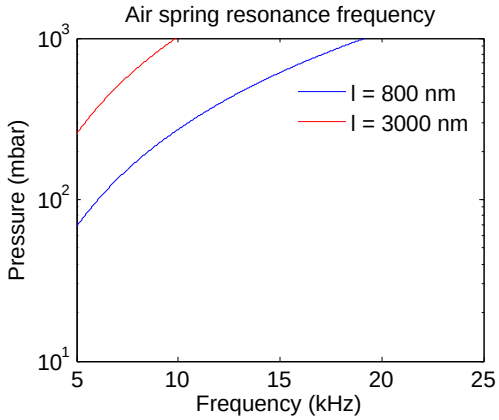

Figure 56: The air spring resonance frequency for two different air gaps.

7.3.2 Open loop step response

First the test response was measured in normal atmospheric pressure (1000 mbar). The step was performed both ways, 0 V to +20 V and from +20 V to 0 V. From the measurement it is seen that the oscillation of the mirror is attenuated quite fast by the air enclosing the FPI structure. The frequency can be calculated from the Figure 57: the figure shows that the period of oscillation is about 0.05 ms, thus the frequency is ca. 20 kHz, which is very close to the resonance frequency measured earlier.

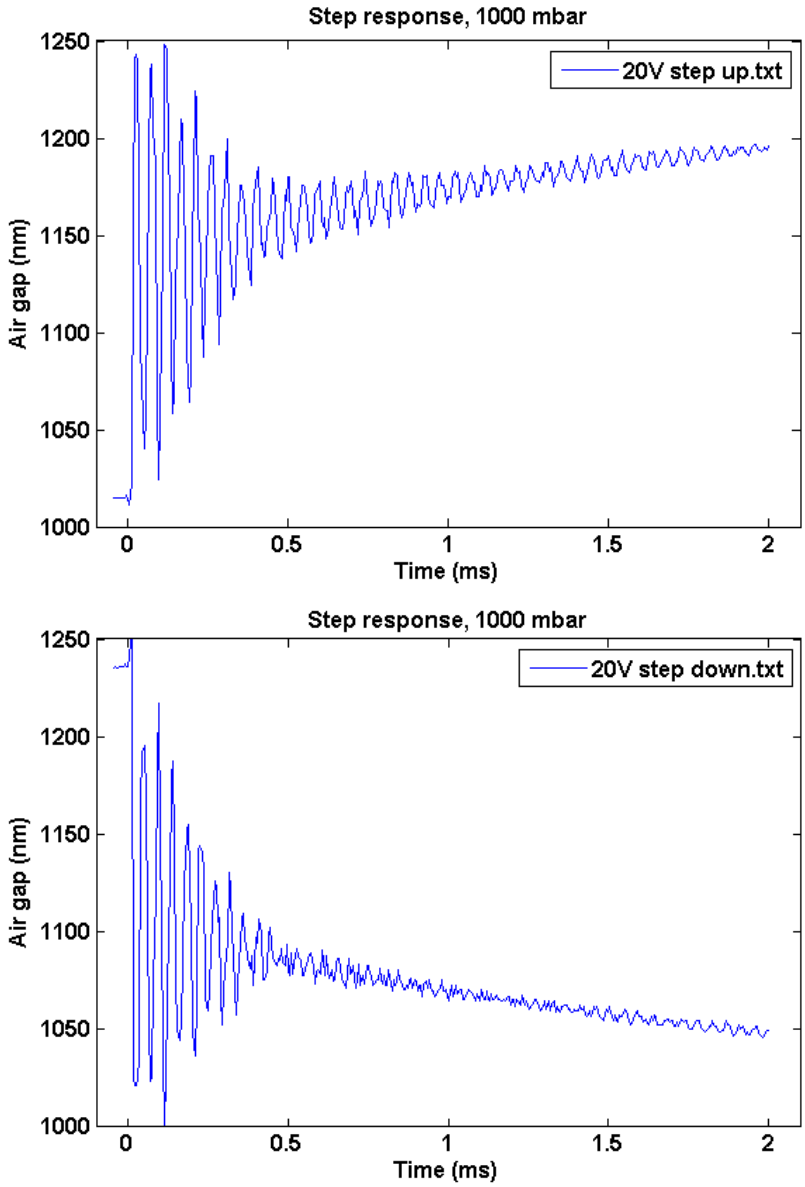

Figure 57: Step responses from +0V to +25V and from +20V to 0V, P = 1000 mbar

After the measurement had been performed in normal atmospheric pressure, the vacuum chamber was set to 10^{-2} mbar and the test was repeated with a 4 Volt step. Results are shown in Figure 58. In this case, the oscillation period is ca. 0.07 ms, which corresponds to a frequency of 14.3 kHz. This frequency matches the previously measured vacuum resonance frequency very well. It can also be seen that without the damping effect of the surrounding gas, the oscillation amplitude is decreasing much slower.

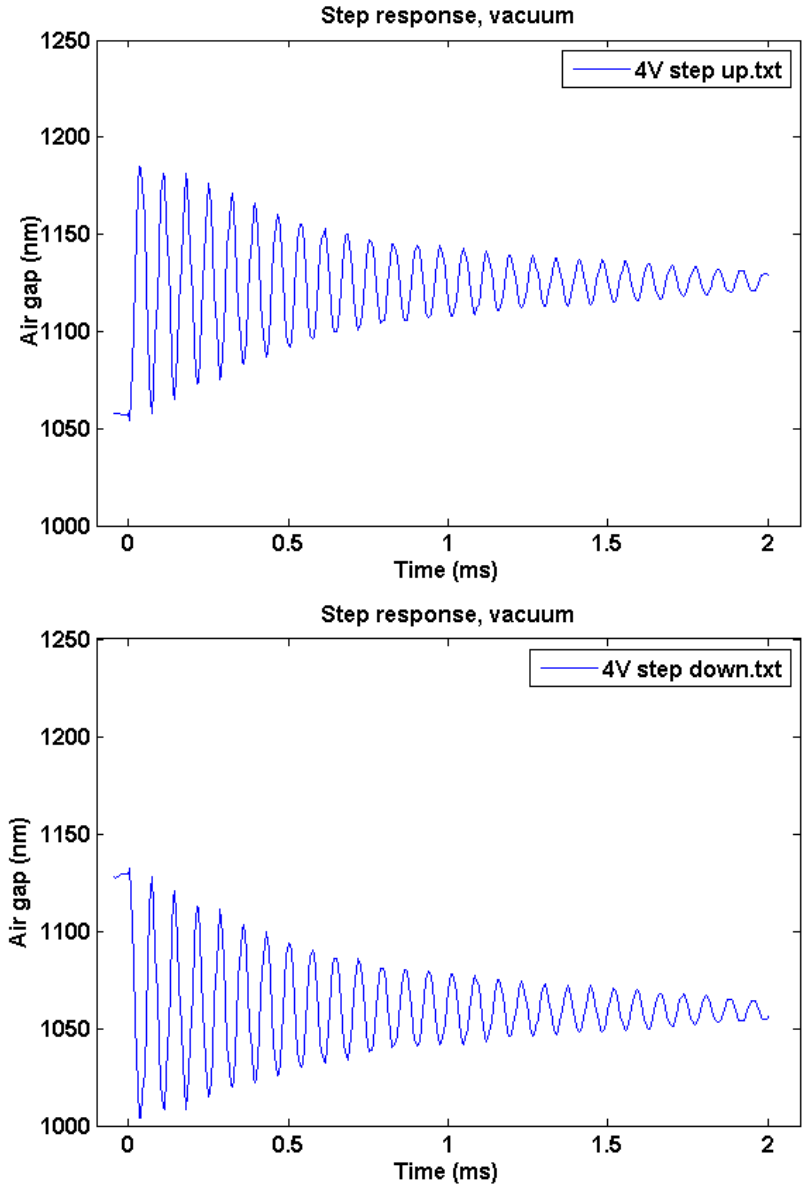

Figure 58: Step response from 0V to +4V and from +4V to 0V, P = 10^{-2} mbar.

Finally, in addition to the optical measurement from the center, the step response was measured capacitively from the electrodes using the same method which was used to measure the frequency response. This measurement was also used to confirm the results of the frequency response test. This measurement was also performed at near vacuum pressures, but as it was performed last, the pressure had already risen to ca. 10^{-1}–10^{0} mbar as the vacuum pump had been turned off. Figure 59 shows that both measurements are very well in-line with each other. According to these measurements, in vacuum it takes at least 2 to 10 milliseconds for the FPI to stabilize after a gap change, thus it is unnecessary to make the control loop faster than this.

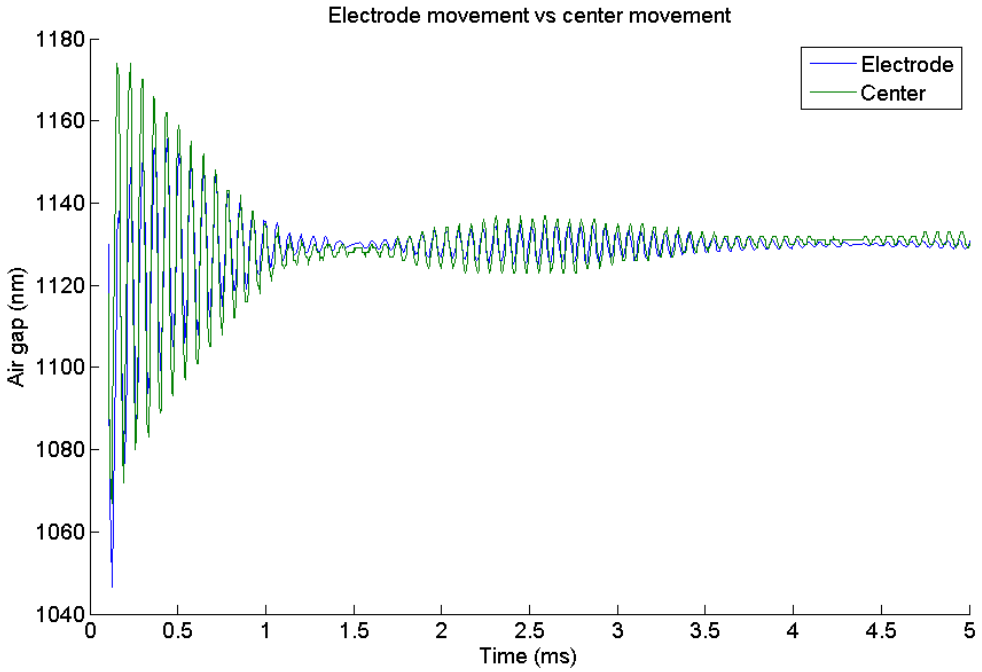

Figure 59: Step response comparison.

7.3.3 Closed loop step response

After the open loop step and frequency response measurements, the control loop of the FPI controller was modified to ensure the proper operation in vacuum environment. The modifications were needed as in normal ground level pressure the air between the mirrors acts as a damping medium (as seen in Figure 57). Removing the damping medium caused the control loop to oscillate (Figure 60), which prevented any optical air gap measurements. To solve the problem the high voltage amplifier was altered in order to lower the control loop gain at high frequencies. The modifications were suggested and done by Jussi Mäkynen at VTT. After the modifications the FPI operated without problems in closed loop control in all pressure environments. The results for closed loop step response measurements are shown in Figure 61, which shows that there is no significant FPI stability difference between vacuum and normal pressure. The main difference is that the FPI air gap stabilizes a little bit faster in vacuum. The stabilization time of the air gap is around 20 to 30 ms.

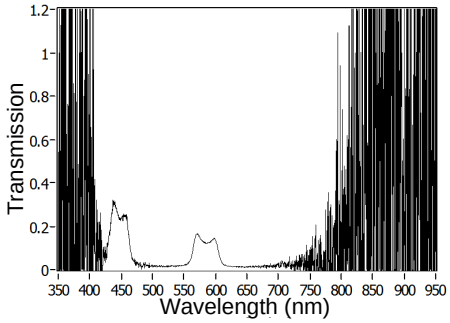

Figure 60: A transmission spectrum of an oscillating air gap. The oscillation produces twin-peak shape in the spectrum instead of the normal peak.

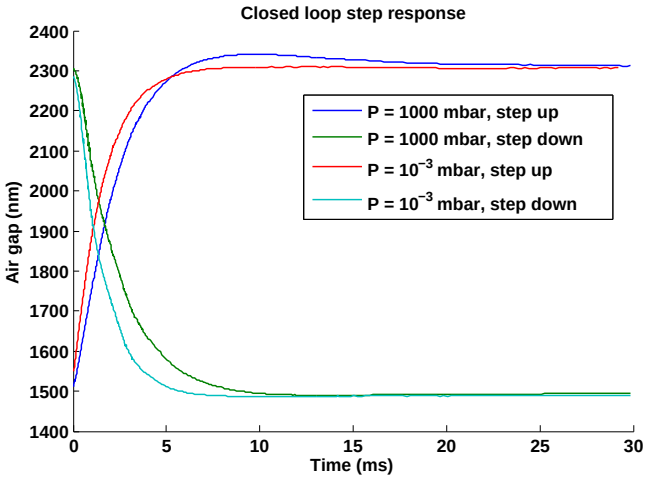

Figure 61: Closed loop step response. In vacuum the air gap is stabilized after 10–20 ms.

8 Thermal Vacuum Testing

8.1 Thermal vacuum test setup

The thermal vacuum testing is performed as described in the General Environmental Verification Standard [33]. The standard states that eight thermal-vacuum temperature cycles should be performed for any instrument components/units. This applies for the PFPI module of AaSI. The purpose of this test is to qualify the PFPI module design and the compensation methods to space environment.

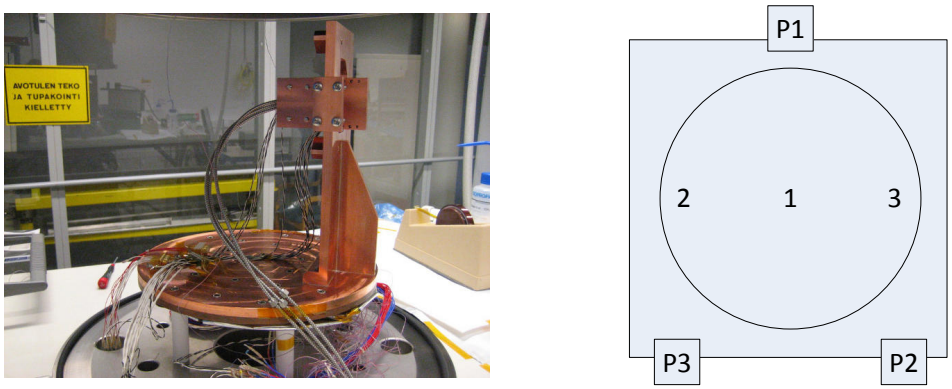

Figure 62: The thermal vacuum test jig showing the three fibre-optic feedthroughs and their positions on the FPI aperture.

The thermal vacuum test is performed with a vacuum chamber, two vacuum pumps (a mechanical pump and a cryopump) and a temperature control system. The temperature is controlled by circulating silicone fluid through the copper test jig (Figure 62), which is connected to the PFPI module. In order to speed up the process, the PFPI is wrapped to thermal blankets (Figure 63) to prevent it from radiating heat to the chamber. The temperature range of the thermal bath fluid is -60–65°C [38]. Previous experience has shown that the fluid can be heated to higher temperatures, so the manufacturer limits were exceeded at some points during the test. Vacuum is maintained in the chamber with the cryopump, which holds the pressure at 10^{-6} mbar. The temperature is recorded from thermocouples placed on the PFPI module and the mounting jig (Figure 63). The internal temperature sensor of the PFPI is also used. During the test the PFPI is illuminated with a collimated beam through a window and air gap measurements are performed constantly during the test. The measurements are performed from three locations using a 3-fibre optic vacuum feedthrough every 1–10 minutes. The feedthroughs are connected to the same multiplexer and spectrometer which were also used in earlier measurements.

The test is started with a bakeout phase, in which the temperature is kept at +65°C for 24 hours. After this the actual cycling is started. The temperature profile for the cycling is shown in Figure 64. During the test air gap values and the transmission spectrum from three points will be recorded every minute when more detailed information is required.

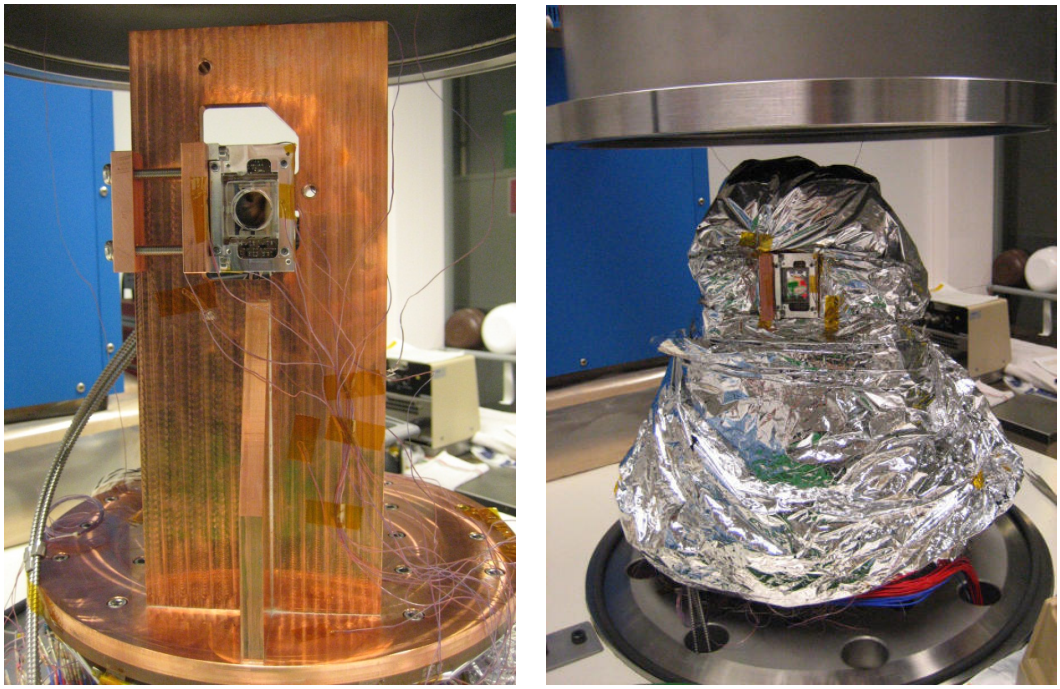

Figure 63: The placement of the thermocouples (left) and the PFPI jig wrapped in thermal blankets (right).

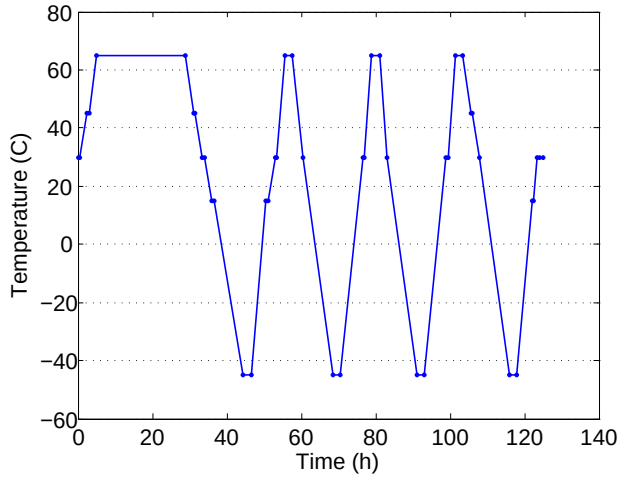

Figure 64: The temperature cycle used for thermal vacuum testing. Only three cycles out of seven are shown here after the bakeout phase, as all of them are identical.

8.2 Results

8.2.1 Thermal cycling

The thermal vacuum test was performed to show that the PFPI module can operate and survive the vacuum environment on low Earth orbit. During the test the FPI was constantly operated, and it survived the test with no detectable issues. However, a strong hysteresis effect was seen in the air gap during the measurements. The air gap drift is different depending on whether the temperature is falling or rising, but when the temperature has stabilized, the air gap difference disappears. The placement of the internal temperature sensor was identified as a probable cause for this hysteresis. The FPI mirror structure is quite well thermally isolated from the rest of the structure, the mirrors cool down or heat up much slower than the PCB. This means that the temperature shown in the Figure 65 is only the temperature of the PCB while the temperature of the mirror structure is something else. This effect could be removed by moving the temperature sensor from the PCB to the mirror structure itself.

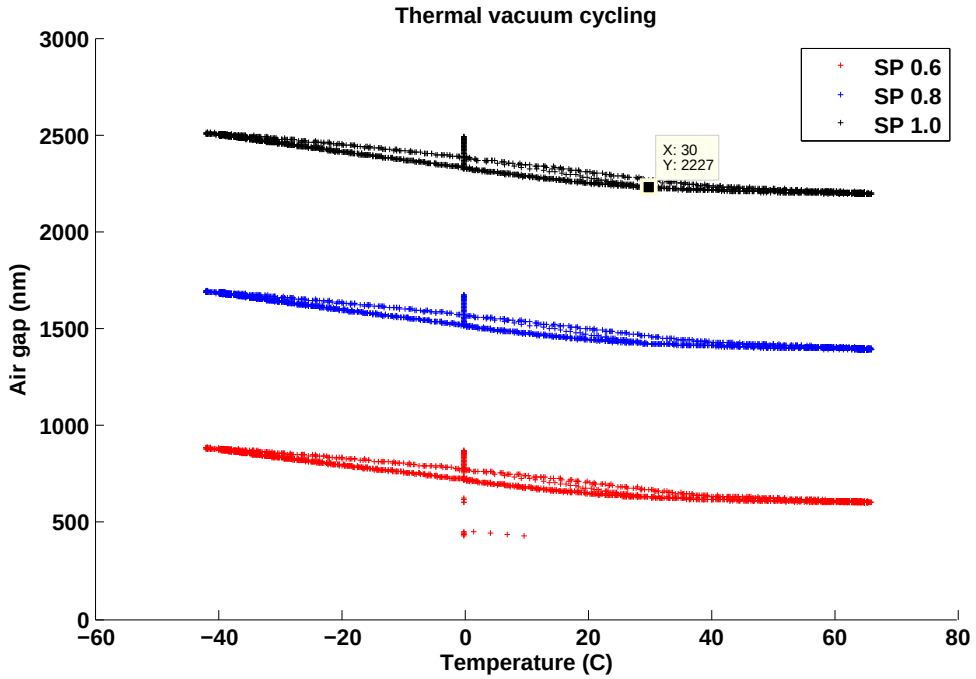

Figure 65: The air gap behaviour during the thermal vacuum testing (8 cycles). Clear hysteresis effects are visible.

The hysteresis also affects the compensation, especially when the temperature is changing rapidly. The effect can be seen in Figure 66. The difference in the curves is caused by the different cooling and heating times (Figure 67). The cool-down period is slower than the heat-up period, so the compensation can keep up better.

To test the temperature compensation, the temperature cycling was repeated, but now the temperature was let to stabilize every 5°C. Now the hysteresis effect disappeared (Figure 68), and over the temperature range (15–45°C) the largest air

gap difference is 13 nm, so the temperature drift is ca. 0.43 nm/°C, which is still outside the specifications (0.316 nm/°C). However, there is large variation in the air gap at the stabilized temperatures, e.g. at 28°C air gaps between 1424 and 1435 nm were measured. The variation at stabilized temperatures is largest close to room temperature and decreases as the temperature is increased or decreased.

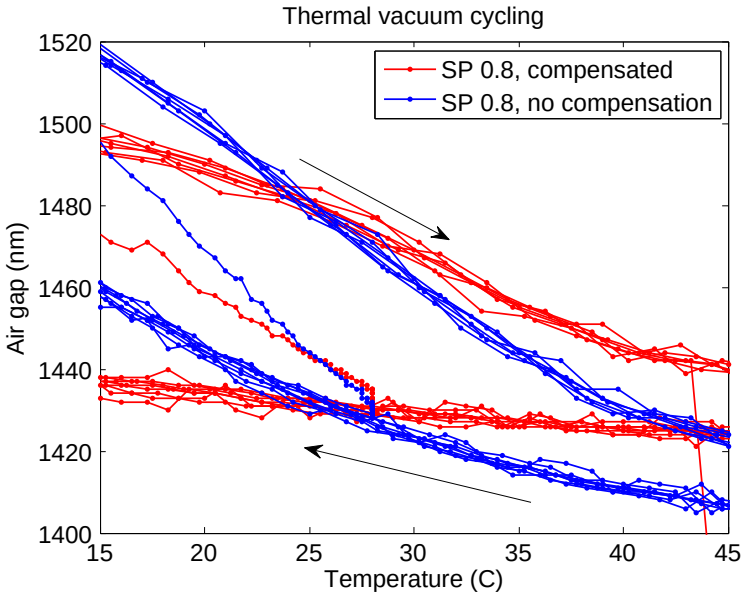

Figure 66: The effect of temperature compensation. A strong hysteresis effect can be seen in both cases.

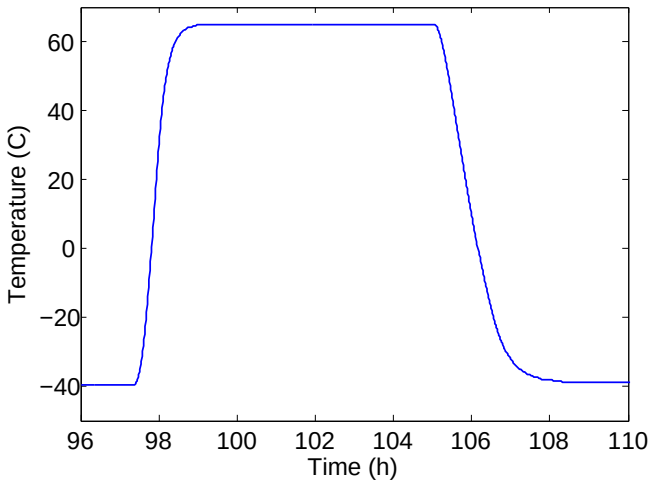

Figure 67: One temperature cycle. The heat up time is ca. two times faster than the cool down time.

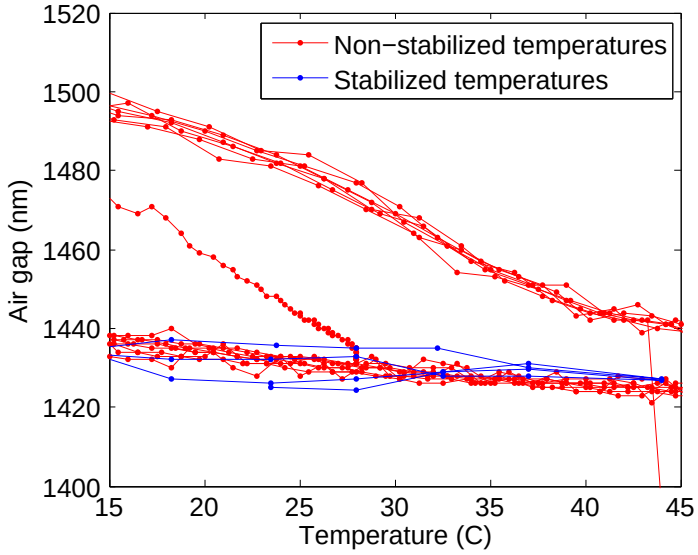

Figure 68: The effect of temperature compensation measured at stabilized temperatures during four cycles. The strong hysteresis effect has disappeared, but there is still variation in the air gap at the same temperatures, especially around room temperature.

8.2.2 Creep effect

The temperature variation seen in Figure 68 brought up concerns of long term stability of the FPI. In this test a long period measurement was peformed at three different temperatures. During the test, the temperature was first let to stabilize, and then the temperature was decreased by ca. 10°C and it was kept constant for ca. 12 hours. The air gap was constantly measured from the center of the FPI aperture. The temperature compensation was also turned off in order to see all possible underlying effects. The set point used for the test was also kept constant at 0.8 (air gap = ca. 1400 nm).

No creep effects were detected when the temperature was decreased from ca. 70 to 60°C (Figure 69). However, when the measurement was performed at room temperature (from ca. 33 to 23°C), a creep effect was detected (Figure 70). The air gap drifted back by ca. 5 nm during 12 hours. But again in the last test, where the temperature step was from ca. 2 to -6°C, no creep effects could be seen (Figure 71).

The exact cause for the creep effect remains unknown. One hypothesis is that the culprit is again the glue, which is used to fix the FPI mirrors to the piezo-actuators. As was seen earlier, the air gap shape distorts less in higher than at lower temperatures. It could be possible that the distortion of the mirrors causes a small but constant stress to the bond between the mirrors and the piezo elements, which could cause the glue to deform. This deformation is often called creep [39]. Thus the stress from the mirror structure would be relieved, causing the air gap revert slightly. The glass transition temperature of the glue given by the manu-

facturer is 70°C [40], so it could be possible that at colder temperatures the glue becomes so hard, that it prevents all kinds of creep effects. This would explain the lack of creep at colder temperatures. However, this does not explain the lack of creep at higher temperatures, so a different explanation must be found. One possibility is that at high temperatures, there are no stresses present, which could cause the glue to deform. This assumption is supported by the glue removal test performed earlier (Figure 46), which showed that at high temperature, removing the glue did not change the air gap shape as it did in lower temperatures. The reason why the creep effect is strongest at room temperature is still unknown. It may be because in room temperature both effects are present: the glue is not yet hard enough to prevent creep and the mirror is still deformed enough to cause the creep. More detailed measurements are required for further analysis.

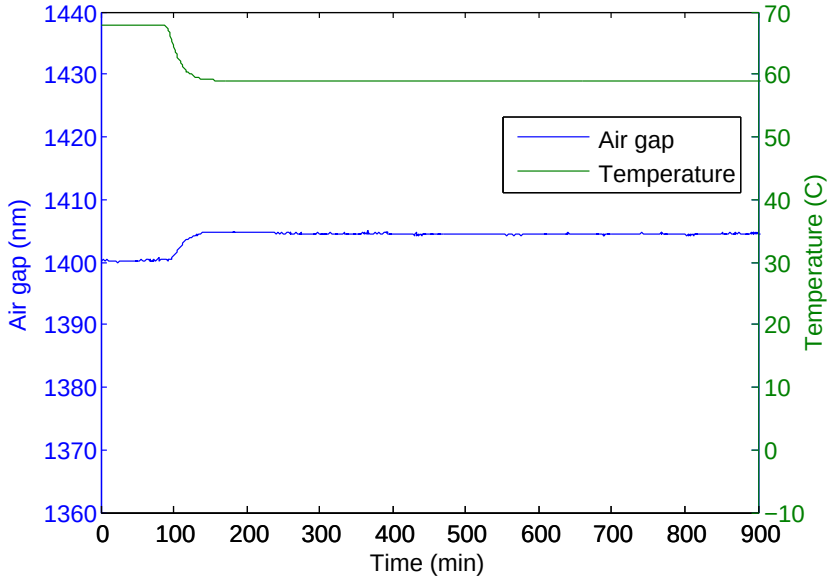

Figure 69: Long period measurement of the air gap after a temperature step. The normal temperature drift is present during the transition, but no creep effects are visible.

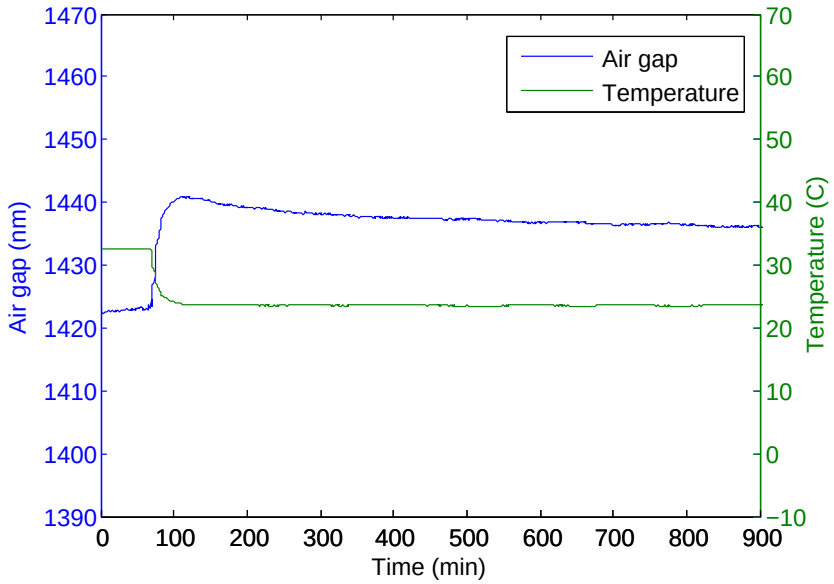

Figure 70: Long period measurement of the air gap after a temperature step. The normal temperature drift is present during the transition, and a clear creep effect to smaller air gap is visible after the temperature has stabilized.

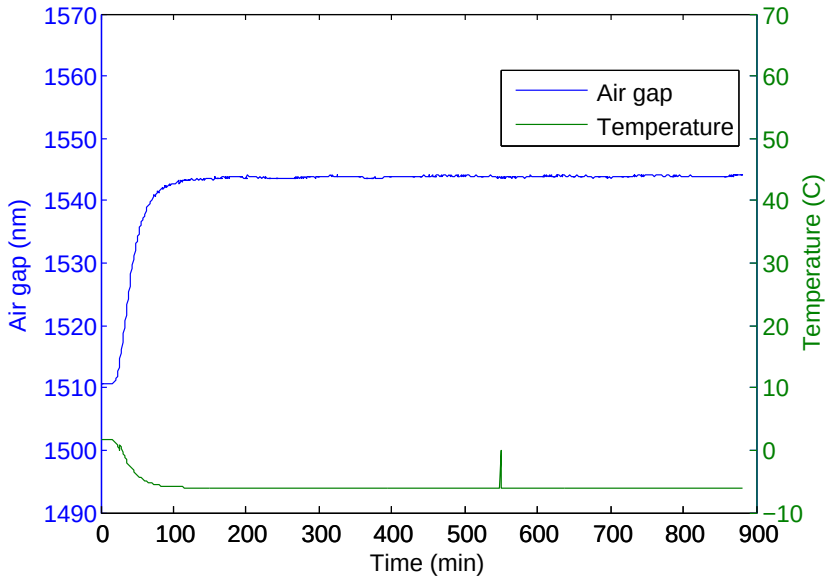

Figure 71: Long period measurement of the air gap after a temperature step. The normal temperature drift is present during the transition, but no creep effects are visible.

8.2.3 Life test

During the Aalto-1 mission, AaSI will be able to downlink one image per orbit (at most), so for a mission lasting for 1 year this means ca. 5000–6000 imaging sequences. In order to test the endurance of the PFPI module, a life test was devised. For this test, the same thermal vacuum setup was used at a constant temperature (ca. 35°C) and a typical 'imaging sequence' (11 different air gap values) is constantly repeated, with a 50 millisecond pause after each sequence. In total the sequence will take about 0.5 seconds, so during 24 hours ca. 173000 sequences will be performed. As the air gap was changed so rapidly, optical gap measurement could not be used. Instead, it was decided to only measure the piezo voltages, as a clear malfunction should be seen as a clear change in voltages. The piezo voltages were logged to a computer every 5 minutes.

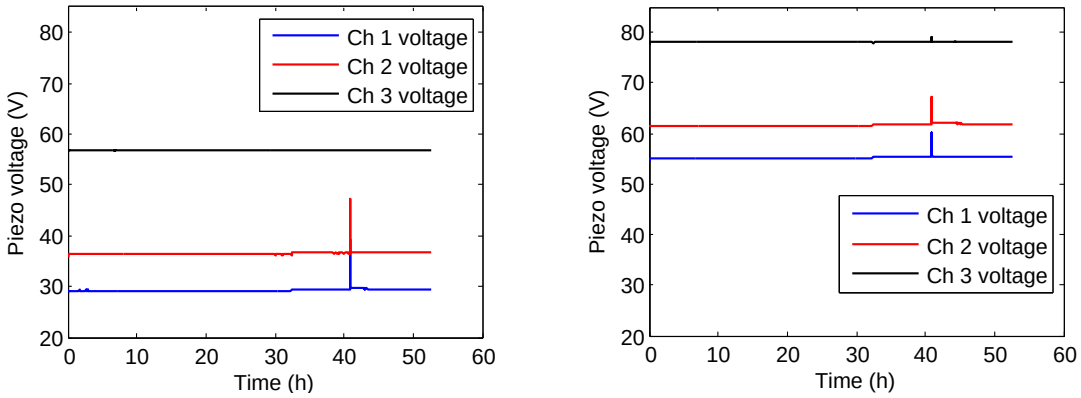

Figure 72: The piezo-voltages measured during the life test at two different set points (0.65 (left) and 0.8 (right)).

No clear changes in the behaviour of the PFPI module were seen during the test. The measurement computer froze multiple times during the test, and these errors are clearly seen in the measurement data (Figure 72). Over 200000 sequences were performed and the piezo voltages remained stable throughout the test, so it is safe to assume that the PFPI module can handle the imaging operations during the mission without any problems.

8.2.4 Transmission measurement

The transmission of the FPI was first measured before the module was installed in the thermal vacuum chamber. The measurement setup was simple: the center of the FPI was illuminated with a light source (Ocean Optics LS-1) and the transmission spectrum was measured with HR4000 spectrometer from a single point placed in the middle of the FPI (Figure 73).

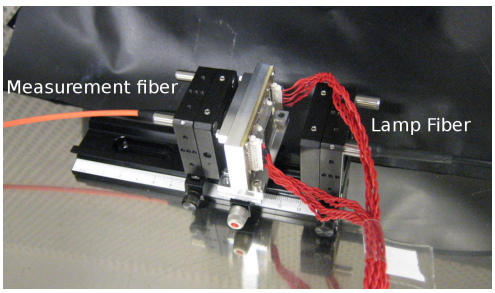

Figure 73: The setup used for measuring the FPI transmission. The center of the FPI was illuminated by the lamp and the transmission spectrum was measured with a single fiber.

The measurements show no observable difference between the two measurements taken before and after the thermal vacuum tests. At higher wavelengths there seems to be a slight drop in transmission, but at shorter wavelengths the transmission has not changed (Figure 74). Both measurements are quite well in-line with the simulated performance, only the rise in transmission near 500 nm is missing from the measured transmission values. This may be caused by manufacturing process, as the thickness of the silver layer may differ from the simulated values. There may also be errors in the simulation material parameters at shorter wavelengths, which could cause a difference.

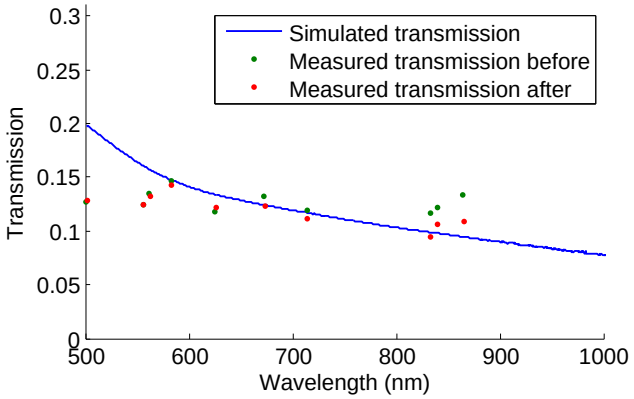

Figure 74: Transmission of the FPI before and after the thermal vacuum test. The simulated curve from Chapter 4.6 is added for comparison. No clear change in transmission can be observed. The difference below 600 nm may be caused by erroneous simulation parameters.

9 Summary and Conclusions

The goal of this work was the successful space qualification of the piezo-actuated Fabry–Perot Interferometer module for the Aalto-1 Spectral Imager. To accomplish this goal, series of tests were planned. The tests included thermal cycling in temperature chamber, vibration and shock tests, frequency and step response tests in low vacuum and finally a series of hard vacuum tests in thermal vacuum chamber. The specifications set for the PFPI module were not extremely strict, as the nature of the mission is technology demonstration, but the aim was to stay within the specifications throughout the test campaign.

For complete space qualification the PFPI module had to be tested for mechanical vibration and shocks, as the launch vehicle environment can be very harsh for delicate instruments. The vibration and shock tests were derived from the General Environment Standard, which qualifies the test subject for any launcher available on the market. The first vibration and shock tests had to be aborted, as the first PFPI module did not survive the first vibration. The thin bonding wires used by the capacitance measurement were cut, so the module design had to be revised. After a more suitable solution for the bonding wires had been applied, the PFPI module survived the vibration and shock tests without any issues, thus qualifying the PFPI for launch vehicle environment.

The thermal test campaign started with thermal characterization in a temperature chamber, and unexpected features were detected already during the first hours of the test. All PFPI modules that were tested exhibited a strong air gap temperature drift, varying from 1–2 nm/°C. The specification for the air gap drift is 0.316 nm/°C, (CWL drift of 0.2 nm for 2nd order transmission peaks). This kind of a drift effect was clearly outside the design specification, so means for temperature compensation were devised. The compensation method added a temperature dependent offset to the air gap, which reduced the air gap drift (when measured from the center of the FPI aperture) to ca. 0.1 nm/°C, which is within the design specification. However, although the center gap drift was removed, a deformation of the air gap was observed. This deformation was also identified as the main cause of the temperature drift.

In order to understand the causes of deformation, the air gap shape was measured with a narrowband light source (Helium-Neon laser) at different temperatures. The test revealed that the air gap is distorted more as the temperature is reduced. During the test excess glue was removed from the piezo-actuators, and it was noticed that removing the glue reduced the distortion significantly at lower temperatures. However, at higher temperatures (+55°C), removing the glue did not change the air gap shape. This could mean that most of the stresses causing the deformation have already disappeared at higher temperatures.

The deformation of the air gap also directly affects the spectral performance of the FPI. The spectral performance of FPI was measured at different temperatures, and the peak width was measured for different orders of interference. The peak width always remained within the specification (10–30 nm), so the spectral performance of the instrument should be adequate for the Aalto-1 mission. However, the

peak position does not remain stable with changing temperature. Over the whole operational temperature range the peak position varies less than 0.2 nm for 2nd order transmission peak, but there seems to be a hysteresis-like effect, which causes the peak position to vary even at the same temperature. This kind of instability is unpredicable, which is why it is very difficult to compensate for. To solve the issue on-board calibration methods are being developed, but alternative design approaches should also be considered.

Before the thermal vacuum testing, the proper operation in low-pressure environment had to be confirmed. It turned out that the PFPI control had a hardware bug, which prevented all operation in low-pressure environment. After the bug had been found and fixed, the FPI operated normally in vacuum environment. The stabilization time of the air gap was measured to be around 20–30 ms, which is within the design specifications.

After the vacuum operation had been confirmed, the PFPI module was placed in a thermal vacuum chamber and temperature cycling test was started. The limits used for the cycling were from -45 to +65°C and the PFPI was subjected to eight cycles. No anomalies in operation were found during the cycling, but another hysteresis effect was present. Depending whether the temperature is increasing or decreasing, the air gap will drift differently. One probable cause for this is the fact that in the PFPI modules used for qualification, the internal temperature sensor is placed on the PCB instead of the FPI mirror structure. This causes the temperature sensor to react much faster than the FPI mirrors to the changing temperature, thus causing a hysteresis-like effect.

To verify this hypothesis, another test with stabilized temperatures was performed, and the hysteresis effect disappeared. However, this test brought up another issue, which was already seen in the peak position measurements. The peak position, or the air gap, does not always return to the same value even at the same temperature. To study the problem in more detail, a long term stability measurement was perfrormed. The measurement showed that at room temperature the air gap will drift backwards by ca. 5 nm after a temperature step. The drift is very slow, as the 5 nm drift took place during a period of ca. 12 hours. Even if the effect is small, it still causes uncertainty in the air gap position when the temperature environment is changing. This behavior is still within the design specification, but there may be an offset in the measured spectrum. To remove the offset, calibration procedures using known spectral features must be used. Otherwise the PFPI module performed as expected in thermal vacuum environment, thus completing the space qualification procedures.

To conclude, the PFPI module for AaSI does meet its design specifications, and it fulfills the requirements for the Aalto-1 mission. There is still room for improvement, especially regarding the thermal stability of the FPI structure. Alternative designs are being considered, but most likely they will not be ready for the flight model of AaSI. Special attention should be given to the adhesives being used and especially to the way they are used. The current way of attaching the actuators to the FPI mirrors allows the glue joints to generate extra stresses to the mirror structure which should be avoided. The glue joints seem to be very sensitive to changing temperature

environments, which means that they are not very suitable for environments where the temperature is changing constantly, such as typical remote sensing orbits around Earth. The current adhesives also slightly exceed the general levels of outgassing allowed by ESA, so alternatives should be sought for.

After AaSI has been integrated, complete test campaign will still be required for the complete instrument, which will, in addition to the tests described here, include all the tests which were not performed to the PFPI module. These tests include electromagnetic compatibility testing and radiation testing, which were dropped from the PFPI module test campaign as the FPI module itself is not that sensitive to radiation or electromagnetic interference. It has to be kept in mind that this was the first attempt to qualify the PFPI module for space environment.

Since the results of the first test campaign were positive, the outlook on future opportunities is also rather good. After the issues with thermal stability and outgassing have been solved, the PFPI technology developed at VTT will be very suitable for harsh environment applications, which require moderate to good spectral resolution. This applies also for the complete AaSI-instrument. As the design is already compatible with the CubeSat standard, the instrument can be easily included in any space mission requiring small instruments capable of spectral imaging at moderate resolution.

References

[1] J. Nieke, H. Schwarzer, A. Neumann, and G. Zimmermann, Imaging Spaceborne and Airborne Sensor Systems in the Beginning of the Next Century, *Sensors, Systems, and Next-Generation Satellites, Proceedings of SPIE*, vol. 3221, pp. 581-592, 1997.

[2] P, Fortescue, J. Stark, and G. Swinerd, *Spacecraft Systems Engineering,* 3rd edition, Wiley, 2003.

[3] J. Bouwmeester and J. Guo, Survey of Worldwide Pico- and Nanosatellite Missions, Distributions and Subsystem Technology, *Acta Astronautica*, vol. 67, pp. 854-862, 2010.

[4] R. J. Twiggs, Space System Developments at Stanford University – From Launch Experience of Microsatellites to the Proposed Future Use of Picosatellites, *Small Payloads in Space 79, Proceedings of SPIE*, vol. 4136, pp.79-86, 2000.

[5] H. Heidt, J. Puig-Suari, A. S. Moore, S. Nakasuka & R. J. Twiggs, CubeSat: A New Generation of Picosatellite for Education and Industry Low-Cost Space Experimentation, *Proceedings of the 14th Annual/USU Conference on Small Satellites*, 2000.

[6] CubeSat Design Specification, Rev. 12, Cal Poly, August, 2009.

[7] A. Näsilä et al., Aalto-1 - A Hyperspectral Earth Observing Nanosatellite, *Sensors, Systems and Next-Generation Satellites XV, Proceedings of SPIE*, vol. 8176, 2011.

[8] G.E. Brueckner et al., The Large Angle Spectroscopic Coronagraph (LASCO) - Visible Light Coronal Imaging and Spectroscopy, *Solar Physics*, vol. 162, issue 1-2, pp. 357-402, 1995.

[9] V. J. Abreu, W. R. Skinner, P. B. Hays, and J.-H. Yee, Optical Effects of Spacecraft-Environment Interaction Spectrometric Observations of the DE-2 Satellite, *Journal of Spacecraft and Rockets*, vol. 22, issue 2, pp. 177-180, 1985.

[10] H. Saari, V. Aallos, A. Akujärvi, T. Antila, C. Holmlund, U. Kantojärvi, J. Mäkynen, &J. Ollila, Novel Miniaturized Hyperspectral Sensor for UAV and Space Applications, *Sensors, Systems and Next-Generation Satellites XIII, Proceedings of SPIE*, vol. 7474, 2009.

[11] C. Fabry and A. Perot, Sur les Franges des Lames Minces Argentées et Leur Application à la Mesure de Petites Épaisseurs d'Air, *Annales De Chimie et de Physique*, vol. 12, pp. 459-501, 1897.

[12] J. Antila, A. Miranto, J. Mäkynen, M. Laamanen, A. Rissanen, M. Blomberg, H. Saari &J. Malinen, MEMS and Piezo Actuator Based Fabry–Perot Interferometer Technologies and Applications at VTT, *Next-Generation Spectroscopic Technologies III, Proceedings of SPIE*, vol. 7680, 2010.

[13] Max Born and Emil Wolf, *Principles of Optics*, 6th edition, Pergamon Press, 1980.

[14] E. Hecht and A. Zajac, *Optics*, 1st edition, Addison-Wesley, 1974.

[15] E. Ikonen, *Optiikan perusteet*, MIKES TKK Mittaustekniikka, 2006.

[16] A. Martel, An Introduction to the TFI Etalon, Technical report, Doc No.: JWST-STScI-002059, SM-12, July 15, Space Telescope Science Institute, 2010.

[17] P. F. Atherton, N. K. Reay and J. Ring, Tunable Fabry–Perot Filters, *Optical Engineering*, vol. 20, issue 6, pp. 806-814, 1981.

[18] Etalon Thickness Report, LightMachinery Inc, 19.11.2012.

[19] P. Jacquinot, The Luminosity of Spectrometers with Prisms, Gratings of Fabry–Perot Etalons, *Journal of the Optical Society of America*, vol. 44, issue 10, pp. 761-765, 1954.

[20] C. Haley, N. Roy, Z. Osman, N. Rowlands & A. Scott, Space Environment Challenges With the Tunable Fabry-Pérot Etalon for the JWST Fine Guidance Sensor, *Space Telescopes and Instrumentation 2012, Proceedings of SPIE*, vol. 8442, 2012.

[21] J. Mäkynen, A Lightweight Hyperspectral Imager, Master's thesis, 2009.

[22] A. Spisser et al., Highly Selective and Widely Tunable 1.55 μm InP/Air-Gap Micromachined Fabry–Perot Filter for Optical Communications, *IEEE Photonics Technology Letters*, vol. 10, issue 9, pp. 1259-1261, 1998.

[23] C. H. Henry, Theory of Spontaneus Emission Noise in Open Resonators and its Application to Lasers and Optical. Amplifiers, *Journal of Lightwave Technology*, vol. LT-4, issue 3, pp. 288-297, 1986.

[24] Ariane 4 User's Manual, issue 2, February 1999.

[25] M. E. Bumbaugh and D. S. Rosario, Ionizing Radiation Effects on Commercial 256K EEPROM's, *1992 IEEE Radiation Effects Data Workshop Record*, No. 92TH0507-4, pp. 42-47, 1992.

[26] ECSS Standard Space Product Assurance - Materials, Mechanical Parts and Processes, ECSS-Q-ST-70C, 2009.

[27] K. Viherkanto et al., TN3 Spectral Imager DM Detailed Design Report, Technical note, Doc No.: A1-AaSI-DD-TN3, February 15, VTT, 2013.

[28] A. Kestilä, Aalto-1 Preliminary Mission & System Requirements, Requirement specification, Doc No.: A1-SYS-RS-01-v2, October 4, Aalto University, 2011.

[29] H. Saari, C. Holmlund, J. Mäkynen, J. Antila, U. Kantojärvi and R. Mannila, A Method for Determining Calibration Parameters for a Spectrometer, Finnish patent application FI20126066, 2012.

[30] K. Viherkanto and A. Näsilä, TN1 PFPI Space Environment Compatibility Validation Test Report, Technical note, Doc No.: A1-SPE-DD-TN1, February 15, VTT, 2013.

[31] T. R. Hicks, N. K. Reay, P. D. Atherton, The Application of Capacitance Micrometry to the Control of Fabry–Perot Etalons, *Journal of Physics E: Scientific Instruments*, vol. 17, issue 1, pp. 49-55, 1984.

[32] J. M. Vaughan, *The Fabry–Perot Interferometer: History, Theory, Practice and Applications*, 1st edition, Taylor & Francis Group, 1989.

[33] General Environmental Verification Standard (GEVS) for GSFC Flight Programs and Projects, GSFC-STD-7000, 2005.

[34] David R. Lide (Editor), *Handbook of Chemistry and Physics,* 72nd edition, CRC Press, 1991.

[35] T. L. Killeen, P.B. Hays and J. DeVos, Parallelism Maps for Optically Contacted Etalons, *Applied Optics*, vol. 20, issue 15, pp. 2616-2619, 1981.

[36] K. P. Reardon and F. Cavallini, Characterization of Fabry–Perot Interferometers and Multi-Etalon Transmission Profiles, *Astronomy & Astrophysics*, vol. 481, pp. 897-912, 2008.

[37] T. D. Rossing, F. R. Moore & P. A. Wheeler, *The Science of Sound,* 3rd edition, Addison-Wesley, 2001.

[38] Bath Fluid Thermal HY, Product Data sheet, Julabo GmbH.

[39] D. V. Rosato et al., *Plastics Design Handbook,* 1st edition, Kluwer Academic Publishers, 2001.

[40] OP-61 Optical Adhesive, Product data sheet, Dymax Corporation, 2000.

Appendix A: Vibration and Shock Test Procedures

The exact procedure used for vibration testing is described below:

1. Performance checkout of the PFPI module in the laboratory
2. Install the PFPI on the shaker for X-direction
3. X-axis 25% random vibration test. Measure unbiased and biased piezo voltage frequency response and assess the difference between these cases.
4. Functional test
5. X-axis 50% random vibration test and unbiased voltage measurement
6. Functional test
7. X-axis 100% random vibration test and unbiased voltage measurement
8. Functional test
9. Install the PFPI on the shaker for Y-direction
10. Y-axis 25% random vibration test. Measure unbiased and biased piezo voltage frequency response and assess the difference between these cases.
11. Functional test
12. Y-axis 50% random vibration test and unbiased voltage measurement
13. Functional test
14. Y-axis 100% random vibration test and unbiased voltage measurement
15. Functional test
16. Install the PFPI on the shaker for Z-direction
17. Z-axis 25% random vibration test. Measure unbiased and biased piezo voltage frequency response and assess the difference between these cases.
18. Functional test
19. Z-axis 50% random vibration test and unbiased voltage measurement
20. Functional test
21. Z-axis 100% random vibration test and unbiased voltage measurement
22. Functional test
23. Performance checkout of the PFPI module in the laboratory

The exact procedure used for shock testing is described below:

1. Install the PFPI adapter for the shock table Z-axis configuration. Make necessary tuning without the PFPI module.
2. Install the PFPI module
3. Six shocks are imposed in one direction. (It is not possible to install the module upside-down).
4. Functional test
5. Install the PFPI adapter for the shock table X-axis configuration. Make necessary tuning without the PFPI module.
6. Install the PFPI module
7. Three shocks are imposed in one direction (+X), then switch direction. Three shocks in the other direction (-X).
8. Functional test
9. Install the PFPI adapter for the shock table Y-axis configuration. Make necessary tuning without the PFPI module.
10. Install the PFPI module
11. Three shocks are imposed in one direction (-Y), then switch direction. Three shocks in the other direction (-Y).
12. Functional test
13. Performance checkout of the PFPI module in the laboratory

Appendix B: Outgassing Measurements

Outgassing definitions

- TML = The difference of mass directly before and after vacuum test as a percentage of initial mass.
- RML = The difference between initial mass and mass after re-conditioning, showing the amount of non-water products.
- CVCM = The amount of material collected by the collectors during vacuum test divided by the initial mass of the material.

MINISTERIO
DE DEFENSA

SECRETARIA DE ESTADO DE DEFENSA
INSTITUTO NACIONAL DE
TECNICA AEROESPACIAL

ÁREA DE MATERIALES METÁLICOS
(4310)

L E T T E R

S/REF:
N/REF: AMM/AHH/ 040
FECHA: 11/02/2013
ASUNTO: OUTGASSING TEST REPORT

Kai Viherkanto

VTT (Technical Research Centre of Finland)
Tietotie 3, Espoo
FI-02044 VTT
Finland

Dear Sir,

Please, find enclosed to this letter, the outgassing test report ***ESE-RPT-4316-095-INTA-12***, as well as the IR Spectrums obtained.

Yours faithfully,

Fdo.: Federico Longo Gregorio
Head of the Metallic Materials Area

06Y0570F. Área de Materiales Metálicos

CORREO ELECTRÓNICO:
longogf@inta.es

CARRETERA DE AJALVIR, KM. 4
28850 TORREJÓN DE ARDOZ
TEL: +34 91 520 13 70
FAX: +34 91 520 1381/1592

Ctra. Ajalvir, km.4. 28850 Torrejón de Ardoz (Madrid). C.I.F. nº Q 2822003F

MINISTERIO DE DEFENSA / SECRETARÍA DE ESTADO DE DEFENSA / INSTITUTO NACIONAL DE TÉCNICA AEROESPACIAL	Doc. N°:	ESE-RPT-4316-095-INTA-12 TEST DMAV-1229
	Página: i de ii	Edición: 01

DOC. N°.: **ESE-RPT-4316-095-INTA-12**

TITULO: / *TITLE:* **ENSAYO DE DESGASIFICACIÓN/** *OUTGASSING TEST:* DMAV-1229

PETICIONARIO: / *REQUIRED BY:* VTT (Technical Research Centre of Finland). *Photonic Devices and Measurement Solutions. Tietotie 3, Espoo. FI-02044 VTT. Finland.*

	NOMBRE *NAME*	FIRMA *SIGNATURE*	FECHA *DATE*
PREPARADO POR: *WRITTEN BY:*	Alejandro **HERRERA HERNÁNDEZ** Titulado del Laboratorio de Desgasificación		11/02/2013
REVISADO Y ACEPTADO POR: *VERIFIED AND APPROVED BY:*	Federico **LONGO GREGORIO** Jefe del Área de Materiales Metálicos		11/02/2013

INSTITUTO NACIONAL DE TÉCNICA AEROESPACIAL – LABORATORIO DE MATERIALES Y PROCESOS – ÁREA DE MATERIALES METÁLICOS – MINISTERIO DE DEFENSA

HISTORIA DEL DOCUMENTO (*DOCUMENT'S HISTORY*)		
EDICIÓN *EDITION*	FECHA *DATE*	INFORMACIÓN *INFORMATION*
01	2013, feb - 11	Edición inicial de este documento (*Initial edition of this document*)

REGISTRO DE EDICIÓN DE PÁGINAS
LIST OF EFFECTIVE PAGES

La edición de este documento comprende las siguientes páginas en las ediciones expuestas:
This document comprises the following pages in the issues showed below:

Página *Page*	Edición *Issue*	Página	Edición *Issue*	Página *Page*	Edición *Issue*
Portada (*First Page*): i	01				
ii	01				
1 - 4	01				

ENSAYO DE DESGASIFICACIÓN/*OUTGASSING TEST*

INDICE
INDEX

I – ANTECEDENTS

In our Laboratory of Materials Outgassing 2 samples have been received coming from VTT (Technical Research Centre of Finland) for the outgassing test realization according to *ECSS-Q-ST-70-02C*, ed. 15 Nov, 2008.

II- TEST SAMPLES

Nº SAMPLE NAME	PETITIONER OF THE TEST MATERIAL DESCRIPTION
12147 *DYMAX OP-61-LS*	*VTT (Technical Research Centre of Finland).* Manufacturer: Dymax Corporation. Optical adhesive. Urethane (Meth) Acrylate.Sample was UV cured ca 10s.Batch nº: 94729-IX221
12148 *DYMAX OP-29 GEL*	*VTT (Technical Research Centre of Finland).* Manufacturer: Dymax Corporation. Optical adhesive. Acrylated Urethane. Sample was UV cured ca 10s.Batch Nº: TI793-HN559

III – TEST CONDITIONS

The samples have been tested according to the specification mentioned previously and whose test conditions are the following:

* Conditioning of the sample during 24 hours to (22 ±3)ºC and (55 ±10)% RH.
* Realization of the test, during 24 hours, under the following conditions:
  * Sample temperature: 125ºC
  * Cold plate temperature: 25ºC
  * Test vacuum pressure: range 10^{-6} - 10^{-7} Torr
* Post - conditioning of the sample during 24 hours to (22 ±3)ºC and (55 ±10)% RH.

IV - TEST RESULTS

The results of this test are exposed in the next page, and they are refered only to the samples included in this report.

MINISTERIO DE DEFENSA — SECRETARÍA DE ESTADO DE DEFENSA — INSTITUTO NACIONAL DE TÉCNICA AEROESPACIAL

ESE-RPT-4316-095-INTA-12
TEST DMAV-1229
Página: 4 de 4 | Edición: 01

ÁREA DE MATERIALES METÁLICOS. LABORATORIO DE DESGASIFICACIÓN/*OUTGASSING TEST LAB*
ENSAYO DE DESGASIFICACIÓN/*OUTGASSING SCREENING TEST*. ECSS-Q-ST-70-02C STANDARD

ENSAYO/ *TEST Nº:* DMAV-1229 — **FECHA /*DATE:*** 2012, dic - 20

MUESTRA/*SAMPLE* ID. Nº	DENOMINACIÓN/*DESIGNATION*	C	TML%	RML%	CVCM%	IR ANALYSIS wave number $\bar{\nu}$ [cm^{-1}]
12147	Name: *DYMAX OP-61-LS* Receipt date: 2012, dic - 10 Code: Sample size in capsule: 1 2 3 4	1	2,450	2,115	0,164	d:
		2	2,296	1,980	0,134	IR: 712,56 751,13 771,38 834,02 960,37 987,38 1053,91 1170,58 1264,11 1313,29 1363,43 1405,85 1457,92 1570,74 1601,59 1672,95 2865,70 2931,27 2965,02 3450,03
		3	2,548	2,214	IR plate	
		$\bar{A}$	**2,432**	**2,103**	**0,149**	Undeterminate. **Note:** IR peaks do not represent chemical nature indicated in the Material Identification Card.
12148	Name: *DYMAX OP-29 GEL* Receipt date: 2012, dic - 10 Code: Sample size in capsule: 1 2 3 4	1	3,810	2,991	0,017	d:
		2	3,844	3,075	0,033	IR:
		3	3,835	3,022	IR plate	
		$\bar{A}$	**3,830**	**3,029**	**0,025**	None. (Signal response very low)
	Name: Receipt date: 2012, dic - 10 Code: Sample size in capsule: 1 2 3 4	1				d:
		2				IR:
		3			IR plate	
		$\bar{A}$				
	Name: Receipt date: 2012, dic - 10 Code: Sample size in capsule: 1 2 3 4	1				d:
		2				IR:
		3			IR plate	
		$\bar{A}$				
	Name: Receipt date: 2012, dic - 10 Code: Sample size in capsule: 1 2 3 4	1				d:
		2				IR:
		3			IR plate	
		$\bar{A}$				

OBSERVACIONES/*GENERAL REMARKS:*

TITULADO LABORATORIO DE DESGASIFICACIÓN: A. Herrera Hernández

JEFE DEL ÁREA DE MATERIALES METÁLICOS: F. Longo Gregorio

INSTITUTO NACIONAL DE TÉCNICA AEROESPACIAL · ÁREA DE MATERIALES ESTRUCTURALES · ÁREA DE MATERIALES METÁLICOS · MINISTERIO DE DEFENSA

FORMATO 04045/96F. ÁREA DE MATERIALES METÁLICOS

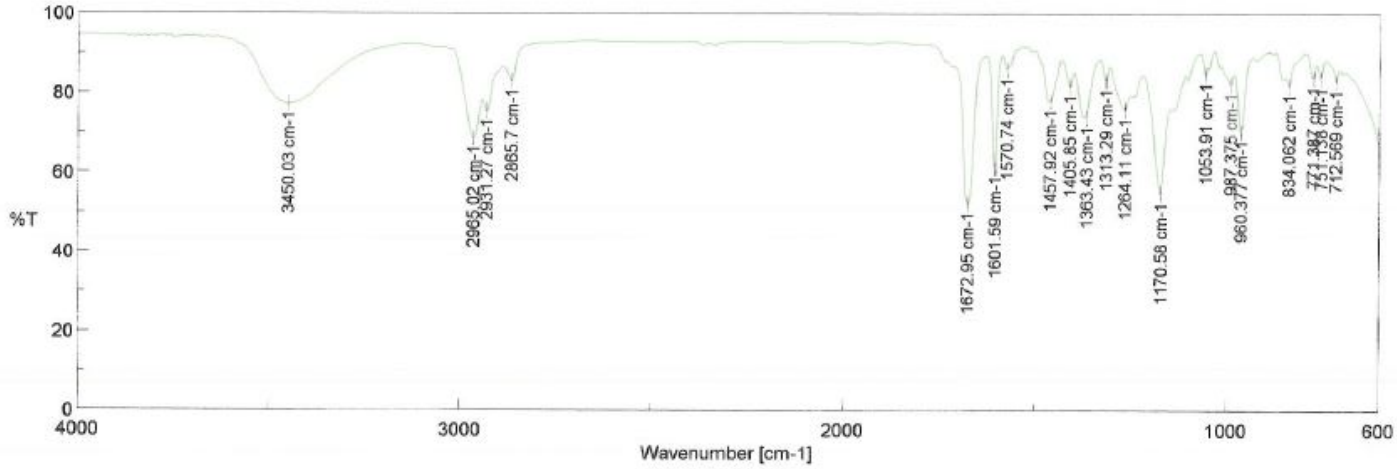

2013_01_17-7.jws

[Comments]

Sample name	OP-61-LS - 12147
Comment	Desgasificacion
User	
Division	Inta
Company	INTA

[Detailed Information]

Creation date	17/01/2013 10:29
Data array type	Linear data array
Horizontal axis	Wavenumber [cm-1]
Vertical axis	%T
Start	599.753 cm-1
End	4000.6 cm-1
Data interval	0.964233 cm-1
Data points	3528

[Measurement Information]

Model Name	FT/IR-4200typeA
Serial Number	C089761018
Measurement Date	17/01/2013 10:29
Light Source	Standard
Detector	TGS
Accumulation	50
Resolution	4 cm-1
Zero Filling	On
Apodization	Cosine
Gain	Auto (1)
Aperture	Auto (7.1 mm)
Scanning Speed	Auto (2 mm/sec)
Filter	Auto (30000 Hz)

Appendix C: Temperature Drift of the FPI Electronics

The temperature drift of the FPI pre-amplifier and the reference capacitors were measured to eliminate possible sources of temperature drift. The temperature drift was measured as a relative deviation from the starting point (25°C), denoted in parts-per-million (ppm). The preamplifier drift is ca. 55.6 ppm/°C (Figure A1), which is about 50 times less than the measured FPI temperature drift (ca. 1.5 nm/°C). The capacitor temperature drift measured was ca. 5 ppm above room temperature (Figure A2), which is much less than the measured temperature drift of the FPI.

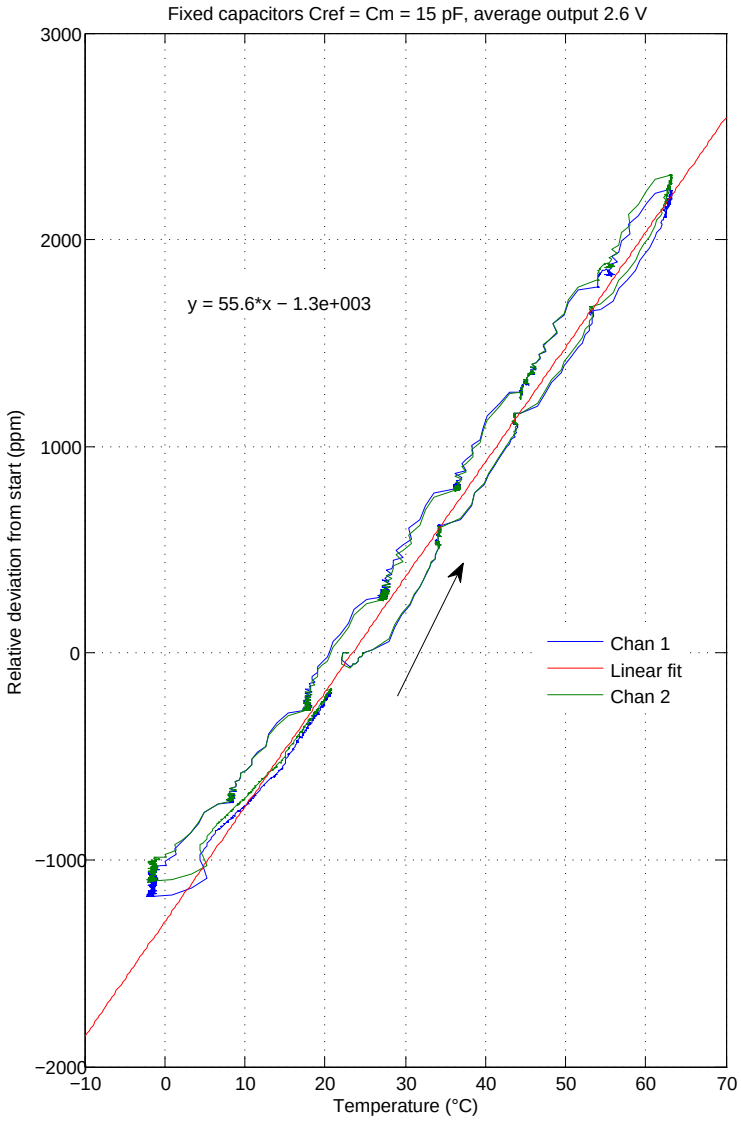

Figure A1: Relative temperature drift of the FPI pre-amplifier. Measured by Christer Holmlund at VTT.

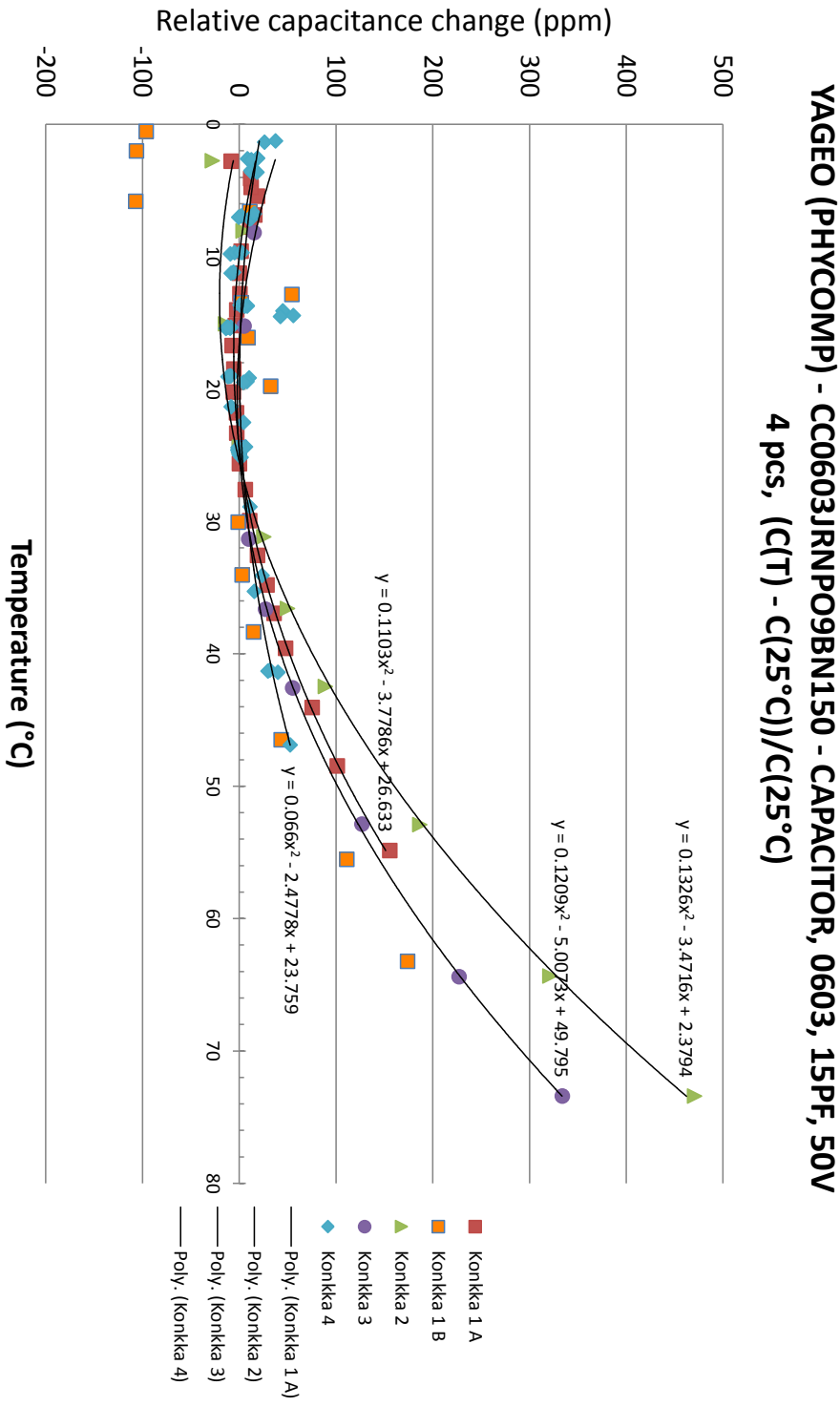

Figure A2: Relative temperature drift of the reference capacitors. Measured by Chirster Holmlund and Osmo Viljamaa at VTT.